

**THE EFFECT OF GRAIN SIZE AND PHASE CONSTITUTION
ON THE MAGNETIC PROPERTIES OF HIGHER CONTENT Cr
SUBSTITUTED $\text{Fe}_{73.5-x}\text{Cr}_x\text{Nb}_3\text{Cu}_1\text{Si}_{13.5}\text{B}_9$ NANOCRYSTALLINE
ALLOYS**

M. Phil. Thesis

BY

MOHAMMAD ZASHED IQBAL



**DEPARTMENT OF PHYSICS
KHULNA UNIVERSITY OF ENGINEERING & TECHNOLOGY
KHULNA - 9203, BANGLADESH
JULY - 2015**

**THE EFFECT OF GRAIN SIZE AND PHASE CONSTITUTION
ON THE MAGNETIC PROPERTIES OF HIGHER CONTENT Cr
SUBSTITUTED $Fe_{73.5-x}Cr_xNb_3Cu_1Si_{13.5}B_9$ NANOCRYSTALLINE
ALLOYS**

BY

MOHAMMAD ZASHED IQBAL

ROLL NO: 1055502

SESSION: JANUARY - 2010

A THESIS SUBMITTED TO THE DEPARTMENT OF PHYSICS,
KHULNA UNIVERSITY OF ENGINEERING & TECHNOLOGY,
KHULNA - 9203 IN PARTIAL FULFILMENT OF THE
REQUIRMENT FOR THE DEGREE OF MASTER OF PHILOSOPHY



DEPARTMENT OF PHYSICS
KHULNA UNIVERSITY OF ENGINEERING & TECHNOLOGY
KHULNA - 9203, BANGLADESH
JULY - 2015

**KHULNA UNIVERSITY OF ENGINEERING & TECHNOLOGY
DEPARTMENT OF PHYSICS**

Approval

This is to certify that the thesis work submitted by *Mohammad Zashed Iqbal* entitled “ *The Effect of Grain size and Phase constitution on the Magnetic Properties of higher content Cr substituted $Fe_{73.5-x}Cr_xNb_3Cu_1Si_{13.5}B_9$ Nanocrystalline Alloys*” has been accepted by the board of examiners for the partial fulfillment of the requirements for the degree of *Master of Philosophy* in the Department of *Physics*, Khulna University of Engineering & Technology, Khulna, Bangladesh in 30 July 2015.

Board of Examiners

Sl. No. Name, Designation & Address


1. Prof. Dr. Shibendra Shekher Sikder
Department of Physics
Khulna University of Engineering & Technology
Khulna-9203, Bangladesh


.....
Chairman & Supervisor

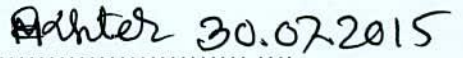
2. Head
Department of Physics
Khulna University of Engineering & Technology
Khulna-9203, Bangladesh


.....
Member

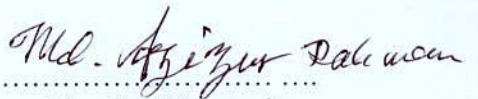
3. Dr. Abdul Gafur
Senior Engineer, PD, DMTBI, PP& PDC BCSIR
Dhanmondi, Dhaka


.....
Co- Supervisor

4. Prof. Dr. Md. Abdullah Elias Akhter
Department of Physics
Khulna University of Engineering & Technology
Khulna-9203, Bangladesh


.....
Member

5. Prof. Dr. Md. Azizur Rahman
Department of Physics
University of Dhaka, Bangladesh


.....
Member (External)

30.7.2015

DECLARATION

This is to certify that the thesis work entitled as “**The Effect of Grain size and Phase constitution on the Magnetic Properties of higher content Cr substituted $Fe_{73.5-x}Cr_xNb_3Cu_1Si_{13.5}B_9$ Nanocrystalline Alloys**” has been carried out in partial fulfillment of the requirement for M. Phil degree in the department of Physics, Khulna University of Engineering & Technology, Khulna - 9203, Bangladesh. The above research work or any part of this work has not been submitted anywhere for the award of any degree or diploma. No other person’s work has been used without due acknowledgement.

1. Supervisor



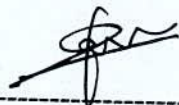
(Prof. Dr. S. S. Sikder)

Candidate



(Mohammad Zashed Iqbal)

2. Co-Supervisor



(Dr. M. A. Gafur)

TO
MY PARENTS

Acknowledgements

I express, with due respect my deepest sense of sincere gratitude indebtedness to my supervisor Prof. Dr. Shibendra Shekher Sikder, Department of Physics, Khulna University of Engineering & Technology (KUET), Khulna for his indispensable guidance, erudite discussion, constructive suggestions, fruitful discussion and constant inspiration of this research work. He is always ready to provide a lucid explanation of the different concepts involved and critical reading of the script and subsequent corrections are much appreciated. Any mistakes that remain are of course mine.

I am very much indebted to my Co-Supervisor Dr. Abdul Gafur, Senior Engineer, PP & PDC, Bangladesh Council of Scientific and Industrial Research (BCSIR), Dhanmondi, Dhaka-1205, Bangladesh for introducing the present research topic and inspiring guidance and valuable suggestion of this research work, who has consistent support and necessary motivation to progress my experimental works.

I am indebted to Professor Dr. Jolly Sultana, Head, Department of Physics, Khulna University of Engineering & technology (KUET), Khulna for her valuable direction and instructions.

I am grateful to Mrs. Shireen Akhter, Head & Chief Scientific Officer (CSO), Materials Science Division (MSD), Atomic Energy Centre, Dhaka (AECD) for providing kind opportunity to use the laboratory for experimental work. My thanks are also for Dr. Dilip Kumar Saha, Chief Scientific Officer, Mr. H. N. Das and Mr. M. A. Mamun, Scientific Officer, Materials Science Division, Atomic Energy Center, Dhaka for providing me with technical assistance form time during my research work and providing kind opportunity to work in their laboratory for experimental purpose regarding my thesis.

It is a matter of great pleasure for me to record the deepest sense of gratitude to Prof. Dr. Md. Mahbub Alam, Prof. Dr. Abdullah Elias Akther, Department of Physics, KUET, has been given me a strong support in various ways during the entire period of my study in the department of Physics, KUET. My thanks are also for Mr. Md. Kamrul Hasan reza, Mr. Md. Asaduzzaman, Mr. Sujit Kumer Shil, Assistant professor, Department of Physics, KUET for tired less co-operation in my thesis work.

I am deeply grateful to Mr. Rakibul Quadeer, Engineer, DMTBI, PP & PDC, Bangladesh Council of Scientific and Industrial Research (BCSIR), Dhanmondi, Dhaka-1205, Bangladesh, who helped me to understand annealing, XRD measurements and technical assistance in the laboratory. My thanks are also for all the staff of PP & PDC, BCSIR whose were very much co-operative with me.

I am mostly indebted forever to Mr. Enamul Hoque Bhuiyan, Ex. Assistant Professor, Department of Physics, KUET, Khulna. I become able to feel and realize it was not possible to complete my M. Phil. except his cordial help with generous thinking and skillful suggestions. I must express my gratitude and very special thanks to Mr. Md. Alamgir Hossain and Mr. Suman Kumar Halder, Lecturer, Department of Physics, KUET, Mr. Ratan Kriskna Howlader, Mr. Nitish Chandro Mollik, Mr. Md. Humayan Ahmed, Mr. Zakir Hossain and other postgraduate students of our group and friends who have given me a lot of encouragement to accomplish this noble work.

I am very much grateful to Prof. Md. Mahbubur Rahman, Principle, Prof. Tarik Hasan Khan, Vice-Principle, and Head, Dept. of Physics, Govt. Rajendra College, Faridpur as well as my colleagues who are more or less support me to make my duties easier and with necessary help.

I want to acknowledge the memorable well-wisher Mr. Masudul Hassan, Associate Professor (Geography), who provide me a lot of encouragement to go for M. Phil. Mostly indebted for ever to Dr. Harun-Ar-Rashid, Monitoring Officer, DSHE, Dhaka, who helped me to get necessary permission from the higher authority. I wish to express thanks to my college-life friend Mr. Shohan Paul and his wife for arranging accommodation during my study in Khulna. I am mostly indebted to one of my best friend Mr. Anwar Sadat (Rumi) and his wife forever for arranges accommodation during my Lab study in Dhaka. My thanks are forever to my best friend Mr. Shyam who helpe me to make decision about every sphere of life.

The deepest sense of gratitude to Mr. Mohammad Shamsur Rahman (Salim), Lecturer, Accounting, Govt. Rajendra college, Faridpur is a think tank and my idol. Also express thanks to my best well-wishers Mr. Murad, Mr. Noor A Salim, Mr. Abdullah Al Masud, Mr. A. Samad, Mr. Hedayet and all the memorable friends and colleagues. It would have not been possible for me to bring out this thesis without their help and constant encouragement.

Many thanks are due to the Director, Atomic Energy Center, Dhaka for his kind permission to use the laboratory of Material Science Division, AEC, Dhaka.

I am thankful to Ms. Alhamra Parveen, Ms. Anjuman Ara Begum, Ms. Nazmunnahar Begum and Mr. Anawar Hossain of Material Science Division, AECD, for their co-operation during the experiments of my research work at the laboratory of AECD.

I wish to express thanks to my life-partner Mrs. Asma-UI-Husna Asha for keeping me free from family-affairs during my work and also for her sustained inspiration, encouragement and continuous co-operation. Finally my thanks are due to only loving daughter Azmina Iqbal (Aava).

My gratitude and thanks are also to my father, mother and father- in- law, mother- in- law, brothers, sisters, brother- in- law, sister- in- law, nephew, niece and all of my family members whose are very much co-operative with my higher studies.

My special thanks to Mrs. Nandita Saha, wife of Prof. Dr. S. S. Sikder for her heartfelt encouragement, cares and helps for the entire period of my M. Phil study.

I also wish to thank the authority of Khulna University of Engineering & Technology (KUET), Khulna for providing me with the necessary permission and financial assistance for conducting this thesis work.

Mohammad Zashed Iqbal

ABSTRACT

This thesis is based on the experimental investigation of the effect of grain size and phase constitution on the magnetic behavior of $\text{Fe}_{73.5-x}\text{Cr}_x\text{Nb}_3\text{Cu}_1\text{Si}_{13.5}\text{B}_9$ [$x = 7, 9, 10$ & 12.5] alloys in the amorphous and annealed states. The samples are initially prepared in the amorphous state in the form of thin ribbons by rapid quenching technique at wheel speed of 25m/s in an Ar atmosphere. The alloy has been annealed in a controlled way in the temperature range of 450 - 800°C for 30 minutes. The kinetics of glass formation and crystallization in composition is studied as affected differential thermal analysis (DTA). Higher content Cr substituted $\text{Fe}_{73.5-x}\text{Cr}_x\text{Nb}_3\text{Cu}_1\text{Si}_{13.5}\text{B}_9$ amorphous alloys upon annealed undergoes phase transformation due to primary crystallization of $\alpha - \text{Fe}(\text{Si})$ and secondary crystallization of Fe_2B phase respectively revealed by DTA and confirmed by XRD. Thermal analysis experiment and from the obtained data activation energy of primary crystallization products $\alpha - \text{Fe}(\text{Si})$ phase are varies 2.35 to 4.88 eV and secondary crystallization products Fe_2B 3.28 to 3.76 eV.

Amorphosity of the ribbon and nanocrystalline state was evaluated by XRD. In the optimized annealing condition the grain size has been obtained in the range of 11 - 30 nm. The primary crystallization phase shifts to higher annealed temperature with Cr content implying the enhancement of thermal stability of the amorphous alloys against crystallization due to increasing amount of Cr. The average grain size of the $\alpha\text{-Fe}(\text{Si})$ phase, almost same under the identical annealing condition as the higher content Cr is increased. The peak shifts indicate the change of the values of Si-content of nanograins and therefore, the change of the values of lattice parameter of nanograins. The saturation magnetization (M_s) and Curie temperature (T_c) of these alloys decrease linearly with the increase of Cr content for the entire composition range due to dilution of Fe magnetic moment and weakening of exchange interaction between of magnetic atoms. The critical composition for disappearance of ferromagnetism fall of curve M_s with the replacement Fe by Cr, where the nearest neighbor coupling is longer dominant and intermediate range occur, giving rise to a significant portion of antiferromagnetic interaction. This causes a weaker exchange interaction among the Fe magnetic moment resulting in a decrease of T_c . This increase of magnetization (M) up to annealed temperature 600°C is connected to the structural

relaxation and varying degrees of chemical disorder with reference to enhancement of M of annealed samples. Crystallization seems to take place and accordingly M Vs H curve sharply rises and look ferromagnetic for $x = 12.5$ which is paramagnetic in the amorphous condition with $T_c = 246K$. This increase of M for the four samples are due to the evolution of ferromagnetic α -Fe(Si) nanograin crystallites.

Contents

	Page No.
Title Page	
Declaration Page	i
Acknowledgement	ii
Abstract	v
Contents	vii
List of Figures	xi
List of Tables	xvi
List of Symbols	xviii

CHAPTER I

INTRODUCTION

1.1	Introduction	1
1.2	The Aim and Objectives of the Present Work	4
1.3	Experimental Reason for Choosing this Research Work	4
1.4	Application of Nanocrystalline Ribbons	6
1.5	Review of Researches on FINEMET	8
1.6	Organization of the Thesis	10

CHAPTER II

PREPARATION ON NANOCRYSTALLINE ALLOY

2.1	Composition of the Nanocrystalline	12
2.2	An overview of Nanocrystalline Materials	13
2.3	Alloy Design Issues	14
2.4	Stages of Evolution of Microstructure	16
2.5	Advantages of Soft Nanocrystalline Alloys	19
2.6	Viscosity Condition for the Formation of Metallic Glass	20
2.7	Condition for the Formation of Nanocrystalline Alloys	20
2.7.1	Methods used for preparation of Nanocrystalline Alloys	21
2.8.1	The Fast Cooling of the Melt	21
2.9	Sample Preparation	22
2.9.1	Master Alloy Preparation	22

2.9.2	Preparation of Ribbon by Melt Spinning Technique	23
2.10	Important Factor to Control the Thickness of Ribbons	25
2.11	Confirmation of Amorphousity of Ribbons	25

CHAPTER III

THEORETICAL BACKGROUND

3.1	Amorphous Alloys or Metallic Glass	27
3.1.1	Nature and Formation of Amorphous Alloys	27
3.1.2	Factor Contributions to Glass Formation and Stability	29
3.2	Structure and Microstructure of Amorphous and Nanocrystalline Alloys	31
3.3	Stability of the Amorphous and Nanocrystalline Materials	32
3.3.1	Characteristics of the Glass Transition Temperature	34
3.4	Differential Thermal Analysis and its Application	35
3.4.1	Evaluation of Activation Energy Based on DTA Technique	36
3.5	Determination of Nanometric Grain Size by X-Ray Diffraction	37
3.5.1	Random Anisotropy Model (RAM)	39
3.6	Magnetic Dipole Moments and Magnetization	44
3.6.1	Magnetization of the Nanocrystalline Ribbon	45
3.6.2	Ferromagnetic ordering (Curie) Temperatures	46

CHAPTER IV

EXPERIMENTAL DETAILS

4.1	Thermal Analysis Technique	47
4.1.1	The principle of Differential Thermal Analysis	48
4.1.2	Apparatus	49
4.1.3	Experimental Factors	51
4.1.4	Interpretation and Presentation of DTA	52
4.2	Annealing	54
4.2.1	Stages	55
4.2.2	Setup and Equipment	55
4.3	Thermal Treatment of the Nanocrystalline Amorphous Ribbon	56
4.4	Powder/Polycrystalline Diffraction	57
4.4.1	Theoretical Consideration of X-Ray Diffraction (XRD)	57

4.4.2	X-Ray Powder Method	58
4.4.3	Experimental Technique for X-Ray Diffractometer	59
4.4.4	Analysis of XRD data	62
4.5	Magnetization Measurement Technique	64
4.5.1	Vibrating Sample Magnetometer (VSM)	64
4.5.2	The Principle of VSM	65
4.5.3	Electronic Circuit of the VSM	66
4.5.3.1	Sensitivity Limits	67
4.5.3.2	Stability Test of Differential Measurements	68
4.5.3.3	Vibration Amplitude	68
4.5.3.4	Image Effects	69
4.5.3.5	Vibration Frequency	69
4.5.3.6	Vibration Problem	69

CHAPTER V

RESULTS AND DISCUSSION

5	Results and Discussion	70
5.1	Crystallization Behavior of Fe-Cr-Cu-Nb-Si-B Alloys	70
5.2	DTA Results of Fe-Cr-Nb-Cu-Si-B ribbons as affected by Cr-content	70
5.2.1	Study of DTA traces of Fe _{66.5} Cr ₇ Nb ₃ Cu ₁ Si _{13.5} B ₉ Alloy	73
5.2.2	Study of DTA Traces of Fe _{64.5} Cr ₉ Nb ₃ Cu ₁ Si _{13.5} B ₉ Alloy	79
5.2.3	Study of DTA traces of Fe _{63.5} Cr ₁₀ Nb ₃ Cu ₁ Si _{13.5} B ₉ Alloy	84
5.2.4	Study of DTA traces of Fe ₆₁ Cr _{12.5} Nb ₃ Cu ₁ Si _{13.5} B ₉ Alloy	90
5.3	Comparison between DTA of Fe-Cr-Cu-Nb-Si-B and original FINEMET	95
5.4	Microstructural Analysis of Amorphous and Nanocrystalline Fe _{73.5-x} Cr _x Nb ₃ Cu ₁ Si _{13.5} B ₉ Alloy by XRD Analysis	97
5.4.1	XRD Analysis of the Nanocrystalline Ribbon with Composition Fe _{66.5} Cr ₇ Nb ₃ Cu ₁ Si _{13.5} B ₉	99
5.4.2	XRD Analysis of the Nanocrystalline Ribbon with Composition Fe _{64.5} Cr ₉ Nb ₃ Cu ₁ Si _{13.5} B ₉	104
5.4.3	XRD analysis of the Nanocrystalline Ribbon with composition Fe _{63.5} Cr ₁₀ Nb ₃ Cu ₁ Si _{13.5} B ₉	108

5.4.4	XRD Analysis of the Nanocrystalline Ribbon with composition $\text{Fe}_{61}\text{Cr}_{12.5}\text{Nb}_3\text{Cu}_1\text{Si}_{13.5}\text{B}_9$	112
5.5	Specific Magnetization Measurement of Fe-Cr-Nb-Cu-Si-B Nanocrystalline Amorphous Ribbons	115
5.5.1	Specific Magnetization at Room Temperature	116
5.5.2	Temperature Dependence of Specific Magnetization Fe-Cr-Nb-Cu-Si-B Nanocrystalline Amorphous Ribbons	118
5.6	Variation of Specific Magnetization with Isothermal Annealing of Higher Cr-content Amorphous Nanocrystalline Alloys.	122
5.6.1	Effect of Annealing Temperature on Specific Magnetization at Room Temperature	124

CHAPTER VI

CONCLUSION

5.1	Conclusion	129
5.2	Scope for Future Work	131

Reference		132
------------------	--	-----

List of Figures

Fig. No	Descriptions	Page No
Fig. 2.1	Flow chart for the consideration in designing and developing nanocrystalline soft magnetic material from an amorphous precursor route	15
Fig. 2.2	Schematic illustration of the formation of nanocrystalline structure	18
Fig. 2.3	FINEMET is superior compared to conventional materials	19
Fig. 2.4	Vacuum Arc Melting Machine	23
Fig. 2.5	Schematic diagram	24
Fig. 2.6	Melt-Spinning Machine	24
Fig. 2.6	X-ray diffraction of as-cast nanocrystalline amorphous ribbons with Composition $Fe_{73.5-x}Cr_xNb_3Cu_1Si_{13.5}B_9$ [$x = 7, 9, 10 \text{ \& } 12.5$]	25
Fig. 3.1	Schematic TTT diagram for the onset of crystallization	28
Fig. 3.2	Volume -Temperature relationship in solid, liquid and glass state	30
Fig. 3.3	Typical pair correlation function for (a) a completely disordered, (b) a crystalline completely ordered and (c) an amorphous short range ordered material	32
Fig. 3.4	Effect of fine particle broadening in XRD (a) fine particle and (b) perfect crystal	38
Fig. 3.5	Schematic representation of Random Anisotropy Model (RAM) (a) Assembly of grains, each of them is having a randomly fluctuating anisotropy axis (b) The correlation volume of size L_{ex} in nanocrystalline material consisting of grains	39
Fig. 4.1 (a)	Heating curve of sample and reference substance	48
Fig. 4.1 (b)	DTA Curve	49
Fig. 4.2	Schematic illustration of a DTA cell	50
Fig. 4.3	Block diagram of a DTA equipment, (S) sample thermocouple, (R) reference thermocouple, (M) monitor thermocouple	51
Fig. 4.4	SII EXSTAR 6000 TG/DTA 6300 assembly	53
Fig. 4.5	MTI - GSL-1600x40 Tube Furnaces	56
Fig. 4.6	Bragg's diffraction pattern	58
Fig. 4.7	Reflection and Transmission geometry of powder diffraction	59
Fig. 4.8	Block diagram of the Bruker AXS D8 Advance XRD system	60
Fig. 4.9	Bruker AXS D8 Advance	61
Fig. 4.10	Vibrating Sample Magnetometer (VSM)	66
Fig. 4.11	Electronic Circuit of the VSM	67

Fig. 5.1	DTA traces of as-cast nanocrystalline amorphous ribbon $\text{Fe}_{73.5-x}\text{Cr}_x\text{Nb}_3\text{Cu}_1\text{Si}_{13.5}\text{B}_9$ [$x = 7, 9, 10$ & 12.5] at the heating rate of $50^\circ\text{C}/\text{min}$	72
Fig. 5.2 (a)	DTA trace of as-cast nanocrystalline amorphous ribbon $\text{Fe}_{66.5}\text{Cr}_7\text{Nb}_3\text{Cu}_1\text{Si}_{13.5}\text{B}_9$ at the heating rate of $10^\circ\text{C}/\text{min}$	73
Fig. 5.2 (b)	DTA trace of as-cast nanocrystalline amorphous ribbon $\text{Fe}_{66.5}\text{Cr}_7\text{Nb}_3\text{Cu}_1\text{Si}_{13.5}\text{B}_9$ at the heating rate of $20^\circ\text{C}/\text{min}$	74
Fig. 5.2 (c)	DTA trace of as-cast nanocrystalline amorphous ribbon $\text{Fe}_{66.5}\text{Cr}_7\text{Nb}_3\text{Cu}_1\text{Si}_{13.5}\text{B}_9$ at the heating rate of $30^\circ\text{C}/\text{min}$	74
Fig. 5.2 (d)	DTA trace of as-cast nanocrystalline amorphous ribbon $\text{Fe}_{66.5}\text{Cr}_7\text{Nb}_3\text{Cu}_1\text{Si}_{13.5}\text{B}_9$ at the heating rate of $40^\circ\text{C}/\text{min}$	75
Fig. 5.2 (e)	DTA trace of as-cast nanocrystalline amorphous ribbon $\text{Fe}_{66.5}\text{Cr}_7\text{Nb}_3\text{Cu}_1\text{Si}_{13.5}\text{B}_9$ at the heating rate of $50^\circ\text{C}/\text{min}$	75
Fig. 5.3	Effects of heating rate on DTA traces of nanocrystalline amorphous ribbons $\text{Fe}_{66.5}\text{Cr}_7\text{Nb}_3\text{Cu}_1\text{Si}_{13.5}\text{B}_9$ at the heating rate of 10 to $50^\circ\text{C}/\text{min}$	76
Fig. 5.4 (a)	Kissinger's plot to determine the activation of Fe(Si) phase for $\text{Fe}_{66.5}\text{Cr}_7\text{Nb}_3\text{Cu}_1\text{Si}_{13.5}\text{B}_9$ alloy	78
Fig. 5.4 (b)	Kissinger's plot to determine the activation of Fe_2B phase for $\text{Fe}_{66.5}\text{Cr}_7\text{Nb}_3\text{Cu}_1\text{Si}_{13.5}\text{B}_9$ alloy	78
Fig. 5.5 (a)	DTA trace of as-cast nanocrystalline amorphous ribbon $\text{Fe}_{64.5}\text{Cr}_9\text{Nb}_3\text{Cu}_1\text{Si}_{13.5}\text{B}_9$ at the heating rate of $10^\circ\text{C}/\text{min}$	79
Fig. 5.5 (b)	DTA trace of as-cast nanocrystalline amorphous ribbon $\text{Fe}_{64.5}\text{Cr}_9\text{Nb}_3\text{Cu}_1\text{Si}_{13.5}\text{B}_9$ at the heating rate of $20^\circ\text{C}/\text{min}$	80
Fig. 5.5 (c)	DTA trace of as-cast nanocrystalline amorphous ribbon $\text{Fe}_{64.5}\text{Cr}_9\text{Nb}_3\text{Cu}_1\text{Si}_{13.5}\text{B}_9$ at the heating rate of $30^\circ\text{C}/\text{min}$	80
Fig. 5.5 (d)	DTA trace of as-cast nanocrystalline amorphous ribbon $\text{Fe}_{64.5}\text{Cr}_9\text{Nb}_3\text{Cu}_1\text{Si}_{13.5}\text{B}_9$ at the heating rate of $40^\circ\text{C}/\text{min}$	81
Fig. 5.5 (e)	DTA trace of as-cast nanocrystalline amorphous ribbon $\text{Fe}_{64.5}\text{Cr}_9\text{Nb}_3\text{Cu}_1\text{Si}_{13.5}\text{B}_9$ at the heating rate of $50^\circ\text{C}/\text{min}$	81
Fig. 5.6	Effects of heating rate on DTA traces of nanocrystalline amorphous ribbon with composition $\text{Fe}_{64.5}\text{Cr}_9\text{Nb}_3\text{Cu}_1\text{Si}_{13.5}\text{B}_9$ at the heating rate of 10°C to $50^\circ\text{C}/\text{min}$	82
Fig. 5.7 (a)	Kissinger's plot to determine the activation of Fe(Si) phase for $\text{Fe}_{64.5}\text{Cr}_9\text{Nb}_3\text{Cu}_1\text{Si}_{13.5}\text{B}_9$ alloy	83
Fig. 5.7 (b)	Kissinger's plot to determine the activation of Fe_2B phase for $\text{Fe}_{64.5}\text{Cr}_9\text{Nb}_3\text{Cu}_1\text{Si}_{13.5}\text{B}_9$ alloy	84
Fig. 5.8 (a)	DTA trace of as-cast nanocrystalline amorphous ribbon $\text{Fe}_{63.5}\text{Cr}_{10}\text{Nb}_3\text{Cu}_1\text{Si}_{13.5}\text{B}_9$ at the heating rate of $10^\circ\text{C}/\text{min}$	85

Fig. 5.8 (b)	DTA trace of as-cast nanocrystalline amorphous ribbon $\text{Fe}_{63.5}\text{Cr}_{10}\text{Nb}_3\text{Cu}_1\text{Si}_{13.5}\text{B}_9$ at the heating rate of $20^\circ\text{C}/\text{min}$	85
Fig. 5.8 (c)	DTA trace of as-cast nanocrystalline amorphous ribbon $\text{Fe}_{63.5}\text{Cr}_{10}\text{Nb}_3\text{Cu}_1\text{Si}_{13.5}\text{B}_9$ at the heating rate of $30^\circ\text{C}/\text{min}$	86
Fig. 5.8 (d)	DTA trace of as-cast nanocrystalline amorphous ribbon $\text{Fe}_{63.5}\text{Cr}_{10}\text{Nb}_3\text{Cu}_1\text{Si}_{13.5}\text{B}_9$ at the heating rate of $40^\circ\text{C}/\text{min}$	86
Fig. 5.8 (e)	DTA trace of as-cast nanocrystalline amorphous ribbon $\text{Fe}_{63.5}\text{Cr}_{10}\text{Nb}_3\text{Cu}_1\text{Si}_{13.5}\text{B}_9$ at the heating rate of $50^\circ\text{C}/\text{min}$	87
Fig. 5.9	Effects of heating rate on DTA traces of nanocrystalline amorphous ribbon with composition $\text{Fe}_{63.5}\text{Cr}_{10}\text{Nb}_3\text{Cu}_1\text{Si}_{13.5}\text{B}_9$ at the heating rate of 10°C to $50^\circ\text{C}/\text{min}$	87
Fig. 5.10 (a)	Kissinger's plot to determine the activation of Fe(Si) phase for $\text{Fe}_{63.5}\text{Cr}_{10}\text{Nb}_3\text{Cu}_1\text{Si}_{13.5}\text{B}_9$ alloy	89
Fig. 5.10 (b)	Kissinger's plot to determine the activation of Fe_2B phase for $\text{Fe}_{63.5}\text{Cr}_{10}\text{Nb}_3\text{Cu}_1\text{Si}_{13.5}\text{B}_9$ alloy	89
Fig. 5.11 (a)	DTA trace of as-cast nanocrystalline amorphous ribbon $\text{Fe}_{61}\text{Cr}_{12.5}\text{Nb}_3\text{Cu}_1\text{Si}_{13.5}\text{B}_9$ at the heating rate of $10^\circ\text{C}/\text{min}$	90
Fig. 5.11 (b)	DTA trace of as-cast nanocrystalline amorphous ribbon $\text{Fe}_{61}\text{Cr}_{12.5}\text{Nb}_3\text{Cu}_1\text{Si}_{13.5}\text{B}_9$ at the heating rate of $10^\circ\text{C}/\text{min}$	91
Fig. 5.11 (c)	DTA trace of as-cast nanocrystalline amorphous ribbon $\text{Fe}_{61}\text{Cr}_{12.5}\text{Nb}_3\text{Cu}_1\text{Si}_{13.5}\text{B}_9$ at the heating rate of $10^\circ\text{C}/\text{min}$	91
Fig. 5.11 (d)	DTA trace of as-cast nanocrystalline amorphous ribbon $\text{Fe}_{61}\text{Cr}_{12.5}\text{Nb}_3\text{Cu}_1\text{Si}_{13.5}\text{B}_9$ at the heating rate of $10^\circ\text{C}/\text{min}$	92
Fig. 5.11 (e)	DTA trace of as-cast nanocrystalline amorphous ribbon $\text{Fe}_{61}\text{Cr}_{12.5}\text{Nb}_3\text{Cu}_1\text{Si}_{13.5}\text{B}_9$ at the heating rate of $10^\circ\text{C}/\text{min}$	92
Fig. 5.12	Effects of heating rate on DTA traces of nanocrystalline amorphous ribbon with composition $\text{Fe}_{61}\text{Cr}_{12.5}\text{Nb}_3\text{Cu}_1\text{Si}_{13.5}\text{B}_9$ at the heating rate of 10°C to $50^\circ\text{C}/\text{min}$	93
Fig. 5.13 (a)	Kissinger's plot to determine the activation of Fe(Si) phase for $\text{Fe}_{61}\text{Cr}_{12.5}\text{Nb}_3\text{Cu}_1\text{Si}_{13.5}\text{B}_9$ alloy	94
Fig. 5.13 (b)	Kissinger's plot to determine the activation of Fe_2B phase for $\text{Fe}_{61}\text{Cr}_{12.5}\text{Nb}_3\text{Cu}_1\text{Si}_{13.5}\text{B}_9$ alloy	95
Fig. 5.14	XRD spectra of $\text{Fe}_{66.5}\text{Cr}_7\text{Nb}_3\text{Cu}_1\text{Si}_{13.5}\text{B}_9$ alloys of annealed at different temperatures at constant annealing time 30 min	100
Fig. 5.15	Change of Si (at. %) content and Lattice Parameter with different annealing temperature for the sample with composition $\text{Fe}_{66.5}\text{Cr}_7\text{Nb}_3\text{Cu}_1\text{Si}_{13.5}\text{B}_9$	102

Fig. 5.16	Change of Grain Size with different annealing temperature for the sample with composition $\text{Fe}_{66.5}\text{Cr}_7\text{Nb}_3\text{Cu}_1\text{Si}_{13.5}\text{B}_9$	103
Fig. 5.17	XRD spectra of $\text{Fe}_{64.5}\text{Cr}_9\text{Nb}_3\text{Cu}_1\text{Si}_{13.5}\text{B}_9$ alloys of annealed at different temperature at constant annealing time 30 min	106
Fig. 5.18	Change of Si (at %) content and Lattice Parameter with different annealing temperature for the sample with composition $\text{Fe}_{64.5}\text{Cr}_9\text{Nb}_3\text{Cu}_1\text{Si}_{13.5}\text{B}_9$	107
Fig. 5.19	Change of Grain Size with different annealing temperature For the sample with composition $\text{Fe}_{64.5}\text{Cr}_9\text{Nb}_3\text{Cu}_1\text{Si}_{13.5}\text{B}_9$	107
Fig. 5.20	XRD spectra of $\text{Fe}_{63.5}\text{Cr}_{10}\text{Nb}_3\text{Cu}_1\text{Si}_{13.5}\text{B}_9$ alloys of annealed at different temperatures at constant annealing time 30 min	109
Fig. 5.21	Change of Si (at. %) content and Lattice Parameter with different annealing temperature for the sample with composition $\text{Fe}_{63.5}\text{Cr}_{10}\text{Nb}_3\text{Cu}_1\text{Si}_{13.5}\text{B}_9$	110
Fig. 5.22	Change of Grain Size with different annealing temperature for the sample with composition $\text{Fe}_{63.5}\text{Cr}_{10}\text{Nb}_3\text{Cu}_1\text{Si}_{13.5}\text{B}_9$	111
Fig. 5.23	XRD spectra of $\text{Fe}_{61}\text{Cr}_{12.5}\text{Nb}_3\text{Cu}_1\text{Si}_{13.5}\text{B}_9$ alloys of annealed at different temperature at constant annealing time 30 min	113
Fig. 5.24	Change of Si (at. %) content and Lattice Parameter with different annealing temperature for the sample with composition $\text{Fe}_{61}\text{Cr}_{12.5}\text{Nb}_3\text{Cu}_1\text{Si}_{13.5}\text{B}_9$	114
Fig. 5.25	Change of Grain Size with different annealing temperature for the sample with composition $\text{Fe}_{61}\text{Cr}_{12.5}\text{Nb}_3\text{Cu}_1\text{Si}_{13.5}\text{B}_9$	115
Fig. 5.26	Field dependence of magnetization of amorphous $\text{Fe}_{73.5-x}\text{Cr}_x\text{Nb}_3\text{Cu}_1\text{Si}_{13.5}\text{B}_9$ ribbons with $x = 7, 9, 10$ & 12.5 alloys at room temperature	117
Fig. 5.27	Variation of Saturation magnetization due to change in the Cr-content in $\text{Fe}_{73.5-x}\text{Cr}_x\text{Nb}_3\text{Cu}_1\text{Si}_{13.5}\text{B}_9$ nanocrystalline ribbons at constant applied field 10kOe	118
Fig. 5.28 (a)	Temperature dependence of specific magnetization of amorphous nanocrystalline ribbons with composition $\text{Fe}_{66.5}\text{Cr}_7\text{Nb}_3\text{Cu}_1\text{Si}_{13.5}\text{B}_9$ alloy	120
Fig. 5.28 (b)	Temperature dependence of specific magnetization of amorphous nanocrystalline ribbons with composition $\text{Fe}_{64.5}\text{Cr}_9\text{Nb}_3\text{Cu}_1\text{Si}_{13.5}\text{B}_9$ alloy	120

Fig. 5.28 (c)	Temperature dependence of specific magnetization of amorphous nanocrystalline ribbons with composition $\text{Fe}_{63.5}\text{Cr}_{10}\text{Nb}_3\text{Cu}_1\text{Si}_{13.5}\text{B}_9$ alloy	121
Fig. 5.29	Temperature dependence of specific magnetization of amorphous nanocrystalline ribbons with composition $\text{Fe}_{61}\text{Cr}_{12.5}\text{Nb}_3\text{Cu}_1\text{Si}_{13.5}\text{B}_9$ alloys at constant applied field 10kOe	121
Fig. 5.30	$\frac{dM}{dT}$ versus temperature curve of amorphous Nanocrystalline ribbons with composition $\text{Fe}_{73.5-x}\text{Cr}_x\text{Nb}_3\text{Cu}_1\text{Si}_{13.5}\text{B}_9$ [$x = 7, 9, 10 \text{ \& } 12.5$]	122
Fig. 5.31	Field dependence of specific magnetization curves of amorphous nanocrystalline ribbons with composition $\text{Fe}_{66.5}\text{Cr}_7\text{Nb}_3\text{Cu}_1\text{Si}_{13.5}\text{B}_9$ alloy in the as-cast and different annealed samples	125
Fig. 5.32	Field dependence of specific magnetization curves of amorphous nanocrystalline ribbons with composition $\text{Fe}_{64.5}\text{Cr}_9\text{Nb}_3\text{Cu}_1\text{Si}_{13.5}\text{B}_9$ alloy in the as-cast and different annealed samples	126
Fig. 5.33	Field dependence of specific magnetization curves of amorphous nanocrystalline ribbons with composition $\text{Fe}_{63.5}\text{Cr}_{10}\text{Nb}_3\text{Cu}_1\text{Si}_{13.5}\text{B}_9$ alloy in the as-cast and different annealed samples	126
Fig. 5.34	Field dependence of specific magnetization curves of amorphous nanocrystalline ribbons with composition $\text{Fe}_{61}\text{Cr}_{12.5}\text{Nb}_3\text{Cu}_1\text{Si}_{13.5}\text{B}_9$ alloy in the as-cast and different annealed samples	127

List of Tables

Table. No	Descriptions	Page No
Table 3.1	Spontaneous and room temperature magnetizations, magnetic dipole moments and Curie temperature for elemental ferromagnets	44
Table 5.1	Onset temperature of 1 st and 2 nd crystallization states of the nanocrystalline amorphous ribbons with composition $Fe_{73.5-x}Cr_xNb_3Cu_1Si_{13.5}B_9$ [$x = 7, 9, 10$ & 12.5] alloy during continuous heating rate $50^{\circ}C/min$	71
Table 5.2	Effect of heating rate on 1st and 2nd crystallization states of the nanocrystalline amorphous ribbon with composition $Fe_{66.5}Cr_7Nb_3Cu_1Si_{13.5}B_9$	77
Table 5.3	Effect of heating rate on 1st and 2nd crystallization of the nanocrystalline amorphous ribbon with composition $Fe_{66.5}Cr_7Nb_3Cu_1Si_{13.5}B_9$ state's calculative data for activation energy calculation data	78
Table 5.4	Effect of heating rate on 1st and 2nd crystallization states of the nanocrystalline amorphous ribbon with composition $Fe_{64.5}Cr_9Nb_3Cu_1Si_{13.5}B_9$	82
Table 5.5	Effect of heating rate on 1st and 2nd crystallization of the nanocrystalline amorphous ribbon with composition $Fe_{64.5}Cr_9Nb_3Cu_1Si_{13.5}B_9$ state's calculative data for activation energy calculation data	83
Table 5.6	Effect of heating rate on 1 st and 2 nd crystallization states of the nanocrystalline amorphous ribbon with composition $Fe_{63.5}Cr_{10}Nb_3Cu_1Si_{13.5}B_9$	88
Table 5.7	Effect of heating rate on 1 st and 2 nd crystallization of the nanocrystalline amorphous ribbon with composition $Fe_{63.5}Cr_{10}Nb_3Cu_1Si_{13.5}B_9$ for activation energy calculation data	88
Table 5.8	Effect of heating rate on 1 st and 2 nd crystallization states of the nanocrystalline amorphous ribbon with composition $Fe_{61}Cr_{12.5}Nb_3Cu_1Si_{13.5}B_9$	93
Table 5.9	Effect of heating rate on 1 st and 2 nd crystallization states of the nanocrystalline amorphous ribbon with composition $Fe_{61}Cr_{12.5}Nb_3Cu_1Si_{13.5}B_9$ for activation energy calculation data	94
Table 5.10	crystallization states (heating rate $20^{\circ}C/min$) and activation energy of different phases of nanocrystalline amorphous ribbons with composition $Fe_{73.5-x}Cr_xNb_3Cu_1Si_{13.5}B_9$ [$x = 7, 9, 10$ & 12.5]	96

Table 5.11	Experimental XRD data of nanocrystalline $\text{Fe}_{66.5}\text{Cr}_7\text{Nb}_3\text{Cu}_1\text{Si}_{13.5}\text{B}_9$ for different annealing temperature	102
Table 5.12	Experimental XRD data of nanocrystalline $\text{Fe}_{64.5}\text{Cr}_9\text{Nb}_3\text{Cu}_1\text{Si}_{13.5}\text{B}_9$ amorphous ribbon at different annealing temperatures	107
Table 5.13	Experimental XRD data of nanocrystalline $\text{Fe}_{63.5}\text{Cr}_{10}\text{Nb}_3\text{Cu}_1\text{Si}_{13.5}\text{B}_9$ amorphous ribbon at different annealing temperatures	110
Table 5.14	Experimental XRD data of nanocrystalline $\text{Fe}_{61}\text{Cr}_{12.5}\text{Nb}_3\text{Cu}_1\text{Si}_{13.5}\text{B}_9$ amorphous ribbon at different annealing temperatures	114
Table 5.16	Curie temperature and saturation magnetization of nanocrystalline amorphous ribbons with $\text{Fe}_{73.5-x}\text{Cr}_x\text{Nb}_3\text{Cu}_1\text{Si}_{13.5}\text{B}_9$ alloys	117
Table 5.17	The values of saturation magnetization of $\text{Fe}_{73.5-x}\text{Cr}_x\text{Nb}_3\text{Cu}_1\text{Si}_{13.5}\text{B}_9$ [$x = 7, 9, 10 \text{ \& } 12.5$] alloys at different annealing temperature with constant annealing time 30 minutes and constant applied field 10kOe	124

List of Symbols

a_0	=	Lattice parameter
B	=	Magnetic induction
D_g	=	Grain size
DTA	=	Differential Thermal Analysis
DSC	=	Differential Scanning Calorimetry
d	=	Average diameter
FWHM	=	Full Width at Half Maximum
H	=	Magnetic field
H_c	=	Coercivity
H_a	=	Applied magnetic field
$[hkl]$	=	Miller Indices
k	=	Magnetic hardness parameter
K_B	=	Boltzmann's constant
K_{eff}	=	Effective magnetic anisotropy constant
L	=	Self inductance of the sample core
L_0	=	Inductance of the winding coil without sample
L_{ex}	=	Ferromagnetic exchange length
M	=	Magnetization
M_s	=	Saturation magnetization
nm	=	nano meter
NM	=	Nobel metal
RAM	=	Random anisotropy model
RDF(r)	=	Radial Distribution Function
S	=	Total spin angular momentum
T_{ij}	=	Exchange interaction between atoms at the position r_i and r_j .
TTT	=	Temperature, time & transformation
T_a	=	Annealing temperature
T_c	=	Curie temperature
T_g	=	Glass transition temperature
T_x	=	Crystallization temperature
T_m	=	Melting point temperature
T_{x_1}	=	Primary crystallization temperature
T_{x_2}	=	Secondary crystallization temperature

T_{p1}	=	Primary crystallization peak temperature
T_{p2}	=	Secondary crystallization peak temperature
VSM	=	Vibrating Sample Magnetometer
XRD	=	X-ray diffraction
μ	=	Permeability
λ	=	Wave length
θ	=	Scattering angle
t_0	=	Time constant
β	=	Heating rate
δ_w	=	Domain wall Width
σ	=	Effective stress
$\rho(r)$	=	Atomic density
$\langle K \rangle$	=	Average anisotropy
T_c^{am}	=	Curie temperature of residual amorphous matrix
ΔH	=	Enthalpy of crystallization
ΔE	=	Activation Energy

CHAPTER I

INTRODUCTION

INTRODUCTION

1.1 Introduction

Magnetism is a discipline, which stimulated by both basic and practical motivations for the study of different nanostructures. Those nanostructured materials are distinguished from conventional polycrystalline materials by the size of the crystallites that compose them. This thesis focuses on exploiting some of the scientific and technological aspect of nanostructured magnetic materials. Nanomaterials are generally materials that can have one dimension, two dimension or three dimension and can be specified within a size of 100 nanometer ($1\text{nm}=10^{-9}\text{m}$). As the size reduces into the nanometer range, the materials exhibit peculiar and interesting physical, chemical, mechanical, magnetic and electrical properties compared to conventional coarse grained counterpart [1.1]. This new field based on nanomaterials has been named as nanotechnology and emerged as a new branch of science and technology, which is quite diverse and incorporates fields ranging from microelectronics to molecular biology [1.2]. But with the tremendous advancement of science and technology for the last two decades the idea that we should be able to economically arrange atoms in most of the ways permitted by physical law has gained fairly general acceptance.

Nanomaterials can be classified into nanocrystalline materials and nanoparticles. The first are polycrystalline bulk materials devitrified from the synthesized amorphous precursor through appropriate thermal treatment with grain size into nanometer range ($<100\text{nm}$) while the last refers to ultrafine dispersive particles with diameters $<100\text{nm}$. Nanoparticles are interesting from the fundamental point of view due to their extremely small size. The increasing surface to volume ratio with decreasing size results in an increased significance of the grain boundaries (i.e. surface energies) especially in the "real" nanometer range ($\leq 10\text{nm}$).

Nanocrystalline ferromagnetic material offer a new possibilities for tailoring advantageously a variety of phenomena including soft, hard and superparamagnetic behavior. The detailed properties depend upon the interaction mechanism and on the ratio between structural and magnetic correlation length. Over the past several decades, amorphous and more recently nanocrystalline materials have been investigated for applications in magnetic devices requiring magnetically soft materials

such as transformers, inductive devices, etc. Most recently, research interest in nanocrystalline soft magnetic alloys has dramatically increased. This is due to impart of the properties common to both amorphous and crystalline materials and the ability of these alloys to compete with their amorphous and crystalline counterparts. The benefits found in the nanocrystalline alloys stem from their chemical and structural variations on a nanoscale which are important for developing optimal magnetic properties.

Amorphous soft magnetic alloys are now well accepted and matured materials. Basically these are two groups of amorphous alloys. On the one hand the Fe-rich magnetic alloys which exhibit the highest saturation densities among the amorphous materials and which are based on inexpensive raw materials. The Co-based metallic glasses on the other hand are distinguished by their low or vanishing magnetostriction leading to highest permeability and lowest core losses. Both groups of metallic glasses are for current commercial use. Fe-rich alloys are mainly used in power electrical devices whereas the Co-based alloys dominate in inductive components for electronics. The losses of the magnetic materials used in this type of high frequency device can be controlled by the ribbon thickness.

In the present work we are dealing with third variant for the processing of nanocrystalline magnetic materials. In this method an amorphous precursor in the form of ribbons typically 20-30 μ m thick (metallic glass) is first obtained from the melt of the parent ingot with appropriate composition using a melt-spinning machine by rapid solidification technique. Since amorphous state is metastable, upon controlled crystallization above the crystallization temperature develops nanocrystalline grains dispersed in a residual amorphous matrix. Magnetic nanocomposites composed of nanosized magnetic crystal of 10-15nm embedded in an amorphous matrix have been shown to display excellent soft magnetic properties and found their applications in transformers, inductive device, etc. [1.3-1.4]. The properties of the isolated grains change drastically as their size is reduced to nanometer range. When these nanometric grains are consolidating to form a nanostructural material, the magnetic properties are largely determined by the grain size and the exchange interaction between the adjacent grains [1.5]. Amorphous alloys provide an extremely covariant precursor material for the preparation of nanocrystals through the crystallization process controlled by thermal treatment [1.6-1.8].

In 1988 Yoshizawa, Oguma and Yamauchi at Hitachi Metals Ltd. developed the first nanocrystalline ultra soft magnetic alloy called FINEMET having composition $Fe_{73.5}Nb_3Cu_1Si_{13.5}B_9$ from the Fe-Si-B amorphous alloys to which the addition of Cu and Nb were added [1.9]. This newly developed material is cost effective and exhibits best soft magnetic properties. The FINEMET consists of a two – phase microstructure in its optimally annealed condition. This microstructure is made up of a ferromagnetic bcc α -Fe(Si) phase and / or Do_3 type of ordered Fe(Si) phase with grain size of 10-15 nm embedded in this residual ferromagnetic amorphous matrix of about 1-2nm thickness. These represent a new family of excellent soft magnetic core materials and have stimulated an enormous research activity due to their potential applications [1.10-1.13]. The formation of this particular structure is attributed to the combined effects of Cu and Nb and their low solubility in bcc Fe. Cu is thought to promote the nucleation of Fe(Si) grains while Nb hinders their growth and inhibits the formation of ferromagnetic Fe-B phases, which are contrary to the soft magnetic properties. The theoretical understanding of the nanometric grain with magnetic softness has been consolidated in the light of random anisotropy model (RAM) as proposed by Alben *et. al.*[1.14], on the basis of RAM showed that the extraordinary soft magnetic properties of nanocrystalline materials arise due to strong inter granular magnetic coupling, the suppression of effective magnetocrystalline anisotropy and vanishing magnetostriction. The magnetocrystalline anisotropy vanishes when the grain size is smaller than the ferromagnetic exchange length and magnetostriction goes towards zero due to the cancellation of the positive magnetostriction of α -Fe(Si) crystallites and negative magnetostriction of the amorphous matrix.

The effect of partial substitution of Co [1.15-1.16], Al [1.17-1.18] Cr-Mo [1.19] and Cr [1.20] to Fe has been investigated. Replacement of Fe by Cr enhances the thermal stability against crystallization and lowers the Curie temperature (T_c) of the amorphous phase. This gives the opportunity of studying the magnetic interaction in a wider temperature range between the Curie temperature of the amorphous phase (T_c^{am}) and that of nanocrystalline phase (T_c^{crs}). The magnetocrystalline higher content Cr substituted Fe-based metallic glasses under optimum heat treatment is the subject of intensive research not only for the promising technological applications but the co-

existence of various magnetic phases at elevated temperature makes them attractive for studying basic magnetic phenomena.

1.2 The Aim and Objectives of the Present Work

The main objective of the present work is the importance of Cr-substituted Fe-based nanocrystalline ribbon there is scope for studying the phase constitution and magnetic properties for the composition $\text{Fe}_{73.5-x}\text{Cr}_x\text{Nb}_3\text{Cu}_1\text{Si}_{13.5}\text{B}_9$ [$x = 7, 9, 10$ & 12.5]. Find out the optimum composition and grain distributions affecting the magnetic properties of this system.

The objectives of the research works are as follows:

- Synthesis of the FINEMET alloys in the form of the ribbon with varying amount of Cr and Fe in the amorphous state rapid solidification technique.
- Growth of nanocrystals on amorphous matrix by thermal treatment.
- The formation nanocrystals with grain size distributions as affected by heat treatment with varying temperature and holding time will be studied by XRD.
- Correlation of the evaluation of nanograins with the magnetic properties.
- Optimization of annealing temperature corresponding to the magnetization of these nanocrystalline ribbons.

1.3 Experimental Reason for Choosing this Research Work

In the present work, soft magnetic amorphous FINEMET type alloy nominal composition of $\text{Fe}_{73.5-x}\text{Cr}_x\text{Nb}_3\text{Cu}_1\text{Si}_{13.5}\text{B}_9$ synthesized by a melt spinning technique. To improve the magnetic properties of this amorphous ribbon, microstructure is an important parameter that can be controlled by heat treatment condition. Also one effective way of preparing nanocrystalline alloy via the amorphous state of material is an appropriate heat treatment that has been found leading to two phase crystallization. The nanostructures are often obtained primary crystallization. As a consequence, the aim of current evolution is a function of heat treatment temperature. The optimum heat treatment has been found out by trial and error to obtain nanocrystalline phase in a minority amorphous matrix. Amorphousity of the sample has been checked by X-ray diffraction.

The pioneer alloy composition $\text{Fe}_{73.5}\text{Nb}_3\text{Cu}_1\text{Si}_{13.5}\text{B}_9$ known as FINEMET, has been thoroughly studied due to its novel magnetic properties. Yoshizawa *et. al.*

[1.3] and Noh *et. al.* [1.21] studied the effect of Cu on the crystallization behavior in $\text{Fe}_{73.5-x}\text{Cr}_x\text{Nb}_3\text{Cu}_1\text{Si}_{13.5}\text{B}_9$ for $x = 0$ and $x = 1$. The crystallization behavior of this $x = 0$ alloy is quite different and leads to a severe degradation of the soft magnetic properties compared to the original amorphous state. They also found that the average grain size just after the onset of crystallization is relatively large, up to about 60nm with a broad scatter, and show a distinct variation with the annealing temperature. This indicates that the significantly lower nucleation rate than in the Cu-doped alloy whose fine grain size is almost constant in a wide range of annealing temperature. Furthermore annealing of the Cu-free alloy leads to the simultaneous or sequential formation of several crystalline phases. A small Cu addition yields two clearly separated crystallization peaks corresponding to the primary crystallization of bcc Fe at T_{x_1} and subsequently to the precipitation of Fe-B compound at T_{x_2} . Cu addition effect is considerably promoted by the simultaneous presence of Niobium (Nb) enhances the crystallization temperature and retards the grain growth by limiting diffusion. In particular, the Nb addition significantly increases the separation between the two crystallization stages, which promotes the primary crystallization of bcc Fe and stabilizes the residual amorphous matrix against the precipitation of Fe-B compounds. All together this leads to an increased number of simultaneously growing and completing crystals resulting in the nanoscaled microstructure upon alloying at least about 2.3 at. % Nb.

Nb can be substituted by other group V or VI group refractory element like Cr, V, Mo, W or Ta which act similarly on the crystallization process and on the magnetic properties [1.22]. Like Nb, the atomic volume of these refractory elements are larger than that of Fe which reduces the diffusion co-efficient and, thus stabilizes the amorphous matrix and slows down the kinetics of grain coarsening [1.23-1.24]. Accordingly the efficiency of these elements for grain size refinement increases in the order of their atomic volumes i.e. $\text{Cr} < \text{V} < \text{Mo} \approx \text{W} < \text{Nb} \approx \text{Ta}$. Thus, finest grain structures and superior magnetic properties in particle require at least a certain amount of the elements Nb or Ta.

Our composition of a primary crystal differ from that of an amorphous matrix, the process of crystal growth becomes diffusion controlled. In order to control the growth process of nanostructured alloys, it is important to investigate the kinetics of crystallization. The crystallization of these metallic glasses enables the study of both

nucleation and growth process. Thus the main aim of this thesis is to present techniques and model to observe and describe the kinetics of solid phase transformation taking place on the nanoscale, i.e. a study of nanocrystallization which promotes the evolution of superior soft magnetic properties in the studied composition.

In this research work, the kinetics of crystallization of amorphous FINEMET type alloys was investigated by the use of Differential Thermal Analysis (DTA) and X-ray Diffraction (XRD) techniques. The combination of these two techniques is necessary for the complete description of the processes occurring during the nanocrystallization from amorphous precursors as well as microstructural evolution in FINEMET type alloys in its crystalline state. Results have been aided in interpreting the effect of heat treatment on magnetic properties and application type of alloys. Optimum annealing temperature would be ascertained through isothermal annealing over a wide range of temperature. An estimation of the volume fraction of the nanocrystalline Fe-Si phase has been ascertained from the thermo magnetic measurement depending on the annealing temperature. The Curie temperature has been determined by specific magnetization verses temperature measurement with the help of a oven using a Vibrating Sample Magnetometer (VSM). Magnetizations of the sample have been measured as a function of field and anneal effect using VSM.

The main study of the present work are the higher percentage Cr-substituted Fe-based nanocrystalline alloys of the above mentioned composition in the amorphous states by using rapid solidification technique and their magnetic properties with the evolution of different phases by varying annealing conditions. The experimental results have been analyzed and interpreted theoretically some possible technological applications of these nanostructured soft magnetic materials will be suggested.

1.4 Application of Nanocrystalline Ribbons

The key beneficial feature of amorphous alloys lied in their low losses but this was at the price of lower induction. The standard for power devices applications that were considered included power transformers, magnetic shields, acoustic delay lines, tensile stress transducers and transverse filters. The properties of amorphous magnetic alloys with respect to application in electronics, in particular saturation inductors,

permeabilities, hysteretic and eddy current losses and magneto electric properties were considered. Application for amorphous magnets that were suggested included

- (i) 400 Hz power transformers
- (ii) Inductive components for switch mode power supplies
- (iii) Magnetic shields
- (iv) Magneto-electric transducers
- (v) Magnetic heads for data storage applications and
- (vi) Magnetic springs.

Materials requirements for conventional magnetic heads include: (a) large permeabilities (b) large Saturation inductions (c) large electrical resistivities, mechanical hardness and wire resistance.

The attenuation of pulse voltage in choke coils was improved using FINEMET cores as compared with Fe-based amorphous materials. These choke coils can be used over a wide frequency range as well as for protection from high voltage noise caused by lightning. Soft magnetic properties require that nanocrystalline grains be exchange coupled and therefore any of the processing routes based on powder production must be coupled with a compaction method in which the magnetic nanoparticles end up exchange coupled.

Nanocrystallization of amorphous precursors will also require compaction to produce shapes and to improve mechanical properties, as ribbons are quite brittle after nanocrystallization. The soft magnetic properties required for rotor applications in the electric aircraft are in some senseless restrictive than those for the applications of FINEMET. Permeabilities of $10^2 - 10^3$ are sufficient for this application. The frequency requirements, based on 10,000 rpm rotor speeds and 6 flux changes per cycle, require these permeabilities to only 1 KHz. The attractive technical characteristic of nanocrystalline alloys has no microstructural discontinuities such as dislocations, grain boundaries as or precipitates. This significantly reduces the possible pinning sites for domain walls, reducing the coercivity. The absence of microstructural discontinuities resulted in improved corrosion resistance. The highly elastic behavior of these alloys makes them less prone to degradation during handling.

1.5 Review of Researches on FINEMET

It has been well established by the time through extensive research work that the addition of Cu and Nb simultaneously with Fe-Si-B based amorphous alloys is the necessary condition for the extraordinary soft magnetic properties of the FINEMET alloy. This addition extends the temperature range between the primary crystallization α -Fe(Si) temperatures T_{x_1} and secondary crystallization Fe-B temperature, T_{x_2} premiere for achieving superior magnetic properties [1.25]. It should be stressed again that good soft magnetic properties require not only a small grain size but at the same time the absence of boron compounds.

The formation of typical nanocrystalline structure is given by a primary crystallization process before the stable or meta-stable inter atomic phases are formed obviously this can be attained by (i) alloying additions which lead clearly separated stages of crystallization at T_{x_1} and T_{x_2} and (ii) by annealing at $T_{x_1} < T_a < T_{x_2}$ such that only the phase forming at and above T_{x_1} is crystallizing. Murillo *et al.* [1.26] studied the influence of Cu/Nb content and annealing conditions on the microstructure and the magnetic properties of FINEMET alloys. Grain size, phase composition and transition temperatures were observed to depend on the ratio of Cu/Nb content. Amorphous ferromagnetic material based on Fe-Si-B show good magnetic properties when they are heat treated below their crystallization temperature while the Fe-Cu-Nb-Si-B alloys exhibit extraordinary high permeability, two orders of magnitude higher than their conventional Fe-Si-B alloys due to heat treatment just above the crystallization temperature for a specific time. The great scope of technical application this material $Fe_{73.5} Nb_3 Cu_1 Si_{13.5} B_9$ arise from this freedom of tailoring the magnetic properties [1.27-1.30].

The study of Yoshizawa *et al.* [1.3] and Noh *et al.* [1.2] on the role of nucleating agent Cu on the crystallization behavior of the composition $Fe_{73.5} Nb_3 Cu_1 Si_{13.5} B_9$ revealed that the average grain size is relatively large at crystallization temperature due to lower crystallization rate with no addition of Cu and annealing of this Cu free alloy leads to simultaneous or sequential formation of several crystalline phases. Kataoka *et al.* [1.31] verified the role of Au in place of Cu and reported the Au is the only element, which has a comparable effect on the crystallization behavior. They also found that the average grain size just after the onset of crystallization is relatively large up to about 60nm with a broad scatter and show a distinct variation

with the annealing temperature. This indicates the significantly lower nucleation rate than in the Cu-doped alloy whose finer grain size is almost constant in a wide range of annealing temperature [1.32].

Inoue *et al.* [1.33] observed that group IVa and VIa transition metals extends the glass forming range at low Si or B contents. The glass forming range is the widest for Hf containing alloys and decreases in the order. According to Suzuki *et al.* [1.34-1.35] the glass forming ability is considerably improved with the addition of Hf or Zr.

Herzer [1.36] studied on Curie temperature and permeability of nanocrystalline material. According to measuring temperature approaches the Curie point of the inter-granular amorphous phase, the exchange coupling between the crystallites is largely reduced. As a result, the initial permeability drops down. As reported by Hakim *et al.* [1.37] and S. Manjura Haque *et al.* [1.38], magnetic initial permeability of nanocrystalline amorphous ribbon strongly depends on annealing temperature and exhibits super paramagnetic behavior at $T > T_c^{am}$. When T_c^{am} , the grain coupling is largely but not interrupted above T_c^{am} and still persists to higher value of permeability compared to annealed temperature at T_c^{am} exhibiting the magnetic coupling between particles is significant. The precise coupling mechanism for this type of behavior at $T > T_c^{am}$ may be explained in terms of exchange penetration through thin paramagnetic inter-granular layer and / or dipolar interactions.

Franco *et al.* [1.39] also studied the super paramagnetic relaxation in FINEMET type of alloy Fe-Cu-Nb-Si-B without adding any extra refractory element and they have demonstrated that, this behavior is a general characteristics of this nanocrystalline alloys provided the volume fraction of crystallites are very low. If the size of the nanocrystals is small enough and the inter-granular amorphous matrix is sufficiently thick to minimize the magnetic interactions between them, of the nanocrystalline particles is expected.

Magnetic and structural properties of FINEMET alloy and with the substitution of Nb by Ta, Mo and Cr, W have been studied by several investigators [1.40-1.41]. Results show that FINEMET composition with Nb and Ta show similar soft magnetic characteristics while alloy with substitution of Nb and Cr, Mo and W display somewhat lower soft magnetic properties. Hakim *et al.* [1.11] found with the Ta substituted alloy super paramagnetic and super ferromagnetic behavior depending upon the volume fraction of the nanocrystallites from the temperature dependence of permeability of the samples annealed in the temperature range 500 - 575°C. Similar

behavior of super paramagnetic has been observed in the FINEMET alloy with higher content of Cr substituted for Fe [1.42-1.43]. Magnetic properties of partial substitution of Fe by Cr have been studied by several investigators with a limited concentration of Cr between 1 and 5 at. % substituted for Fe in the FINEMET alloy [1.44-1.46]. The authors found that Cr enhances the crystallization temperature, controls the volume fraction and particle size of α -Fe(Si) phase and reduces the Curie temperature. The influence of Cr content with higher percentage of Cr on the magnetization behavior of $\text{Fe}_{73.5-x}\text{Cr}_x\text{Nb}_3\text{Cu}_1\text{Si}_{13.5}\text{B}_9$ alloys have been studied [1.47]. It has been found that magnetic moment and the T_c decreases linearly with Cr concentration. The onset of ferromagnetism for the alloy system studied has been claimed to be $\text{Cr} < 27$ at. % and the alloys have been found to follow the Bloch's $T^{3/2}$ - law in their temperature dependence of magnetization.

The effect of annealing temperature on saturation magnetization (M_s) has been reported by Lovas *et al.* [1.48] and Berkowitz [1.49]. M_s is increased with annealing temperature up to initial stage of crystallization temperature and then decreases correspond to the optimum nanocrystallized state with high volume fraction of Fe(Si) nanograins. The influences of Cr content with higher percentage of Cr on the magnetization behavior of $\text{Fe}_{73.5-x}\text{Cr}_x\text{Nb}_3\text{Cu}_1\text{Si}_{13.5}\text{B}_9$ alloys have been studied.

1.6 Organization of the Thesis

The thesis has been divided into six chapters. Chapter I general introduction followed by The aim and objectives of the present work, reason for choosing this research work, application of nanocrystalline ribbons, review of researches on FINEMET and organization of the thesis. In Chapter II, the preparation procedures of the nanocrystalline alloys are described. In Chapter III, the theoretical background of the stability of amorphous alloys, theories of magnetization are discussed.

In Chapter IV, the experimental details including Differential Thermal Analysis (DTA), X-ray Diffraction (XRD) analysis, and Vibrating Sample Magnetometer (VSM) are described. In Chapter V, the details results regarding DTA, activation energy, corresponding crystallization temperature, XRD method after heat treatment of the sample at different temperatures, Lattice parameter, Silicon content, Grain size determination, field dependence of specific magnetization and annealing effects on saturation specific magnetization are discussed.

And in Chapter VI, contains conclusion, achievement of works and further suggestion of this work.

Finally a complete list of reference has been given towards the end of the chapters.

CHAPTER II

PREPARATION ON NANOCRYSTALLINE ALLOY

PREPARATION ON NANOCRYSTALLINE ALLOY

2.1 Composition of the Nanocrystalline

The study of magnetic glass dates back to the pioneering work of Pol Duwez at Caltech in the 1950s. Duwez employed atomization [2.1] prior to splat quenching [2.2-2.4]. Ferromagnetic amorphous alloys were first reported by Mader and Nowik [2.5]. Soon after, Tsuei and Duwez [2.6] reported splat quenched amorphous ferromagnetic with interesting soft magnetic properties.

Generally the optimum mechanical and magnetic properties of nanocrystalline soft magnetic materials are obtained for partially crystallized materials. This means that those materials are formed in two phases [2.7]. In general nanocrystalline alloys can be described as $TL_{1-x}(TE, M, NM)_x$ where

- TL denotes a late ferromagnetic transition metal element (TL= Co, Ni or Fe)
- TE denotes an early transition metal element (TE = Zr, Nb, Hf, Ta etc.)
- M is metalloid (M = B, P, Si, etc.) and
- NM is a noble metal (NM=Cu, Ag, Au etc.)

This composition usually has $x < 0.02$ i.e. with as much late ferromagnetic transition metal (TL of Fe, Co or Ni) as possible. The remaining early transition metals (TE = Zr, Nb, Hf, Ta, etc.) and metalloids (B, P, Si, etc.) are added to promote glass formation in the precursor. The noble metal elements (NM = Cu, Ag, Au, etc.) serve as nucleating agents for the ferromagnetic nanocrystalline phase. The compositions are limited by where glass formation can occur prior to the nanocrystallization route. These alloys may be single phase (Type-I) but are generally two phase materials with a nanocrystalline ferromagnetic phase and a residual amorphous phase at the grain boundaries (Type-II). The type-II nanocrystalline alloys might have been general properties:

- Relatively high resistivity (50 - 80 $\mu\Omega$ -cm)
- Low magnetocrystalline anisotropy and
- Increase mechanical strength

With properties such as these, nanocrystalline alloys have great potential as soft magnetic properties. In the ongoing research we are interested about the type-II.

One of the important features of this magnetic system is that one can play with different compositions, annealing temperatures and time to control the grain size and

their distribution upon, which the magnetic properties of these new materials strongly depend. In choosing the composition, one has to consider the magnetic component like Fe, Co or Ni, the crystallization initiating component e.g. Cu and the component Nb for stabilizing the nanocrystal by inhibiting the grain growth and glass forming materials like Si, B, etc.

Nanocrystalline soft magnetic alloys have received considerable attention due to their excellent soft magnetic properties [2.8]. Small addition of Cu and Nb into Fe-Si-B amorphous materials changes considerable their crystallization process, which is executed under appropriately controlled conditions and the specific purpose of these addition are

- The element is used for helping the formation of nuclei and ultra-fine grain and
- The element is used to impede the growth of the crystallites.

In this material, the nanocrystalline state is composed of a fine structure of α -Fe(Si) and is usually around 10nm. For such as average grain size the exchange interaction dominates the magnetic behavior of randomly oriented crystallites guided by random anisotropy [2.9]. In the present thesis work nanocrystalline alloys are prepared by partial substitution of Fe by Cr of FINEMET $Fe_{73.5}Nb_3Cu_1Si_{13.5}B_9$.

2.2 An overview of Nanocrystalline Materials

Nanocrystalline amorphous ribbon can be considered as an off-shoot of amorphous materials. In fact nanocrystalline amorphous ribbon is a composite material where nanocrystals are embedded in an amorphous matrix. Nanocrystalline materials represent one of the most active research areas in recent times for the atomic tailoring of materials with specific properties and property combinations. However, it is still in its infancy since its emergence as potential material has just began at this stage of development. There have been glimpses of exciting new properties like super plasticity, giant magneto resistance (GMR), transparency in opaque ceramics, enhanced homogeneity, unusual soft ferromagnetic and giant magneto caloric effects, processed by these material where reduced to nanometer dimension. In addition to the understanding of the usual properties possessed by nano phase materials, there are three other associated areas, which need serious attention:

- (i) Identification and development of suitable preparation methods, especially those which are capable of providing large industrial quantities of nanometer scale materials.
- (ii) Development of processing methods for manufacturing these materials into useful size and shapes without losing their desirable nanometer size feature and
- (iii) Identification of proper characterization methods, where the nanometer size range of these materials falls just below or at the resolution limit of the conventional tools.

2.3 Alloy Design Issues

Alloy design issues include issues of chemistry and processing designed to:

- (i) Optimize one of a number of important intrinsic and or extrinsic magnetic properties and
- (ii) Optimize structural or microstructural features which promote important magnetic properties.

The first of these issues concerns the choice of chemistry so as impact the intrinsic magnetization of the material. The second issue pertinent to alloy additions designed at aiding formation of an amorphous phase.

As intrinsic properties we take to mean microstructure insensitive properties including the saturation magnetization, Curie temperature, magnetocrystalline anisotropy and magnetostrictive co-efficient are all important. Also it includes magnetic dipole moment and exchange interaction. Extrinsic magnetic properties important in soft magnetic materials include the magnetic permeability and coercivity, which typically have an inverse relationship. Also include magnetic anisotropy and magnetic coupling through amorphous phases are included to these properties. Magnetic anisotropy and magnetostriction can be considered as extrinsic (microstructure sensitive) in the same for a two phase material (in aggregate) they depend on microstructure.

Since microstructure of alloy in influence extrinsic magnetic properties, the important microstructure features should be recognized including grain size, shape and orientation, defect concentration, compositional in homogeneities, magnetic domain and domain wall. The development of soft magnetic materials for application requires attention to a variety of intrinsic magnetic properties as well as development

extrinsic magnetic properties though an appropriate optimization of the microstructure.

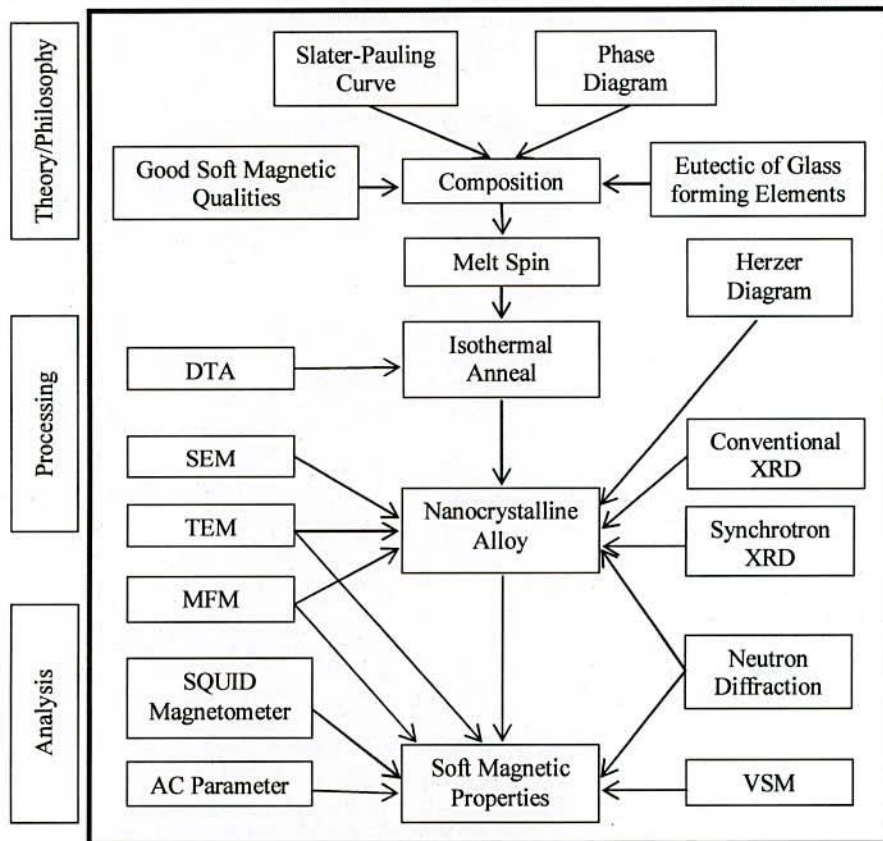


Fig. 2.1 Flowchart for the consideration in designing and developing nanocrystalline soft magnetic material from an amorphous precursor route

Alloy design issues are in many ways influenced by processing routes used to achieve desired microstructures. In Fig. 2.1 illustrates a flowchart for the considerations in designing and developing nanocrystalline soft magnetic material from an amorphous precursor route as an example of the design process. Here we consider first, the effects of alloy composition on intrinsic magnetic properties. This is followed by consideration of alloying additions necessary to produce an appropriate amorphous precursor. Typical experimental steps used to identify the structure and properties of the resulting materials are also illustrated.

2.4 Stages of Evolution of Microstructure

The amorphous alloys in the form of thin ribbons prepared by rapid solidification technique using melt-spinning machine appeared to be the most suitable method available now to synthesize nanocrystalline alloys with attractive soft magnetic properties. The basic principle for the crystallization method from amorphous solids is to control the crystallization kinetics by optimizing the heat treatment conditions such as annealing temperature and time, heating rate, etc. So that the amorphous phase crystallizes completely into a polycrystalline material with ultrafine crystallites nanocrystallization can be realized upon either isothermal or an isothermal annealing in various amorphous metallic alloys in the form of ribbons. Controlled crystallization of FINEMET type of Fe-Cu-Nb-Si-B alloys can be used to obtain partially crystallized materials with nanometer size crystallite embedded in residual amorphous matrix. These special nanocrystal/amorphous composite structures with appropriate compositions allow the material to exhibit extraordinary soft magnetic properties [2.10-2.13].

FINEMET alloys crystallized at temperature above their primary crystallization temperature but below the secondary crystallization temperature can yield nanocrystalline grains with average grain size 10-50nm as a result of primary crystallization of α -Fe(Si) phase embedded in a still remaining amorphous matrix. The excellent soft magnetic properties only occur when the grain size of primary crystallization product of α -Fe (Si) is limited to 10-15nm. This is to note that to obtain an appropriate nanoscale microstructure necessitates very high nucleation rate and very slow growth of the crystalline precipitates simultaneously. It has long been established that when the conventional metallic glasses based on Fe-Si-B are crystallized for the optimization of soft magnetic properties, it has been found that relatively coarse grain microstructure having various crystalline phase have been evolved that dramatically deteriorated the soft magnetic properties.

The nanocrystalline microstructure and the accompanying soft magnetic properties are rather insensitive to the precise annealing conditions within a wide range of annealing temperature $T_a \approx 525-580^\circ\text{C}$. They develop in a relatively short period of time (about 10~15 minutes) and do not much latter even after prolonged heat treatment of several hours [2.12]. A typical heat treatment like $T_a \approx 540^\circ\text{C}$ in most cases yields a nanocrystalline microstructure to the Quasi-equilibrium state and characteristic for the individual alloy composition.

Only annealing at more elevated temperatures above about 600°C leads to the precipitations of small fractions of boride compounds like Fe₂B or Fe₃B with typical dimensions of 50nm to 100nm, while the ultra-fine grain structure bcc Fe-Si still persists. Further increase of the annealing temperature above about 700°C finally yields grain coarsening. Both the formation of Fe borides and grain coarsening deteriorates the soft magnetic properties significantly. The evolution of microstructure during annealing is depicted schematically in Fig. 2.2 and summarized as follows according to Hono *et. al.* [2.14-2.15]. Formation of the nanocrystalline microstructure in the amorphous phase was depicted by G. Herzer in 'the nanocrystalline soft magnetic alloys' [2.16].

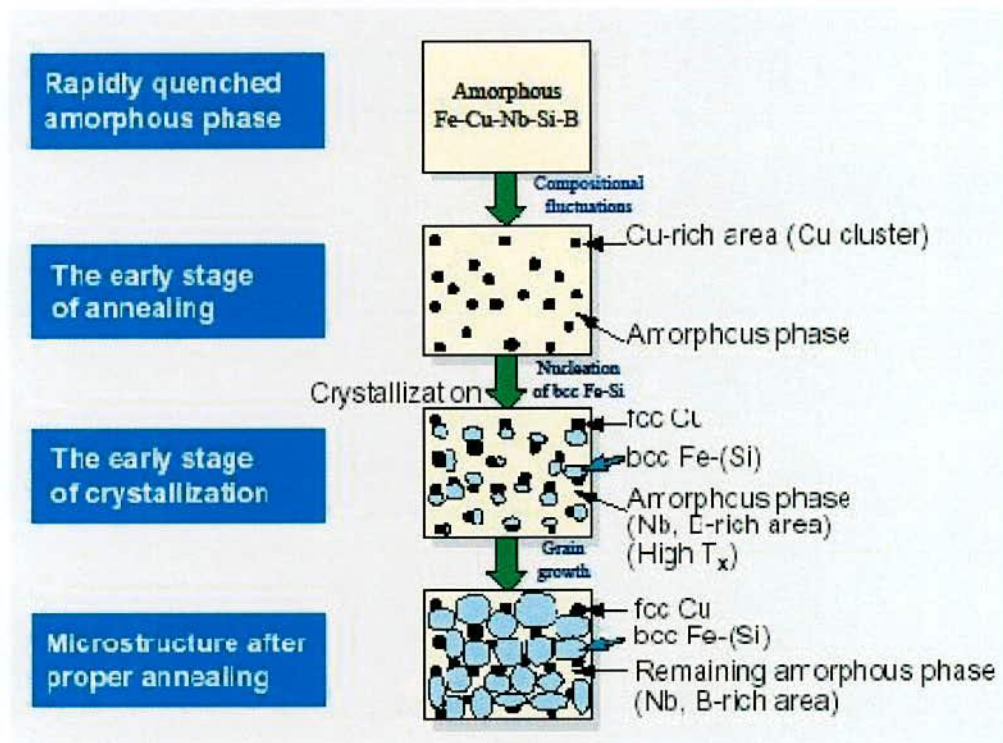


Fig.2.2 Schematic illustration of the formation of nanocrystalline structure

The formation of the particular nanocrystalline structure is essentially related to the combined addition of Cu and Nb (or other group IV or VI elements) and their low solubility in Fe-Si (<0.2 at % Cu, < 0.1 at % Nb). Copper enhances the nucleation of bcc grains while Nb impedes grain coarsening and at the same time, inhibits the

formation of Boride compounds. The microstructure evolution is schematically illustrated in Fig. 2.2 can be summarized as follows.

Annealing at temperatures in general between about 500°C to 600°C leads to primary crystallization of the bcc Fe. At the initial stage of annealing, before the onset of crystallization, the phase separation tendency between Cu and Fe leads to the formation of Cu-rich clusters, with 5nm size and probably still amorphous [2.14-2.15]. Slightly annealing at higher temperature at the initial stage of crystallization α -Fe(Si) phase forms. At this stage Nb and B are excluded from α -Fe(Si) and are enriched in the remaining amorphous phase, because they are insoluble in the α -Fe(Si) phase. This happens when the annealing treatment is carried out at around 550°C when Cu clusters are formed with a few nanometer diameters. Because the investigators [2.17] observed that the Cu clusters and bcc phase simultaneously at the early stage of the nanocrystallization.

Thus the regions between the Cu rich clusters provide a significantly increased density of nucleation sites for the crystallization of bcc Fe. The consequence is an extremely fine nucleation of bcc Fe-Si crystallites at a high rate, which subsequently grow in a diffusion-controlled process as the annealing proceeds further. As annealing goes on the grain size of the α -Fe(Si) increases. At the same time the Si content of this phase keeps increasing since Si tends to be partitioned to the bcc α -Fe(Si) phase. Since the Nb and B enrichment in the amorphous phase stabilizes the remaining state, the grain growth of the bcc phase eventually stops. The presence of Nb at the same time inhibits the formation of Fe-B compounds. The Cu concentration of the clusters also increases as the crystallization proceeds.

At the optimum stage, three distinct phases are present based on the chemical composition. As the bcc Fe-Si phase forms, Nb and B are excluded from the crystallite because of their low solubility in bcc Fe and are enriched in the residual amorphous matrix. At a time all the Si tends effectively to be partitioned into the bcc Fe-Si phase [2.18-2.19]. The particular enrichment with B and Nb increasingly stabilizes the residual amorphous matrix, thus, hinders coarsening of the bcc grains. The presence of Nb at the time inhibits the formation of Fe Boride compounds. The transformation finally ceases in a metastable two-phase microstructure of bcc Fe-Si embedded in an amorphous Fe-Nb-B matrix.

2.5 Advantages of Soft Nanocrystalline Alloys

Nanocrystalline amorphous ribbons are produced by the melt-spinning technique to produce an amorphous metal and then heat treating this alloy at temperature higher than its crystallization temperature. The choice of soft magnetic materials for applications has been guided by recent developments in the field of soft magnetic materials. Amorphous and nanocrystalline magnetic materials, in terms of combined induction and permeability are now competitive with Fe-Si bulk alloys and the Fe-Co alloys. In Fig. 2.3 [2.20], figures of merit for Fe-based amorphous alloys, Co-based amorphous alloys and nanocrystalline alloys are summarized. Co-based amorphous alloys, Fe-based amorphous alloys and nanocrystalline alloys have evolved over the past decades with soft magnetic properties which now exceed those of the bulk alloys based on Fe, Co and Fe-Co.

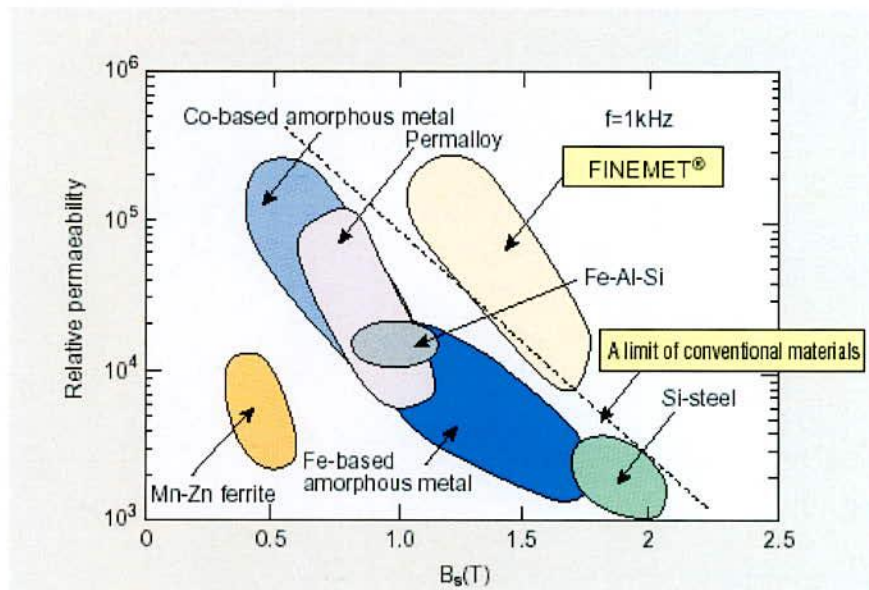


Fig. 2.3 FINEMET is superior compared to conventional materials

This FINEMET material is still in its immaturity since its emergence, although much research work has been carried out for the potential utility of this unique material.

At the stage of development, this material has the following advantages:

- High saturation magnetic flux density more than 1 Tesla or 10kOe.
- High permeability over $\mu_i \approx 10,000$ at 100kHz.
- Excellent temperature characteristics.

- Less affected by mechanical stress.
- Audio noise emission is very low, lower magnetostriction significantly reduces audible noise emission when the voltage and current is applied to the core at audible frequency range.
- Flexible to control the magnetic properties, “B-H curve shape” during the annealing, and three types of B-H curve squareness, high, middle and ion resonance ratio, corresponding to various applications.

2.6 Viscosity Condition for the Formation of Metallic Glass

We find the condition for the formation of metallic glass in the terms of viscosity and diffusion co-efficient are as follows:

- (i) Metallic atomic bonding of the metals; the viscosity is lower than the diffusion co-efficient and mobility is high.
- (ii) Viscosity becomes high and the diffusion co-efficient decreases in the amorphous state. An atomic bond tends to be covalent as in the case of Silicate (SiO_2).

2.7 Conditions for the Formation of Nanocrystalline Alloys

The essential conditions for preparing of nanocrystalline materials are.

- (i) The magnetic properties are highly dependent on the grain size; if the grain size is larger; the magnetic anisotropy would be very high, which in turn will have diverse effect on the soft magnetic properties specially the permeability.
- (ii) For the crystallization process there should be nucleation centers initiated to be distributed throughout the bulk of amorphous matrix.
- (iii) For stabilizing the crystallites there must be a nucleation.
- (iv) Nanocrystalline materials obtained from crystallization must be controlled that crystallites do not grow too big. The grain growth should be controlled so that the grain diameter is within 15-20nm.
- (v) The size of the grain can be limited to nanometer scale by doping group-II metals are

→ Cu (Au)

→ Nb, W, Mo, Cr, Ta etc.

(vi) The stability must be lower and the crystallization must be higher.

There is additional understanding of the unusual properties possessed by nanophase materials; there are three other associated areas, which need serious attention:

- Identification and development of suitable preparation methods, especially which are capable of providing large industrial quantities on nanometer scale.
- For manufacturing of these materials processing methods should be developed useful size and shape without losing their nanometer size feature.
- Identification of proper crystallization methods, where the nanometer size range of these materials falls just below or at the resolution limit of the conventional tools.

2.7.1 Methods used for preparation of Nanocrystalline Alloy

There are various techniques in use to produce a metallic alloy in an amorphous state whose atomic arrangement has no long range periodicity. The methods are generally classified into two groups:

- (i) The atomic deposition method.
- (ii) The fast cooling of the melt.

As we know, controlled crystallization from the amorphous state is the only method which is presently available to synthesize nanocrystalline alloys with superior soft magnetic properties. In this thesis work amorphous ribbons have been prepared by fast cooling of the melt.

2.8.1 The Fast Cooling of the Melt

The molten alloy must be cooled through the temperature range from the melting temperature (T_m) to the glass transition temperature (T_g) very fast, allow no time for crystallization. The factors controlling T_g and crystallization are both structural and kinetic. Atomic arrangement, bonding and atomic size effects are related in the structural factors. The structural factors as discussed by D. Turnbull [2.21] are the nucleation, crystal growth rate and diffusion rate compared to the cooling rate. The pioneering work of P. Duwez, *et al* [2.22], number of devices have

been reported for obtaining the necessary high quenching rates and producing continuous filaments. The methods using the principle of fast cooling of melt techniques are:

- (i) The gun techniques
- (ii) Single roller rapid quenching technique
- (iii) Double roller rapid quenching techniques
- (iv) Centrifuge and rotary splat quencher techniques
- (v) Torsion catapult techniques
- (vi) Plasma-jet spray techniques
- (vii) Filamentary casting techniques
- (viii) Melt extraction techniques
- (ix) Free-jet spinning techniques
- (x) The melt spinning techniques

Although the different methods used in preparing amorphous metallic ribbons are mentioned here, only the single roller rapid quenching technique, which is widely used to prepare the amorphous ribbons.

2.9 Sample Preparation

2.9.1 Master Alloy Preparation

Amorphous ribbons with the nominal composition $\text{Fe}_{73.5-x}\text{Cr}_x\text{Nb}_3\text{Cu}_1\text{Si}_{13.5}\text{B}_9$ [$x = 7, 9, 10 \text{ \& } 12.5$] were prepared in an arc furnace on a water-cooled copper hearth under an atmosphere of pure Ar. Their purity and origin of the constituent elements were Fe (99.9%), Cr (99.9%), Nb (99.9%), Cu (99.9%), Si (99.9%) and B (99.9%) as obtained from Johnson Mathey (Alfa Aesar Inc.). The required amounts of the constituent elements were taken from pure metal bars or flakes, weighed carefully with a sensitive electronic balance and placed on the copper hearth inside the arc furnace. Before melting, the furnace chamber was evacuated (10^{-4} torr), and flashed with Ar gas. The process was repeated several times to get rid of residual air and finally the furnace chamber were kept in an Ar atmosphere.

A substantial amount of pure Titanium getter, placed inside of the chamber on the side of the copper hearth was melted first in order to observe any oxygen present in the furnace chamber. The constituent elements were then melted in the shape of buttons. The arc melting facilities used to prepare the sample are installed at the Centre for Materials Science, National University of Hanoi, Vietnam. The arc furnace used in the preparation of master alloy is shown in Fig. 2.4

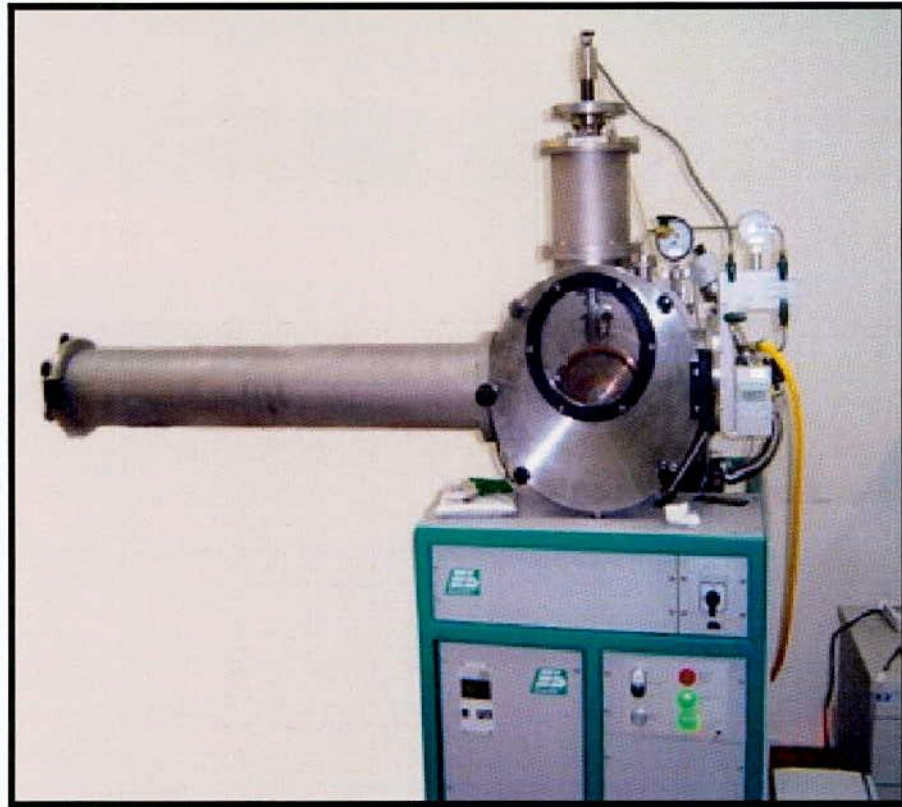


Fig. 2.4 Vacuum Arc Melting Machine

2.9.2 Preparation of Ribbon by Melt Spinning Technique

Melt spinning is a widely used production method for rapidly solidifying materials as well as preparing amorphous metallic ribbon [2.23-2.24]. In order to prepare amorphous of $\text{Fe}_{73.5-x}\text{Cr}_x\text{Nb}_3\text{Cu}_1\text{Si}_{13.5}\text{B}_9$ [$x = 7, 9, 10$ & 12.5] alloys, the melt spinning facilities was used at the Centre for Materials Science, National University of Hanoi, Vietnam. The arc melted master alloy was crashed into small pieces and put inside the quartz tube crucible for re-melting by induction furnace using a medium frequency generator with maximum power of 25kW at a nominal frequency of 10kHz.

Fig. 2.5 shows schematic diagram and Fig. 2.6 shows the pictorial view of the Melt-Spinning Machine. The Quartz crucible has in its bottom part, a rectangular nozzle tip of 8 mm length and 0.7 mm width. The position of the nozzle tip can be adjusted with respect to copper wheel surface, so that the molten alloy was perpendicularly ejected onto the wheel surface from a distance of about 0.3 mm. The small piece of the master alloy samples were inductively remelted inside the quartz tube crucible followed by ejecting the molten metal with over pressure of 250 mbar of 99.9% pure Ar supplied from an external reservoir through a nozzle onto a rotating copper wheel with surface velocity of 30 m/sec. The temperature was monitored by an external pyrometer from the upper surface of the molten alloy through a quartz window.

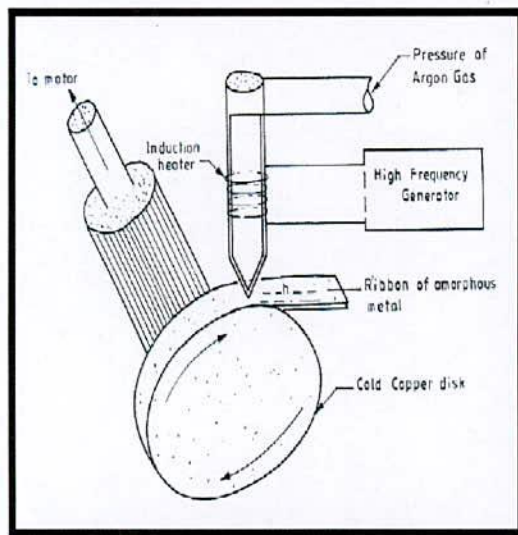


Fig. 2.5 Schematic diagram



Fig. 2.6 Melt-Spinning Machine

The metal alloys were ejected at a temperature of about 150 to 250 K above the melting point of the alloy. The resulting ribbon samples had thickness of about 20-25 μm and width ~ 6 mm. Processing parameters such as the thermal conductivity of the rotating quench wheel, wheel speed, ejection pressure, thermal history of the melt before ejection, distance between nozzle of quartz tube and rotating wheel, as well as processing atmosphere have been influenced on the microstructure and properties of melt-spun ribbons. The lower pressure of 250 mbar as mentioned above stabilizes the turbulence between melt pull and rotating copper wheel enhancing the heat transfer resulting in a more uniform quenching. As a result, a more uniform ribbon microstructure can be obtained at relatively low wheel speed. With increasing wheel speeds for a given ejection rate, the increasing extraction rate results in thinner ribbons.

2.10 Important Factors to Control the Thickness of Ribbons

- (i) Rotating speed
 - Angular velocity $\omega = 2000$ rev/min
 - Surface velocity $V = 20$ m/s to 30 m/s
- (ii) Gap between nozzle and rotating copper drum (h) = 200 to 30 μm
- (iii) Oscillations of the rotating copper drum both static and dynamic has maximum displacement 1.5 to 5 μm
- (iv) Pressure = 0.2 to 3.0 bar at argon atmosphere
- (v) Temperature of molten metals $T_m \approx 1500^\circ\text{C}$; the temperature did not exceed 1800°C otherwise quartz tube would be melted.
- (vi) A steady flow of the molten metals on the surface of the rotating drum needs to be ensured.

2.11 Confirmation of Amorphousness Ribbons

The amorphous state of the four ribbons has been confirmed by X-ray diffraction using BUKER D8 ADVANCE XRD system located at Bangladesh Council of Scientific and Industrial Research (BCSIR).

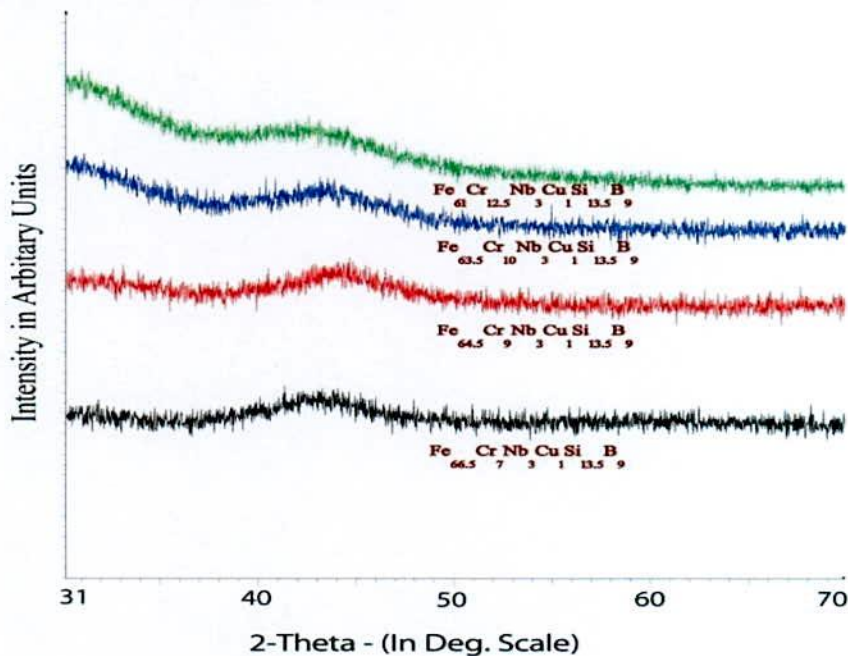


Fig. 2.6 X-ray diffraction of as-cast nanocrystalline amorphous ribbons with Composition $\text{Fe}_{73.5-x}\text{Cr}_x\text{Nb}_3\text{Cu}_1\text{Si}_{13.5}\text{B}_9$ [$x = 7, 9, 10$ & 12.5]

From the X-ray diffraction pattern of the samples in Fig. 2.6, there have been no peaks observed within the scanning range. Although there are few small humps shown in the diffraction pattern around $2\theta = 45^\circ$; but it cannot be regarding due to the crystalline effects. So from all the pattern of X-ray diffraction is confirmed that the samples are in pure amorphous state.

CHAPTER III

THEORETICAL BACKGROUND

THEORETICAL BACKGROUND

3.1 Amorphous Alloys or Metallic Glass

An amorphous (from the Greek *a*, without, *morphe*, shape, form) or non-crystalline solid is a solid that lacks the long-range order characteristics of a crystal. In part of the older literature, the term has been used synonymously with glass. The total structure in amorphous metallic material is distinct from that of window glass. The term amorphous defines a non-crystalline body while a glass refers to a molten mass that is cooled rapidly to prevent crystallization. By analogy, the term 'metallic glass' usually refers to a metallic alloy rapidly quenched in order to freeze its structure from the liquid state. The expression 'glass' in its original sense refers to an amorphous or nanocrystalline solid formed by the continuous cooling of liquid while a solid is defined somewhat arbitrary as object having a viscosity greater than 10^4 Pa.s [3.1]. Glasses have been found in every category of materials and of various bond types, Covalent, ionic, Vender Walls, hydrogen and metallic. Different types of amorphous solids include gel, thin films and nanostructured materials.

3.1.1 Nature and Formation of Amorphous Alloys

From the amorphous state, it is very difficult to get pure metals. It is essential to add glass-forming elements to pure metals or alloys to get the amorphous state and to bring the cooling rate within a reasonable state. Usually around 20% of glass forming materials like B, Si, P, C etc. which have atomic radii comparatively small compared to those of metallic atoms and glass forming atoms occupy the voids left between the bigger atoms of metals when they are closely packed. It can be showed that when there is random close packing of hard spheres, there is about 20% voids created between these atoms. The glass forming materials which have smaller atoms occupy these voids which explain the importance of the glass forming material in the preparation of an amorphous ribbon.

Generally glasses are formed if upon cooling of a melt, crystal nucleation and / or growth avoided. At a temperature called glass transition temperature (T_g) liquid freezes to a rigid solid, however without crystalline order. By the absence of long range transitional order, glasses and amorphous solids are structurally characterized.

But a short-range order is still present and may be similar to that found in the crystalline counterpart.

Synthesizing amorphous alloys requires rapid solidification in order to by-pass the crystallization [3.2]. The metastable structure thus achieved nevertheless may possess short range order (SRO) that resembles the equilibrium crystal structure [3.3]. This indicates that the thermodynamic forces that drive crystallization in metals are extremely strong and in the more case overpowering. Thus the search for alloy systems that allow formation of amorphous structures is of keen technological importance.

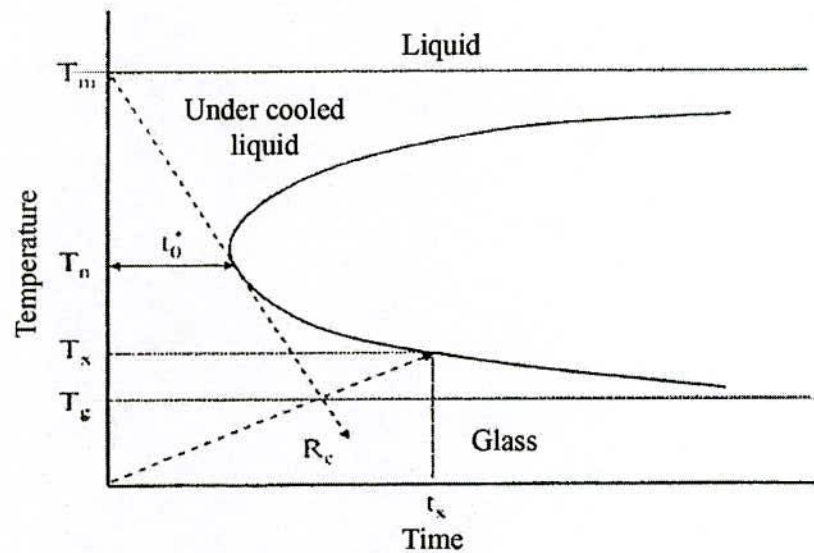


Fig. 3.1 Schematic TTT diagram for the onset of crystallization

The time taken for a small amount of crystalline phase to form in an under cooled liquid as a function of temperature shown in Fig. 3.1 schematically. The Temperature-Time-Transformation (TTT) diagram shows a characteristic C curve behavior. At the temperature close to melting point T_m , there is little driving force for crystallization, so that the crystal nucleation and growth rates are small, and crystallization onset time t_0 is large. As the temperature decreases, the crystallization onset time reaches a minimum value t_0^* at a temperature T_n , and then increases again as the thermal energy becomes insufficient for atomic motion.

The atomic motion is completely suppressed and the amorphous structure is frozen in close to the T_g . So that the crystallization onset time t_0 becomes large. Therefore, to avoid crystallization, critical cooling rate R_c is given

$$R_c = \frac{T_m - T_n}{t_0} \quad (3.1)$$

The absence of long range order (LRO) easily to determine using XRD. For example in XRD, broad diffuse halo peaks are observed with $2\theta \approx 10^\circ$ broadness with Cu-K α radiation instead of the sharp Bragg peaks shown by crystalline state.

3.1.2 Factor Contributing to Glass Formation and Stability

There are three inter related factors that determine glass-forming tendency. These are:

- (i) Thermodynamic conditions that favor the liquid phase relative to the crystalline phase.
- (ii) The kinetic conditions that inhibit crystallization and
- (iii) The processing factors that arise due to experiential conditions.

The thermodynamic factors for glass formation are liquids temperature (T_m) at which the alloy melts, the heat of vaporization and the free energy of all the phases that arise or could potentially arise during solidification process. Viscosity of the melt, the T_g and the homogeneous nucleation rate belongs to kinetic parameters. The glass transition temperature is defined as the temperature at which the super cooled liquid takes on the rigidity of a solid or more specifically at which the viscosity approaches 15 Poise.

One of the following two events may occur when a liquid is cooled, either crystallization may take place at the T_m or the liquid will become super-cooled below T_m . If the liquid is super cooled sufficiently, its density gradually falls and its viscosity gradually rises. Thus microscopic flow of the liquid becomes progressively more difficult. These changes can be observed by monitoring the volume of the super cooled liquid as a function of temperature and a typical result is shown in Fig. 3.2 [3.4].

The crystallization process is manifested by an abrupt change in volume at T_m , where glass formation is characterized by a gradual break in slope. The region over which the change of slope occurs is termed the T_g .

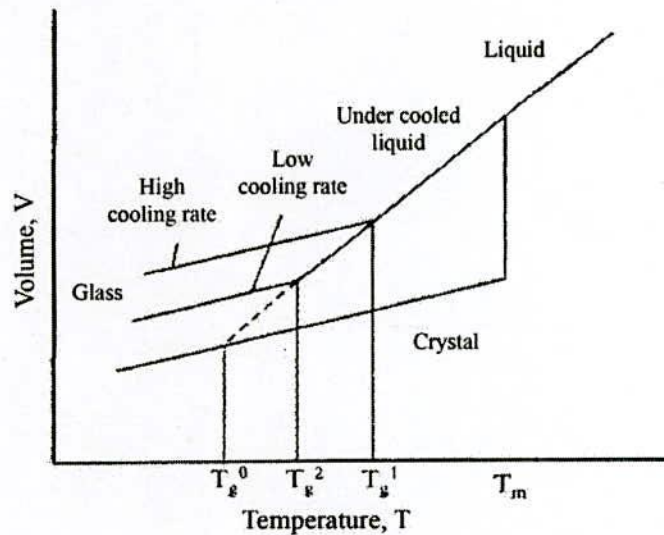


Fig. 3.2 Volume-Temperature relationship in solid, liquid and glass state

The point at which the alloy finally solidifies with frozen in amorphous atomic structure is the T_g . Freezing the amorphous structure at the T_g is a kinetic rather than a thermodynamic transition. The cooling rate decreases gives more time for atomic motion, allowing the liquid to maintain its equilibrium structure to lower the T_g , with a denser, lower entropy structure. The T_g is not a constant of the material but is a function of experimental conditions. The volume (ΔV) and entropy (ΔS) difference between the liquid and the crystal decreases the temperature progressively as the temperature falls, and approaches zero at a temperature called the ideal glass transition temperature (T_g^0).

An amorphous structure with higher density and lower entropy than the corresponding crystal is impossible [3.5]. So T_g^0 is the natural limit of the range of possible T_g , corresponding to a condition of an infinitely slow cooling rate. In general, T_g is defined as the temperature at which an amorphous solid such as glass or a polymer, becomes brittle on cooling, or soft on heating. More specifically it defines a pseudo second order phase transition in which a super-cooled melt yields, on cooling, a glassy structure and properties similar, those of crystalline materials e.g. of

an isotropic solid material [3.6]. Now we can measure the glass transition temperature by using Differential Thermal Analysis (DTA).

3.2 Structure and Microstructure of Amorphous and Nanocrystalline Alloys

An amorphous solid is one in which the atomic positions do not have crystalline periodic order. The amorphous structure is postulated to be that of the frozen liquid. The local structure in amorphous metallic materials is distinct from that of window glass. A periodically spaced atom does not exist in amorphous alloys. Therefore XRD does not show any diffraction patterns. If X-Ray scattering experiment perform on amorphous material, thus observe one or more peaks in the scattered intensity shown in Fig. 3.3 at angles, similar to those where one or more diffraction peaks would occur in a crystalline alloy of the same composition.

From Scherer analysis of the breadth of X-Ray scattering peak (s), one would conclude that the 'crystalline Size' was on the order of atomic dimensions. For the sort range atomic correlations only being present in amorphous metals is a good argument. Scattering experiment on amorphous alloys can be used to determine the so called radial distribution function that is derived from an appropriate Fourier transform of a normalized scattered intensity expressed as a function of scattering angle. The atoms in an amorphous solid are not periodically arranged and therefore the concept of a lattice is not appropriate for describing their positions. Thus in an amorphous solid there is not an equivalent concept to that of a lattice and a basis of region to describe atomic positions in a more probabilistic sense using the concept of a pair correlation function $g(r)$. The pair correlation function $g(r)$ is defined as the probability that two atoms in the structure are separated by the distance r . To define $g(r)$ further begin by considering N atoms in a volume Ω , letting $R_1, R_2, R_3, \dots, R_N$ denote the position of the N atoms with respect to an arbitrary origin. The distance r denotes the magnitude of the vector connecting two atoms i and j ,

$$\text{i.e., } r = R_i - R_j \quad (3.2)$$

Two additional atomic distribution functions related to the pair correlation function are the spatially dependent atomic density $\rho(r)$, which is defined as;

$$\rho(r) = \frac{Ng(r)}{\Omega} \quad (3.3)$$

and the radial distribution function RDF(r), which is defined in terms of the pair correlation function as;

$$\text{RDF}(r) = 4\pi^2\rho(r) \quad (3.4)$$

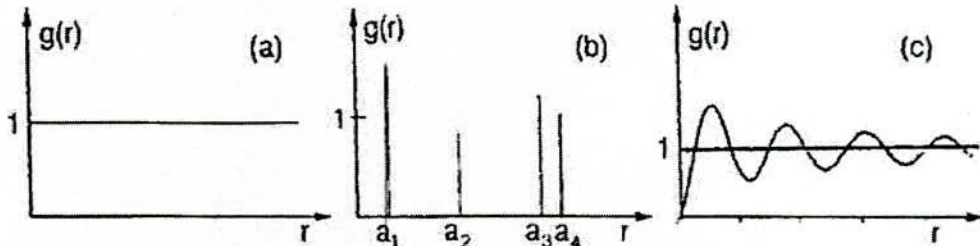


Fig. 3.3 typical pair correlation function for (a) a completely disordered, (b) a crystalline completely ordered and (c) an amorphous short range ordered material

Fig. 3.3 illustrates schematically the distinction between pair correlation function for completely disordered, a crystalline completely ordered and an amorphous short range ordered material. A completely disordered material like a gas has a uniform unit probability of finding neighboring atoms at all possible distances which leads to a uniform, featureless $g(r)$. On the other hand, a crystalline solid has a set of discrete distances between atomic positions and therefore the pair correlation function in a set of discrete δ – like functions, the amplitude which reflects the particular coordination number for nearest neighbor, next nearest neighbor, ... etc. pair of atoms. This is consistent with Bragg diffraction scattering. In amorphous alloys $g(r)$ is neither discrete nor featureless; instead broad peaks reflect the short range order in these materials.

3.3 Stability of the Amorphous and Nanocrystalline Materials

Amorphous materials are always metastable state which leads to transform into more stable crystalline phase. There are three kinds of stability of significance for magnetic ribbons;

- (i) Their resistance to the initiation of crystallization.
- (ii) Structural relaxation effect, and

(iii) The relaxation or reorientation of directional order.

Controlled crystallization seems from the amorphous state to be the only method presently available to synthesize nanocrystalline alloys with attractive soft magnetic properties. The formation and the resultant stability of amorphous alloys are important topic, both for theoretical understanding and technical. The theoretical analyses of the factors controlling the case of formation and the stability of the resultant amorphous alloys have been extensively reviewed [3.7-3.8]. From the thermodynamic view point [3.9-3.10], the ability of an alloy to be quenched into the glassy state is generally measured by the magnitude of the quantity.

$$\Delta T_g = T_m - T_g \quad (3.5)$$

Where T_m and T_g are the melting and glass temperature respectively. The stability of the glass after formation in a similar manner is generally measured by the magnitude of the quantity.

$$\Delta T_x = T_x - T_g \quad (3.6)$$

Where T_x is the temperature for the onset of crystallization. As the temperature decrease from T_m , the rate of crystallization will increase rapidly but then fall rapidly as the temperature decrease below T_g . So that if we quenched a molten alloy rapidly enough to temperature below T_g a quasi-equilibrium amorphous phase is obtained. There is no direct relation between the easy of formation and the resultant stability of an amorphous alloy. The amorphous alloy composition most favorable for glass formation is near eutectic i.e. the composition in which the transformation from the liquid state to solid state takes place instantaneously without passing through liquid plus solid mixed phase. The deeper the eutectic the better is the glass formation ability [3.11]. There have been three approaches for relating the stability of the glass, i.e. its microstructure:

- (i) Barnal's model of randomly packed hard sphere's [3.12]. The atoms of the metal are assumed to form a random network of close packed hard spheres and the smaller metalloid atoms fill the holes inherent in such structure.

- (ii) The effect of atomic sizes and inter atomic interactions [3.13], i.e. chemical bonding suggested that it is chemical bonds which are dominating factors in glass formation and stability.
- (iii) The third approach [3.14] is based on the role of the electron gas and showed that under certain circumstances a nearly free electron gas will produce a barrier against crystallization.

The transition to the glassy state and the crystalline state is accompanied by an exothermic heat effect giving rise to a sharp peak in temperature dependence of the heat flows. Therefore, DTA is a widely used technique to study thermally induced transformations in amorphous alloys and to determine T_g and T_x . The magnitude of T_g and T_x are very different for amorphous materials and depend strongly on composition. The activation energy ranges typically between 2 and 6 eV [3.15].

3.3.1 Characteristics of the Glass Transition Temperature

When the time scale of molecular rearrangements occurs glass transition temperatures (T_g) are too long for equilibrium to be maintained:

- (i) T_g means the time scale of the experiment matters.
- (ii) A high frequency/short time scale experiment allows less long for equilibrium to be established – even for an identical cooling rate.
- (iii) NMR (high frequency technique 10^{15} Hz.) always measures a higher T_g than DTA (1 Hz.).
- (iv) In the glass itself, entropy is similar to the crystal and original in vibrational modes, which are still present.
- (v) Long range transitional motions are frozen out. The temperature T_g configuration relaxation (including translational motion) but vibrational relaxations are still in equilibrium.
- (vi) T_g decreases as melt cooled more and more slowly.
- (vii) When the time scale of the experiment and the configuration relaxation time coincide, begin to see departure from equilibrium.
- (viii) The time scale for configuration relaxation will be related to rotational or translational diffusion coefficient.

- (ix) Optional definition of T_g is when the viscosity of the super-cooled liquid exceeds 10^{13} NSm⁻². Where as in the liquid there is an Arrhenius type with a Boltzmann factor containing activation energy.

3.4 Differential Thermal Analysis and its Application

Differential thermal Analysis (DTA) is an important technique for the study of structural change both in solid and liquid materials under heat treatment. During this process, the temperature difference between a substance and reference material is measured as a function of temperature whilst the subject and the reference material are subjected to some controlled temperature program. The transition of an amorphous or glassy state to crystalline state is accompanied by an exothermic heat effect that gives rise to a sharp peak in temperature dependence of the heat flow. To study this thermally induced transformation in amorphous alloys, DTA is a widely used technique. Amorphous alloys are in a metastable state and tend to transition into stable crystalline phases. At temperature below the crystallization temperature, structural relaxation effect takes place which are caused by atomic rearrangements. DTA is an important technique for the study of structural change both in solid and liquid materials under heat treatment. The principle of DTA is widely used to understand the crystallization nature of the amorphous. Differential thermal analysis is a direct and effective technique for analyzing the kinetics of amorphous materials and stability with respect to crystallization process.

The crystallization is associated with the nucleation and growth process. Since the formation of an amorphous alloy depends on the absence of LRO, change of composition is expected to affect T_g and T_x . This is because long range ordering of atoms depends on the free energy difference between the crystalline state and the amorphous state. The magnitude of T_g and T_x are very different for amorphous materials and depend strongly on composition. Using DTA technique it is possible to determine T_g and T_x . Nanocrystalline amorphous ribbons prepared by rapid quenching method have been subjected to DTA using a Shima dzu Thermal Analyzer. Different peaks, crystallization temperatures, crystallization activation energies are obtained from this analysis.

3.4.1 Evaluation of Activation Energy Based on DTA Technique

Based on the work of Murray and White [3.16-3.18], the kinetics of materials can be understood by interpretation of DTA patterns of the materials. The dependence of T_x on the heating rate $\beta = \frac{dT}{dt}$ can be used to determine the activation energy of crystallization [3.19]. Considering the fraction x of amorphous material transformed into the crystalline state in time t and at temperature T obtains for the first-order rate process [3.20-3.21]

$$\left(\frac{\delta x}{\delta t}\right)_T = K(1-x) \quad (3.7)$$

For thermally activated process, the rate constant K obeys an Arrhenius type of equations

$$K = K_o e^{-\left(\frac{\Delta E}{RT}\right)} \quad (3.8)$$

where K_o is a constant and ΔE is the activation energy. Combining eqⁿ. (3.7) and (3.8)

and using $dx = \left(\frac{\delta x}{\delta t}\right)_T dt + \left(\frac{\delta x}{\delta t}\right)_t dT$ with $\left(\frac{\delta x}{\delta t}\right)_t dt \cong 0$, are obtained

$$\frac{dx}{dt} = K_o(1-x)e^{-\left(\frac{\Delta E}{RT}\right)} \quad (3.9)$$

$$\frac{d^2x}{dt^2} = \frac{d}{dt} \left[K_o(1-x)e^{-\left(\frac{\Delta E}{RT}\right)} \right]$$

$$= -K_o \frac{dx}{dt} e^{-\left(\frac{\Delta E}{RT}\right)} + K_o(1-x) \frac{d}{dT} \left\{ e^{-\left(\frac{\Delta E}{RT}\right)} \right\} \frac{dT}{dt}$$

$$= -K_o \frac{dx}{dt} e^{-\left(\frac{\Delta E}{RT}\right)} + \frac{dx}{dt} \left(\frac{\Delta E}{RT^2} \right) \beta$$

At the peak of the exothermic heat, the change of the reaction rate $\frac{d^2x}{dt^2} = 0$, yielding

with $T = T_x$ but $\frac{dx}{dt} \neq 0$

$$K_o e^{-\left(\frac{\Delta E}{RT_x}\right)} = \left(\frac{\Delta E}{RT_x^2} \right) \beta \quad (3.10)$$

From eqⁿ (3.10) it is easily seen that

$$\frac{d\left(\ln \frac{\beta}{T_x^2}\right)}{d\left(\frac{1}{T_x}\right)} = -\frac{\Delta E}{R} \quad (3.11)$$

Here $\beta = \frac{dT}{dt}$ the heating rate. ΔT_x for the stability of amorphous alloys as given by eqⁿ (3.6) and is obtained from DTA. Similar correlation between thermal stability as measured by ΔT_x and ΔE appears too small.

From the measured data of the heating rate (β) and the respective crystallization temperature (ΔT_x), the activation energy can be deduced from the slope of a plot $\ln \frac{\beta}{T_x^2}$ versus $\frac{1}{T_x}$ from eqⁿ (3.11) can be derived from the transformation theory, where ΔE is the activation energy for versus flows and other terms have been omitted because they insignificant temperature dependence in this region of temperature. The values of ΔE also appear to correlate well with the number of atomic species in the alloy; the more complex the alloy the grater is ΔE .

3.5 Determination of Nanometric Grain Size by X-Ray Diffraction

Nanocrystalline alloys are basically crystalline and because of their crystallinity and they exhibit Bragg scattering peaks in X-ray diffraction experiments. However, due to their small size, significant fine particle broadening is observed in the Bragg peaks. The X-ray scattering from a crystalline solid is given by Bragg's law:

$$2d \sin \theta = n\lambda \quad (3.12)$$

This equates the path difference scattered from parallel crystalline planes spaced $d = d_{hkl}$ apart to an integral number (n) of X-Ray wavelength λ . Here θ is the X-Ray angle of incidence (and of diffraction) measured with respect to the crystalline planes. Bragg scattering occurs at discrete values of 2θ satisfying the Bragg condition for an infinite crystal, i.e. Bragg peaks are δ -functions. The peaks are broadened over a range of angles for finite sized crystals as shown in Fig. 3.4.

To understand the phenomenon of fine particle broadening following argument of Cullity [3.22] is outlined below. We consider a finite crystal of thickness, $D_g = md$, where m is an integer and d is the distance between crystalline planes, i.e., there are m planes in D_g . considering Fig. 3.4, if the broadened Bragg peak begins at an angle $2\theta_2$ and ends at $2\theta_1$, the breadth of the peak or full width at half maximum is given as:

$$\beta = \frac{1}{2}(2\theta_1 - 2\theta_2) = \theta_1 - \theta_2 \quad (3.13)$$

Now consider the path differences for each of the two angles θ_1 and θ_2 , for X-rays travelling the full thickness of the crystal. The width β is usually measured in radians; intensity is equal to half the maximum intensity. As a rough measure of β , we can take half the difference between the two extreme angles at which the intensity is zero, which amounts to assuming that the diffraction line is triangular in shape.

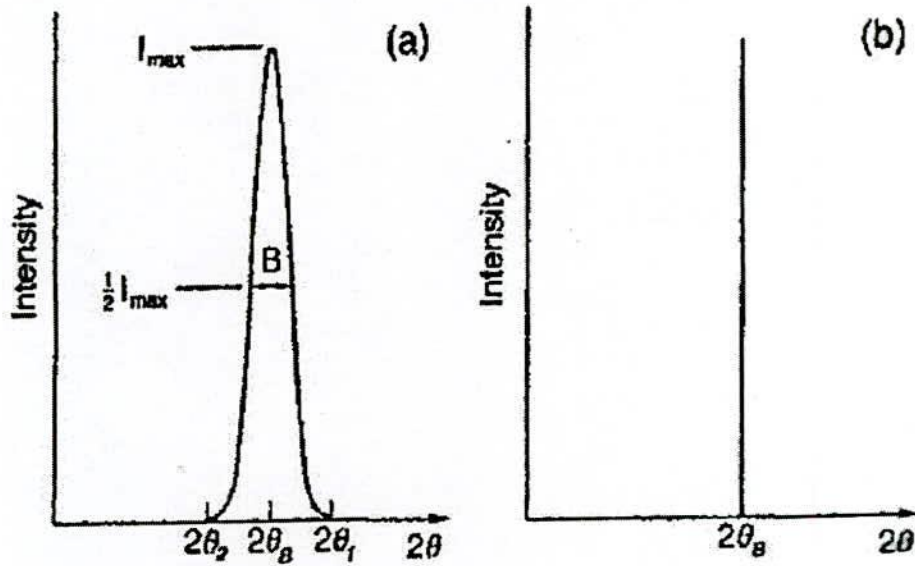


Fig. 3.4 Effect of fine particle broadening in XRD (a) fine particle and (b) perfect crystal

We now write the path difference equations for those two angles related to the entire thickness of the crystal rather than the distance between adjacent planes.

$$2D_g \sin \theta_1 = (m + 1)\lambda \quad (3.14)$$

$$2D_g \sin \theta_2 = (m - 1)\lambda \quad (3.15)$$

By the subtraction;

$$D_g (\sin \theta_1 - \sin \theta_2) = \lambda \quad (3.16)$$

$$2D_g \cos\left(\frac{\theta_1 + \theta_2}{2}\right) \sin\left(\frac{\theta_1 - \theta_2}{2}\right) = \lambda \quad (3.17)$$

But θ_1 and θ_2 are both very nearly equal to θ , so that $\theta_1 + \theta_2 \approx 2\theta$ and $\sin\left(\frac{\theta_1 - \theta_2}{2}\right) \approx \left(\frac{\theta_1 - \theta_2}{2}\right)$ thus the eqⁿ (3.17) can be written as:

$$2D_g \cos\theta \cdot \left(\frac{\theta_1 - \theta_2}{2}\right) = \lambda \quad (3.18)$$

From the eqⁿ (3.13) and eqⁿ (3.18) we get:

$$\beta \cdot D_g \cos\theta = \lambda \quad (3.19)$$

$$D_g = \frac{\lambda}{\beta \cos\theta} \quad (3.20)$$

A more exact empirical treatment yields:

$$D_g = \frac{0.9\lambda}{\beta \cos\theta} \quad (3.21)$$

This is known as the Scherrer's formula. It is used to estimate the particle size of very small crystals from the measured width of their diffraction curves.

3.5.1 Random Anisotropy Model (RAM)

Random Anisotropy Model (RAM) is proposed by Herzer [3.23] for the soft magnetic properties based on FINEMET type of nanocrystalline alloys. Soft magnetic properties of nanocrystalline alloys are strongly dependent on the grain size and grain boundary structure. In order to interpret the behavior of the magnetic properties for atomic scale grains, the RAM was originally proposed by Alben *et al.* [3.24] for amorphous ferromagnets. The basic idea is sketched in Fig. 3.5 and starts from an assembly of ferromagnetically coupled grains of size D_g with magneto crystalline anisotropies K_1 oriented at random.

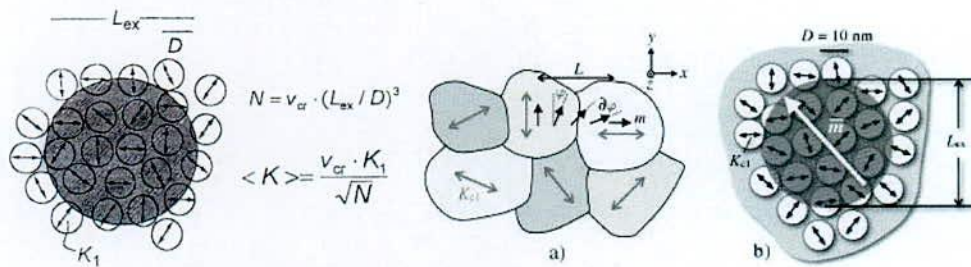


Fig. 3.5 Schematic representation of Random Anisotropy Model (RAM) (a) Assembly of grains, each of them is having a randomly fluctuating anisotropy axis (b) The correlation volume of size L_{ex} in nanocrystalline material consisting of grains

The concept of a magnetic exchange length (L_{ex}) and its relationship to the domain wall width (δ_w) and nano domain size is important in the consideration of magnetic anisotropy in nanocrystalline soft magnetic materials [3.24]. These can be defined by applying to a Helmholtz free energy function as described by Coey [3.25]. These length scales are:

$$\delta_w = \pi \sqrt{\frac{A}{K_1}} \text{ And } L_{ex} = \sqrt{\frac{A}{4\pi M_s^2}} \quad (3.22)$$

Herzer considers a characteristic volume whose linear dimension is the magnetic exchange length $L_{ex} \sim \left(\frac{A}{K_1}\right)^{\frac{1}{2}}$, where K_1 is the nanocrystalline anisotropy. The unstated constant of proportionality should be $\left(\frac{k}{\pi}\right)$ which for materials with very small K_1 can in fact be quite large. Ignoring this constant of proportionality, the Herzer's argument considers N grains, with random easy axes, within a volume of L_{ex}^3 to be exchange coupled. Since the easy axes are randomly oriented, a random walk all over N grains will yield an effective anisotropy which is reduced by a factor of $\left(\frac{1}{N}\right)^{\frac{1}{2}}$ from the value K_1 for any one grain, thus $K_{eff} \approx \frac{K_1}{\sqrt{N}}$. Now the number of grains in this exchange coupled volume is just $N \approx \left(\frac{L_{ex}}{D_g}\right)^3$, where D_g is the average diameter of individual grains. The ferromagnetic correlation volume $V = L_{ex}^3$ is determined by the exchange length L_{ex} . The results from averaging over the $N = V_{cr} \left(\frac{L_{ex}}{D_g}\right)^3$ grains, volume fraction V_{cr} relevant to the magnetization process with magnetocrystalline anisotropy oriented at random. Treating the anisotropy self-consistently, then

$$K_{eff} = V_{cr} \frac{K_1}{\sqrt{N}} = V_{cr}^{\frac{1}{2}} K_1 \left(\frac{D_g}{L_{ex}}\right)^{\frac{3}{2}} \quad (3.23)$$

The ferromagnetic exchange length $L_o = \sqrt{\frac{A}{K_1}}$, the exchange length L_{ex} has to be normalized by substituting $4\pi M_s^2 = K_{eff}$ in eqⁿ (3.22) i.e. L_{ex} is self-consistently related to the average anisotropy by

$$L_{ex} = \left(\frac{A}{K_{eff}}\right)^{\frac{1}{2}} \quad (3.24)$$

Combining eqⁿ (3.23) and eqⁿ (3.24), we get

$$K_{eff} = \sqrt{V_{cr}} K_1 \left[\frac{D_g}{\sqrt{\frac{A}{K_{eff}}}} \right]^{1/2}$$

or $K_{eff} = \sqrt{V_{cr}} K_1 \left[\frac{D_g \sqrt{K_{eff}}}{\sqrt{A}} \right]^{3/2}$

or $K_{eff} = \sqrt{V_{cr}} K_1 \left[\frac{D_g \sqrt{K_{eff}}}{L_0 \sqrt{K_1}} \right]^{3/2}$

or $K_{eff}^4 = V_{cr}^2 K_1^4 \frac{D_g^6 (\sqrt{K_{eff}})^6}{L_0^6 (\sqrt{K_1})^6}$

or $K_{eff}^4 = V_{cr}^2 K_1^4 \frac{D_g^6 \sqrt{K_{eff}}^3}{L_0^6 K_1^3}$

or $K_{eff} = V_{cr}^2 K_1 \left(\frac{D_g}{L_0} \right)^6$

or $K_{eff} = V_{cr}^2 K_1 \frac{D_g^6}{\left(\frac{A}{\sqrt{K_1}} \right)^6}$

or $K_{eff} = V_{cr}^2 K_1 \frac{D_g^6}{A^3} K_1^3$

or $K_{eff} = V_{cr}^2 D_g^6 \frac{K_1^4}{A^3}$

or $K_{eff} = \frac{V_{cr}^2 D_g^6 K_1^4}{A^3} \quad (3.25)$

Since the coercivity can be taken as proportional to the effective anisotropy. This analysis leads to Herzer's prediction that the effective anisotropy and therefore the coercivity should grow as the 6th power of the grain size:

$$H_c \sim D_g^6 \quad (3.26)$$

Herzer noted that the Nanocrystalline grains must be exchange coupled for such a reduction in the coercivity to be realized. This to be contrasted with uncoupled particles that have an exchange length, comparable to the particle diameter is susceptible to super paramagnetic response.

The most significant feature predicted by the RAM is the strong variation K_{eff} with the 6th power of the grain size. Thus for $D_g \approx \frac{L_0}{3}$. i.e. grain sizes in the order of

10-15 nm, the magnetocrystalline anisotropy is reduced by three order of magnitude towards a few J/m^3 , i.e. small enough to enable superior soft magnetic behavior.

The K_{eff} , essentially determines the magnetic softness, since H_c and inverse of initial permeability (μ) are proportional to K_{eff} . Therefore it is expected that these quantities have similar dependence on grain size and have been confirmed experimentally [3.27]. Herzer explained the size dependence of the H_c based on RAM considering the nanocrystalline materials as single phase magnetic system. Hernando *et. al.* [3.28] extended this model for two phase materials and was able to explain the thermal dependence of the coercivity [3.29-3.30]. Hernando has generalized RAM, taking into account the two phase character of nanocrystalline materials and it explained the previously maintained hardening as well as other features which could not be understood without the generalization. Since the dimensions of the crystallites dictate the unique properties by controlling the annealing temperature of the specimens. The magnetic softness or hardness in respect of permeability is determined by the grain size, grain distribution and the volume fraction, which are developed on the amorphous matrix in the nanostructure system.

3.6 Magnetic Dipole Moments and Magnetization

Fe, Co or Ni, or the rare earth metal Gd as a majority component. The vast majority of soft magnetic materials have one or more of the ferromagnetic transition metal element. The magnetic dipole moments of the elemental and alloy magnets are almost completely understood through the Band Theory of Solids [3.31]. The band theory of solids considers the broadening of localized atomic states with discrete Eigen values into a continuum of states for more itinerant electrons over arranged of energies. The theory allows for calculation of energy dispersion (i.e. energy as a function of wave vector) and orbital angular momentum specific and spin-resolved densities of states. The calculation of spin-resolved energy band and densities of states allows for the dispersion of atom resolved magnetic dipole moments, therefore spontaneous magnetization of element and alloy magnetic solids. Among the success of the band theory descriptions of magnetic properties are:

- (i) The prediction of non-integral or half integral atomic dipole moments and resulting ground state magnetization in the metals and alloys.

- (ii) The prediction that band widths and exchange splitting (energy differences between spin up and spin down bands) are intimately dependent on magnetic coordination number and atomic volume.

The variation of the mean atomic magnetic dipole moment as a function of composition in the transition metal alloys system. Spin resolved densities of states $g_+(E)$ and $g_-(E)$ for Co and Fe atoms, in an equiatomic Fe Co alloy, as a function of energy (where the Fermi energy, E_F is taken as the Zero of energy). The number of spin up, n_+ and spin down, n_- electrons in each band can be calculated again by integrating these densities of state:

$$n_+ = \int_0^{E_F^+} g_+(E) dE \quad (3.27)$$

$$\text{and } n_- = \int_0^{E_F^-} g_-(E) dE \quad (3.28)$$

Here the Fermi energies, E_F , are the same and the zero's of energy are different for the two spin bands and the atom resolved (i.e. Fe and Co) magnetic dipole moments can be calculated as:

$$\mu_m = (n_+ - n_-)\mu_B \quad (3.29)$$

Knowledge of atomic values or alloy density, then allows for the direct calculation of the alloy magnetization. The Fe-Co alloy, exhibits the largest magnetic inductions of any material and also have T_c 's which are desirable for high temperature applications. Fe rich alloys typically have smaller inductions and lower Curie temperatures than Fe-Co alloys. Co alloys can also be soft but only if the fcc phase of Co is present. Co rich alloys typically have smaller inductions and larger T_c 's.

Table 3.1, summarizes the absolute zero and room temperature (where applicable) magnetizations and atomic dipole moments for some important transition metal and rare earth elemental magnets. Also shown Curie temperatures i.e. ferromagnetic ordering temperatures which are not ground state properties that directly calculable from the band theory [3.32].

Table 3.1 Spontaneous and room temperature magnetizations, magnetic dipole moments and Curie temperature for elemental ferromagnets

Element	$\mu_m@0K(\mu_B)$	$M_s@0K$ (G)	$M_s@RT$ (G)	$T_c(K)$
Fe	2.22	1740	1707	1043
Co	1.72	1446	1400	1388
Ni	0.606	510	485	627
Gd	7.63	2060	--	292
Dy	10.2	2920	--	88

3.6.1 Magnetization of the Nanocrystalline Ribbon

The saturation magnetization of a material at a temperature of 0 K is one of its basic properties. Measurements are usually expressed as average moment per magnetic atom in units of the Bohr magneton, μ_b as specific saturation magnetization for the amorphous alloy, σ_s in units for Am^2/kg . The moments of most amorphous alloys are lower than those of the structural disorder on the moments is very small. This is point out the importance of chemical instead of structural disorder. The reduction is least in B-based and highest in p-based glass. The observed moments on TM-M glasses can approximately fit to the formula [3.33].

$$\mu = \left(\frac{\mu_{TM} C_{TM} - C_B - 2C_{sc} - 3C_p}{C_{TM}} \right) \quad (3.30)$$

Where μ_{TM} is the magnetic moment of TM-M atoms, taken as 2.6, 1.6 and 0.6 respectively in Bohr magneton for Fe, Co and Ni, C's are respective concentrations. This clearly demonstrates the charge transfer from metalloid to d-band of transition metal and seems to suggest that 1, 2 or 3 electrons are transferred from each of B, Si (C, Ge) or P atom. The relative number of electrons donated can be listed as $-P_{13}C_7 > -S_{15}B_{10} > -P_{16}B_6Al_3 > -P_{14}B_{13} > -B_{20}$ Based on the relative magnitudes of M_s .

3.6.2 Ferromagnetic ordering (Curie) Temperatures

Ferromagnetism is a collective phenomenon since individual atomic moments interact so as to promote alignment with one another. This collective interaction gives rise to the temperature dependence of the magnetization. Two models have explained

the interaction between atomic moments. Mean Field Theory considers the existence of a non-local internal magnetic field, called the Weiss field, which acts to align magnetic dipole moments even in the absence of an applied field H_a . Heisenberg Exchange Theory considers a local (usually nearest neighbor) interaction between atomic moments (spins) which acts to align adjacent moments even in the absence of a field.

The basic assumption of the mean field theory is that this internal field is non-local and is directly proportional to the sample magnetization.

$$H_{INT} = \lambda_w M \quad (3.31)$$

where the constant of proportionality, λ_w , is called the Weiss molecular field constant.

To consider ferromagnetic response in applied field, H_a , as well as the randomizing effects of temperature, we consider the superposition of the applied and internal magnetic fields. By analogy with the problem of paramagnetic moments, the average atomic dipole moment can be expressed in terms of the Brillouin function

$$\langle \mu_m \rangle = \mu_m^{atom} B_J(\alpha') \quad (3.32)$$

where $\alpha' = \left(\frac{\mu_0 \mu_m^{atom}}{K_B T} \right) (H + \lambda_w M)$ for a collection of classical dipole moments. The saturation magnetization

$$M_s = N_m \langle \mu_m^{atom} \rangle \quad (3.33)$$

$$\frac{M}{N_m \mu_m^{atom}} = \frac{M}{M_s} = B_J[H + \lambda_w M] \quad (3.34)$$

Under appropriate conditions, this leads to solutions for which there is a non-zero magnetization (spontaneous magnetization) even in the absence of an applied field.

For $T > T_c$, the ferromagnetic T_c the only solution to eqⁿ (3.34) is $M = 0$, i.e., no spontaneous magnetization and thus paramagnetic response. For $T < T_c$, we obtain solutions with a non-zero, spontaneous magnetization, the defining feature of a ferromagnet.

Ferromagnetic exchange interactions set the scale for T_c in ferromagnetic alloys. Inter atomic exchange couplings can be calculated from first principles by considering the energy change associated with rotation of individual spins in the host

material. These exchange interactions can be used within a mean field theory to estimate the T_c . An empirical description of the variations of the exchange energy, with inter atomic spacing called the Bethe-Slater curve is instructive in describing the effect of alloying on ferromagnetic T_c . The interplay between electron-electron Coulomb interactions and the constraints of the Pauli's exclusion principle determine the sign of the exchange interaction.

In transition metal solids a measure of the overlap between nearest neighbor d-orbital is given by the ratio of the atomic to the 3d ionic (or nearest neighbor) radius. In mean field theory the T_c can be related to the exchange energy as follows:

$$T_C = \frac{2S(S+1)}{3K_B} \sum_{ij} T_{ij} , \quad (3.35)$$

where S is the total spin angular momentum, K_B is the Boltzmann's constant and T_{ij} is the exchange interaction between atoms at the position r_i and r_j .

In first case, a unique constant exchange interaction between the magnetic atoms is assumed and the amorphous nature of the alloy is taken into account by calculating a random distribution of the local anisotropy field [4.26]. In the second approach is treating this problem of distribution of exchange integrals assumed in order to reflect the structural fluctuations in the amorphous alloy [4.28]. Both approaches predict that M vs. T curve will flat below that for the crystalline counterpart.

CHAPTER IV

EXPERIMENTAL DETAILS

EXPERIMENTAL DETAILS

4.1 Thermal Analysis Techniques

Thermal analysis comprises of a group of techniques in which a physical property of a substance is measured as a function of temperature, while the substance is subjected to a controlled temperature program. The differential Thermal Analysis (DTA) is an important technique for studying the structural change occurring both in solid and liquid materials under heat treatment. These changes may be due to dehydration, transition from one crystalline variety to another, destruction of crystalline lattice, oxidation, decomposition etc. The principle of DTA consists of measuring the heat changes associated with the physical or chemical changes that occur when a standard substance is gradually heated. This technique can also be used to identify magnetic ordering of nanocrystalline amorphous ribbons. The related technique of differential scanning calorimetry relies on difference in energy required to maintain the sample and reference at an identical temperature.

This technique has been used in determining the first crystallization temperature (T_{x_1}) and second crystallization temperature (T_{x_2}) of our nanocrystalline soft magnetic materials. The first crystalline temperature is defined as the temperature at which the alloy passes from the solid to liquid state. For our study, it is sufficient to describe T_{x_1} as the temperature at which atomic mobility is great enough to allow diffusive rearrangement to occur in a matter of minutes. The crystallization temperature T_{x_2} is defined as the temperature at which crystallization occurs with long range ordering. Metallic nanocrystalline glasses ribbons usually are ductile in the as quenched condition, but may often embrittled by exposure to elevated temperature.

DTA technique have been used in determining T_{x_1} and T_{x_2} of our nanocrystalline ribbon of composition $\text{Fe}_{73.5-x}\text{Cr}_x\text{Nb}_3\text{Cu}_1\text{Si}_{13.5}\text{B}_9$ [$x = 7, 9, 10 \& 12.5$]. Based on Kissinger plots, crystallization activation energy of T_{x_1} and T_{x_2} phases have been evaluated.

4.1.1 The Principle of Differential Thermal Analysis

The DTA technique was first suggested by Le Chatelier [4.1] in 1887 and was applied to the study of clays and ceramics. DTA involves heating or cooling a test sample and inert reference under identical conditions, while recording any temperature difference between the sample and reference. DTA is the process of accurately measuring the difference in temperature between a thermocouple embedded in a sample and a thermocouple in a standard inert material such as aluminum oxide, while both are being heated at a uniform rate. These differences of temperature arise due to phase transition or chemical reactions in the sample involving the evolution of heat or absorption of heat due to exothermic reaction or endothermic reaction measured. The exothermic and endothermic reactions are generally shown data in the DTA trace as positive and negative deviations respectively from a baseline. Then this differential temperature is plotted against time, or against temperature. When a sample and reference substance are heated or cooled at a constant rate under identical environment, their temperature differences are measured as a function of time or temperature as shown by the curve in Fig.4.1 (a).

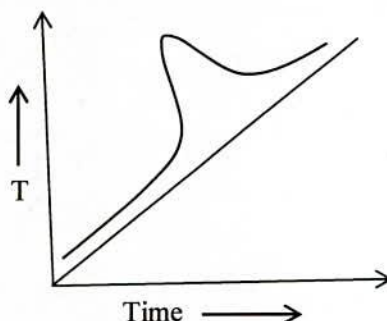


Fig. 4.1(a) Heating curve of sample and reference substance

The temperature of the reference substance, which is thermally inactive, rises uniformly when heated, while the temperature of the sample under study changes anomalously when there is physical or a chemical change of the active specimen at a particular temperature. When there is an exothermic reaction there is a peak in the temperature versus time curve, heat supplied from outside is consumed by the reaction. And when the reaction is over, the sample temperature gradually catch up the temperature of the inactive specimen. The temperature difference ΔT is defined, amplified and recorded by a peak as shown in Fig. 4.1 (b).

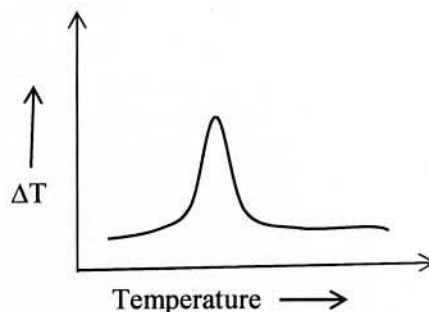


Fig. 4.1(b) DTA Curve

For any endothermic reaction or change the active specimen absorbs heat which is reflected in the corresponding the trough in temperature versus time curve. Changes in the sample, which leads to the absorption or evolution of heat, can be detected relative to the inert reference. Differential temperatures can also arise between two inert samples when their response to the applied heat treatment is not identical. DTA can therefore be used to study thermal properties and phase changes which do not lead to a change in enthalpy.

Changes in the sample, either exothermic or endothermic, can be detected relative to the inert reference. Thus, a DTA curve provides data on the transformations that have occurred, such as glass transitions, crystallization, melting and sublimation. The baseline of the DTA curve showed then exhibit discontinuities at the transition temperatures and the slope of the curve at any point will depend on the microstructural constitution at that temperature. The area under a DTA peak can be related to the enthalpy change and is not affected by the heat capacity of the sample. DTA may be defined formally as a technique for recording the difference in temperature between a substance and a reference material against either time or temperature as the two specimens are subjected to identical temperature regimes in an environment either heated or cooled at a controlled rate.

4.1.2 Apparatus

The key features of a DTA kit are as shown in Fig. 4.2 sample holder comprising thermocouples, sample containers and a ceramic or metallic block, a furnace, temperature programmer, recording system. The essential requirements of the furnace are that it should provide a stable and sufficiently large hot-zone and must be able to respond rapidly to commands from the temperature programmer. A temperature programmer is essential in order to obtain constant heating rates. The

recording system must have a low inertia to faithfully reproduce variations in the experimental set-up.

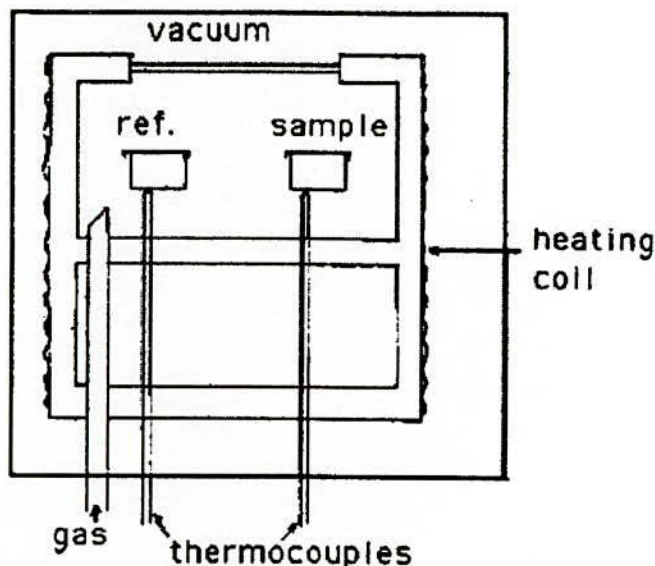


Fig. 4.2 Schematic illustration of a DTA cell

The sample holder assembly consists of a thermocouple each for the sample and reference, surrounded by a block to ensure an even heat distribution. The sample is contained in a small crucible designed with an indentation on the base to ensure a snug fit over the thermocouple bead. The crucible may be made of materials such as Pyrex, Silica, Nickel or Platinum, depending on the temperature and nature of the tests involved. The thermocouples should not be placed in direct contact with the sample to avoid contamination and degradation, although sensitivity may be compromised. Metallic blocks are less prone to base-line drift when compared with ceramics which contain porosity. On the other hand, their high thermal conductivity leads to smaller DTA peaks.

The sample assembly is isolated against electrical interference from the furnace wiring with an earthed sheath, often made of platinum-coated ceramic material. The sheath can also be used to contain the sample region within a controlled atmosphere or a vacuum. The specimen holder is placed in the cavity of the heating block which is operated in the center of the cylindrical refractory tube of an electrical furnace. This supply is a uniform heating rate. The furnace is peked with calcined china clay. The input of current into the furnace is secured through the secondary of a Variac transformer, which controls the currents. Fine Chromelalumel wires (28

gauges) are used for thermocouples. A cold junction is used for thermocouple leads and the e.m.f. is recorded almost continuously, while the temperature of the inert material is measured at 3 minute intervals. It is essential to use perfectly dry materials, as otherwise errors will be introduced in the analysis. Approximately 0.1 gm anhydrous alumina is used in the reference cup and the sample weight varies over a range 0.05 to 0.125 gm; depending on their density. A heating rate of 10°C to 50°C per minute of the furnace is conveniently chosen and this gives satisfactory results in most case. A block diagram of DTA as shown in Fig. 4.3

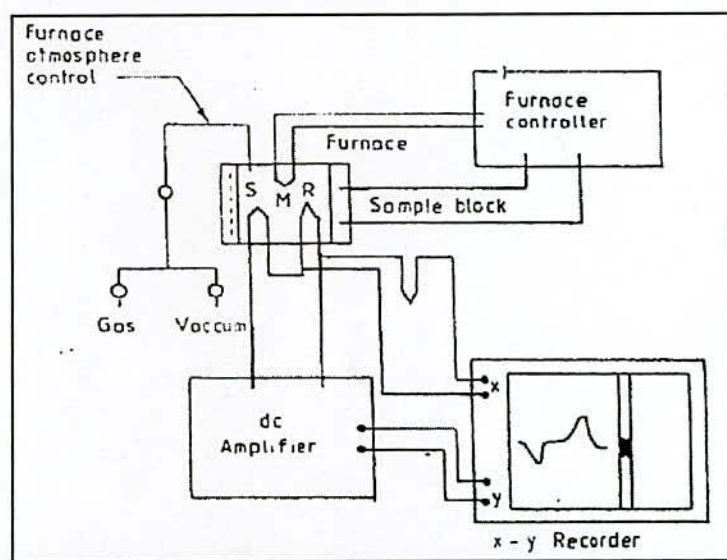


Fig. 4.3 Block diagram of a DTA equipment, (S) sample thermocouple, (R) Reference thermocouple, (M) Monitor thermocouple

During experiments a temperature problems are encountered in transferring heat uniformly away from the specimen. These may be mitigated by using thermocouples in the form of flat discs to ensure optimum thermal contact with the new flat-bottomed sample container, made of aluminum or platinum foil. To ensure reproducibility, it is then necessary to ensure that the thermocouple and container are consistently located with respect to each other.

4.1.3 Experimental Factors

It is necessary in care to selecting the experimental parameters. For example, the effects of specimen environment, composition, size and surface to volume ratio all affect powder decomposition reactions, whereas these particular variables may not

affect solid state phase changes. Experiments are frequently performed on powders so the resulting data may not be representative of bulk samples, where transformations may be controlled by the build-up of strain energy. The packing state of any powder sample becomes important in decomposition reactions and can lead to large variations between apparently identical samples.

In some circumstances, the rate of heat evolution may be high enough to saturate the response capability of the measuring system; it is better than to dilute the test sample with inert material. For the measurement of phase transformation temperatures, it is advisable to ensure that the peak temperature does not vary with sample size. The shape of a DTA peak does depend on sample weight and the heating rate used. The influence of heating rate on the peak shape and disposition can be used to advantage in the study of decomposition reactions, but for kinetic analysis it is important to minimize thermal gradients by reducing specimen size or heating rate.

4.1.4 Interpretation and Presentation of DTA

There are difficulty to the measurement of transition temperatures using DTA curves. The onset of the DTA peak in principle gives the start-temperature, but there may be temperature lags depending on the location of the thermocouple with respect to the reference and test samples or the DTA block. It is wise to calibrate the apparatus with materials of precisely known melting points. The peak area (A), which is related to enthalpy changes in the test sample, is that enclosed between the peak and the interpolated baseline. When the differential thermocouples are in thermal, but not in physical contact with the test and reference materials, it can be shown that A is given by,

$$A = \frac{mq}{gk} \quad (4.1)$$

where m is the sample mass, q is the enthalpy change per unit mass, g is a measured shape factor and k is the thermal conductivity of sample.

With porous, compacted or heaped samples, the gas filling the pores can alter the thermal conductivity of the atmosphere surrounding the DTA container and lead to large errors in the peak area. The situation is made worse when gases are evolved from the sample, making the thermal conductivity of the DTA-cell environment different from that used in calibration experiments. The DTA apparatus is calibrated

for enthalpy by measuring peak areas on standard samples over specified temperature ranges. The calibration should be based upon at least two different samples, conducting both heating and cooling experiments.



Fig. 4.4 SII EXSTAR 6000 TG/DTA 6300 assembly

In the present work, SEIKO Instruments Inc. (SII) EXSTAR 6000 TG/DTA 6300 has been used for thermal analysis shows in Fig. 4.4. The Thermo gravimetric / Differential Thermal Analyzer (TG/DTA) combine the flexibility of DTA with the proven capabilities of the TG measurement technology, providing property information for a verity of samples. Thus simultaneous TG/DTA System can be used for such application as oxidation, heat resistance, and the amount of water, compositional analysis and measurement of ash contents in a sample. This system is also used to cover such need as reaction rate and accelerated degrading tests.

The thermal analysis runs generally for 1 to 1.5 hrs. Thermal analysis curves are obtained by plotting heating temperature and the difference between the temperature of the test and reference substances. From these plots the reaction temperature could be determined. Under standard conditions of the experiment; characteristic curves for different compositions of $\text{Fe}_{73.5-x}\text{Cr}_x\text{Nb}_3\text{Cu}_1\text{Si}_{13.5}\text{B}_9$ [$x = 7, 9, 10 \& 12.5$] nanocrystalline amorphous ribbons. T_{x_1} and T_{x_2} points are indicating the sharp exothermic peaks.

All experiments are run at atmospheric pressure in continuous flow of purified inert gas Nitrogen. Gases are normally purged into the furnace chamber at the lower

end through a purification train in which oxygen and water are removed by heated copper wool and exhausted from the top into a condensate trap for collecting the condensable volatile products.

A. The Features are:

- (i) The TG/DTA can operate in either DSC or DTA mode. In DSC mode it displays heat flow signal.
- (ii) The horizontal differential balance provides high sensitivity and accuracy.
- (iii) Gas control unit automatically control the environment of the furnace between measurements.
- (iv) Auto sampler with 30 samples positions provides laboratory automation and increase productivity.
- (v) Through the utilization of an automatic cooling unit, the instrument is now automatically cooled to a set temperature after measurements, which raises the effectiveness of measurements.

B. Specification:

Temperature Range	: Room temperature to 1500°C (normally around 1300°C)
Balance Method	: Horizontal differential type
Maximal sample weight	: 200mg;
Program rate	: 0.01 to 100°C/min
Automatic Cooling unit	: Force Air Cooling
Gas flow rate	: 0 to 1000ml/min
Cooling rate	: less than 15 min from 1000 to 50°C
Atmosphere	: Air, Inert gas, Vacuum (10 ⁻² Torr)
Sample pan material	: Platinum, Alumina and Aluminum.
TG measurement Range/Sensitivity	: 200 mg /0.2µg
DTA measurement / Sensitivity	: +1000µV/ 0.06µV

4.2 Annealing

Annealing in metallurgy and materials science, is heat treatment where in a material is altered, causing changes in its properties such as strength and hardness. It is a process that produces conditions by heating to above the critical temperature, maintaining a suitable temperature and then cooling. Annealing is used to induce

ductility, soften material, relieve internal stresses, refine the structure by making it homogeneous and improve cold working properties.

In the cases of copper, steel, silver and brass, this process is performed by substantially heating the material (generally until glowing) for a while and allowing it to cool. Unlike ferrous metals, which must be cooled slowly to anneal, copper, silver and brass can be cooled slowly in air or quickly by quenching in water. In this fashion the metal is softened and prepared for future work such as shaping, stamping, or forming.

Annealing occurs by the diffusion of atoms within a solid material, so that the material progresses towards its equilibrium state. Heat is needed to increase the rate of diffusion by providing the energy needed to break bonds. The movement of atoms has the effect of redistributing and destroying the dislocations in metals and (to a lesser extent) in ceramics. This alternation in dislocations allows metals to deform more easily, so increases their ductility.

4.2.1 Stages

There are three stages in the annealing process, with the first being the recovery phase, which results in softening of the metal through removal of crystal defects (the primary type of which is the linear defect called a dislocation) and the internal stresses which they cause. Recovery phase covers all annealing phenomena that occur before the appearance of new strain-free grains. The second phase is recrystallization, where new strain-free grains nucleate and grow to replace those deformed by internal stresses. If annealing is allowed to continue once recrystallization has been completed, grain growth will occur, in which the microstructure starts to coarsen and may cause the metal to have less than satisfactory mechanical properties.

4.2.2 Setup and Equipment

Typically, large ovens are used for the annealing process. The inside of the oven is large enough to place the work piece in a position to receive maximum exposure to the circulating heated air. For high volume process annealing, gas fired conveyor furnaces are often used. For large work piece or high quantity parts, car-bottom furnaces will be used in order to move the parts in and out with ease. Once the

annealing process has been successfully completed, the work pieces are sometimes left in the oven in order for the parts to have a controlled cooling process. While some work pieces are left in the oven to cool in a controlled fashion, other materials and alloys are removed from the oven. After being removed from the oven, the work pieces are often quickly cooled off in a process known as quench hardening. Some typical methods of quench hardening materials involve the use of media such as air, water, oil or salt. Quench hardening is generally applicable for some ferrous alloys, but not copper alloys.

4.3 Thermal Treatment of the Nanocrystalline Amorphous Ribbon

With a view to study nanocrystallization behavior by XRD and magnetic properties upon evaluation of nanocrystalline phase on amorphous matrix, thermal treatment, i.e. annealing is required to perform. For XRD, as prepared amorphous ribbon were cut into small pieces of about 2cm lengths for annealing treatment. MTI Corporation built GSL-1600x40 tube furnace used for this purpose shown in Fig. 4.5. The samples were put into the tube and filled up with Nitrogen gas before the tube furnace heated to a predefined temperature and kept for the time (30 minute) required completing the annealing. In this way all the isothermal annealing as a function of time were performed.



Fig. 4.5 MTI - GSL-1600x40 Tube Furnaces

4.4 Powder / Polycrystalline Diffraction

About 90% of all solid materials can be described as crystalline. When X-ray interacts with a crystalline substance (phase) one get a diffraction pattern. The X-ray diffraction pattern of a pure substance is, therefore, like a fingerprint of the substance. The powder diffraction method is thus ideally suited for characterization and identification of polycrystalline phases. Today about 50000 inorganic and 25000 organic single components, crystalline phase and diffraction patterns have been collected and stored on magnetic or optical media as standard. The main use of powder diffraction is to identify components in a sample by a search match procedure. Furthermore, the areas under the peak are related to the amount of each phase present in the sample.

4.4.1 Theoretical Considerations of X-ray Diffraction (XRD)

The German Physicist Wilhelm Roentgen discovered X-rays in 1895. X-rays are electromagnetic waves of short wavelengths in the range of 10^{-2} to 10^2 \AA . Unlike ordinary light, these rays are invisible, but they travel in straight lines and affect photographic film in the same way as light. On the other hand, they were much more penetrating than light and could easily pass through the human body, wood, quite thick pieces of metal and other "opaque" objects.

The XRD provides substantial of information on the crystal structure. XRD is one of the oldest and effective tools for the determination of the atomic arrangement in a crystal. The wavelength (1 \AA) of an X-ray is the same order of magnitude as the lattice constant of crystals and it is this which makes X-rays so useful in structural analysis of crystal. Whenever X-rays are incident on a crystal surface, they are reflected from it. The reflection abides by the Bragg's Law as given below

$$2d \sin \theta = n\lambda \quad (4.2)$$

Where d is the distance between crystal planes, θ is the incident angle, λ is the wavelength of the X-ray and n is a positive integer. Bragg's Law also suggested that the diffraction is only possible when $\lambda < 2d$.

X-ray diffractograms of all the samples were recorded using monochromatic Cu- K_{α} radiation ($\lambda = 1.54053 \text{ \AA}$) to ensure the formation of single-phase nature of the product. XRD patterns information are: scanning speed 2° , chart speed 20mm, starting from 20° and ending at 90° . Peak intensities are recorded corresponding to their 2 θ

values. The inter planner distance d was calculated from these 2θ values of the diffraction peaks using the Bragg's Law (In Fig. 4.6).

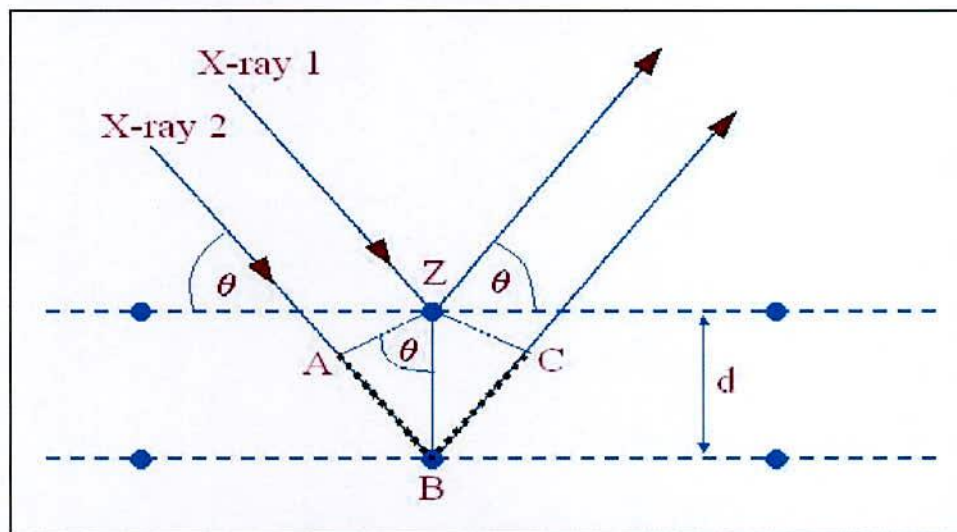


Fig. 4.6 Bragg's diffraction pattern

Therefore the two possible values where we can have reflections are determined by the unit cell dimensions. However, the intensities of the reflection are determined by the distribution of the electrons in the unit cell. The highest electron density is found around atoms. Therefore, the intensities depend on what kind of atoms we have and where in the unit cell they are located. Planes going through areas with high electron density will reflect strongly, planes with low electron density will give weak intensities.

4.4.2 X-ray Powder Method

Powder method is perhaps the most widely used X-ray diffraction technique for characterizing materials. The term 'powder' really means that the crystalline domains are randomly oriented in the sample. Therefore, when the 2-D diffraction pattern is recorded, it shows concentric rings of scattering peaks corresponding to the various d spacing in the crystal lattice. The positions and the intensities of the peaks are used for identifying the underlying structure (or phase) of the material. Powder diffraction data can be collected using either transmission or reflection geometry, as shown in Fig. 4.7 below.

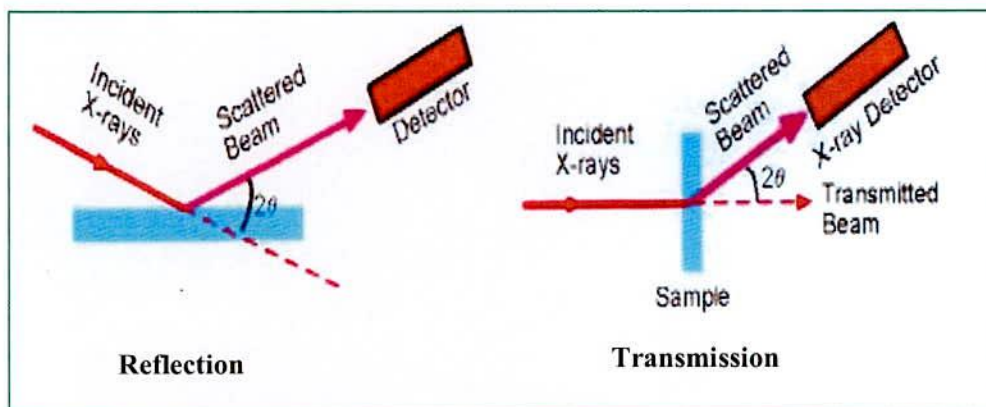


Fig. 4.7 Reflection and Transmission geometry of powder diffraction

Because the particles in the powder sample are randomly oriented, these two methods will yield the same data. Powder diffraction data are measured using Bruker AXS D8 Advance diffractometer, which measures data in reflection mode and is used mostly with solid samples, or the custom built 4-circle diffractometer, which operates in transmission mode and is more suitable for liquid phase samples.

4.4.3 Experimental Technique for X-ray Diffractometer

X-ray diffraction (XRD) is a versatile non-destructive analytical technique for identification and quantitative determination of various crystalline phases of powdered or solid samples of any compound. For each set of composition, ribbons are cut into several pieces; each of length 20 mm. Heat treatment was performed on the amorphous ribbons using a tube furnace which filled with Nitrogen gas. After the heat treatment, samples were removed from the furnace tube carefully and kept separately for XRD experiment.

For XRD experiment each sample was set on a glass slides and fixed the sample by putting adhesive tape at the two ends of the sample. After the pattern is obtained the value of 2θ is calculated for each diffraction line; set of 2θ values is the raw data for the determination of the lattice parameters of the unit cell. Fig. 4.8: Shows the block diagram of Bruker AXS D8 Advance X-ray diffractometer. The Bucker AXS D8 Advance X-ray diffractometer was used for the lattice parameter determination in the PP & PDC, Materials Science Division, Bangladesh Council of Scientific and Industrial Research (BCSIR), Dhaka. Fig. 4.9 shows the inside view of the Bucker AXS D8 Advance XRD system. The Bruker AXS D8 Advance diffraction

system utilizes a modular system approach to provide performance for application ranging from routine characterization to in-depth research investigation.

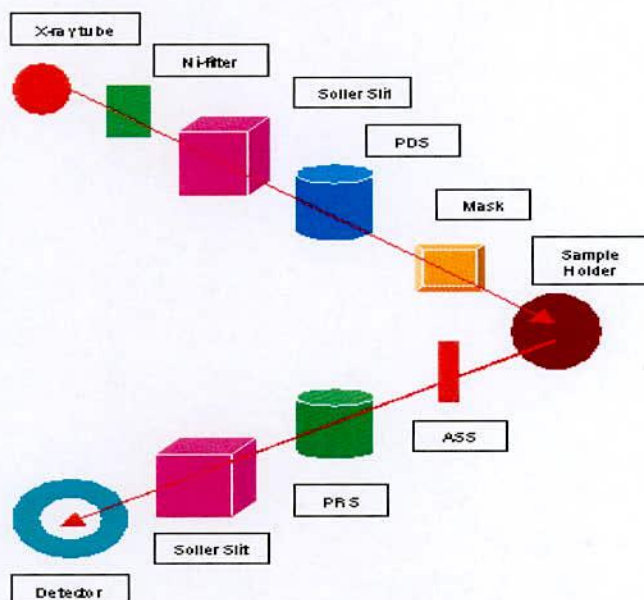


Fig. 4.8 Block diagram of the Bruker AXS D8 Advance XRD system

The powder diffraction technique was used with a primary beam power of 40 kV and 40 mA for Cu radiation. A nickel filter was used to reduce Cu-K_{α} radiation and finally Cu-K_{α} radiation was only used as the primary beam. A $(\theta-2\theta)$ scan was taken from 30° to 90° to get possible fundamental peaks of the sample with the sampling pitch of 0.02° and time for each step data collection was 1.0 sec. Both the programmable divergence and receiving slits were used to control the irradiated beam area and output intensity from the sample respectively.

An anti-scatter slit was used just after the sample holder to reduce air scattering. Two solar slits were used just after the tube and in front of the detector to get parallel beam only. All the data of the samples were stored in the computer memory and for later analysis that using computer software “*DIFFRAC^{plus}*”.

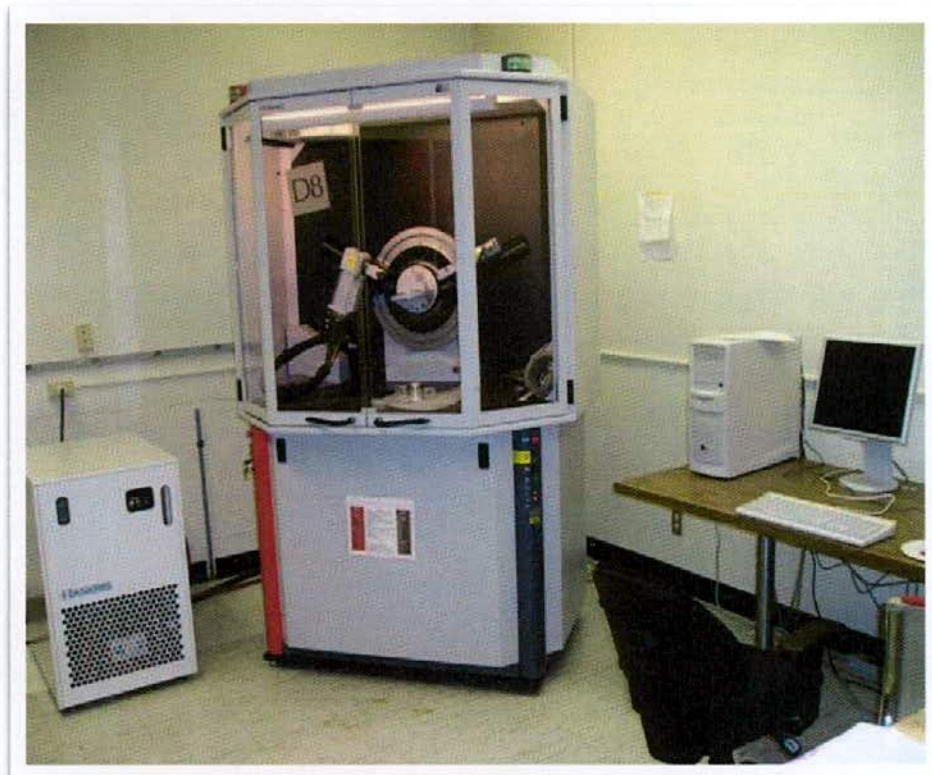


Fig. 4.9 Bruker AXS D8 Advance

The Bruker AXS D8 ADVANCE has the ability to perform a full range of applications, from qualitative and quantitative phase identification, under ambient or non-ambient conditions, to crystal structure solution from powder samples, crystallite size determination, micro strain analysis, residual stress analysis, and preferred orientation.

Bruker AXS D8 Advance SPECIFICATIONS	
X-RAY SOURCE	2.2kW Cu and Co, Running condition (40kV, 40mA), Power stability is better than 0.01%
DETECTORS	Point detector, Vantec-1 detector
OPTICS	Gobel Mirror
GONIOMETER	High precision microprocessor controlled, two circle goniometer with independent stepper motors and optical encoders; Smallest angular step 0.0001°; Reproducibility +/- 0.0001°
SAMPLE STAGE	Centric ¼-Circle Eulerian Cradle. Motorized Chi (tilt) and Phi (rotation) rotations and X-Y-Z translations. The cradle accommodates bulky specimens, powders, thin-films, and wafers up to 80 x 50 x 20 mm and weighing up to 1 kg
ATTACHEMENTS	High Temperature MRI stage (RT-1400C), Thin Film Reflectometry, sample spinner, video camera, sample plate with 9-sample holders
SOFTWARE	LEPTOZ, TOPAZ, ICCD

Attributes	
Depth	1135 mm
Height	1868 mm
Width	1300 mm
Weight	770 kg
Additional Specifications	<p>Configurations: Vertical goniometer, Theta/2Theta or Theta/Theta geometry Measuring circle diameter: Predefined at 500 mm, 560 mm and 600 mm or any intermediate setting Angular range: 360° Max. usable angular range: $-110^\circ < 2\Theta < 168^\circ$ Angle positioning: Stepper motors with optical encoders Smallest addressable increment: 0.0001° Instrument alignment: Equal or better than $\pm 0.01^\circ 2\Theta$; NIST SRM 1976a always included Maximum angular speed: 20°/s Detectors: Point detectors: Scintillation counter SOL-XE energy dispersive 1-D detectors: LYNXEYE, VANTEC-1 All detectors guaranteed without defective/dead strips or areas Cooling water supply: Min. 4 l/min, pressure 4 bar to 7.5 bar, no pressure on outlet side, temperature: 10 °C to 20 °C Power supply: Single phase: 208 to 240 V, Three phases: 120 V, 230 V, 240V; 47 to 63 Hz</p>

4.4.4 Analysis of XRD data

The XRD data consisting of θ_{hkl} and d_{hkl} values corresponding to the different planes from which the following structural information of the nanocrystalline ribbon sample was evaluated.

- (i) Identification of phases
- (ii) Lattice parameter determination
- (iii) Average grain size determination
- (iv) Si- content determination in nanograins

(i) Identification of phases

The most common use of powder (polycrystalline) diffraction is chemical analysis. This can include phase identification (search/match), investigation of high/low temperature phase, solid solutions and determination of unit cell parameter of new materials.

XRD has become a very popular and useful instrument for routine X-ray analysis of nanocrystalline amorphous ribbon samples. In fact the diffractometer technique is often preferred to Debye-Scherrer technique owing to its several inherent merits. The most striking difference between the two methods is in the use of different intensity detection and measuring devices. XRD pattern of as-cast indicates just amorphous pattern of the given composition. The XRD patterns are identified as bcc α -Fe(Si) solid solution, which are developed on the nanocrystalline amorphous ribbon after heat treatment. The peak pattern is observed for all the samples at different heat treatment temperatures indicating the bcc α -Fe(Si) phase, which is developed on amorphous ribbons after heat treatment. Present experiment reveals that 450°C is not sufficient temperature to start forming of crystalline nanograins of bcc Fe(Si) on the amorphous ribbon of the studied alloy composition.

(ii) Lattice Parameter Determination

Lattice parameter of crystalline bcc Fe-Si nanograin has been determined for all the two different amorphous compositions at different heat treatment temperatures. Normally, lattice parameter of an alloy composition is determined by the Debye-Scherrer method after extrapolation of the curve. In the present case, only one reflection (110) is prominent in all XRD patterns and we would like to understand how the value of lattice parameter changes with annealing temperatures. We have, therefore, determined the lattice parameter using only that particular reflection using equation $2d \sin \theta = \lambda$ and $a_0 = d\sqrt{2}$, where $\lambda = 1.54178 \text{ \AA}$ for $Cu - K_{\alpha}$ radiation and a_0 is the determined lattice parameter within an error estimated to be $\pm 0.0001 \text{ \AA}$.

(iii) Grain Size Determination

The main aim (vital point) of the present study is to determine the nanocrystalline grain size for all the heat treated samples of the alloy composition by using Scherrer method. The XRD pattern of (110) reflection for different steps of heat treatment temperature of the alloy composition is used to calculate grain size. Grain size is determined using the following formula,

$$D_g = \frac{0.9\lambda}{\beta \cos \theta} \quad (4.3)$$

Where $\lambda = 1.54178\text{\AA}$ for $Cu-K_{\alpha}$ radiation and β = FWHM (full width at half maximum) of the peak in radian. Considering β in degree we get the following relation

$$D_g = \frac{79.5}{\beta \cos \theta} \quad (4.4)$$

All the values of grain size for every step of heat treatment temperature of the alloy composition were determined. The FWHM of the peak is large at the early heat treatment temperature and with the increase of heat treatment temperature; the value of FWHM becomes smaller which means that the grain size is increasing gradually.

(iv) Si-content in Nanograins

Crystalline nanograins were formed on the amorphous matrix of the ribbon in the process of heat treatment having the composition of Fe-Si. It is, therefore important to determine the concentration of Fe and Si in the nanograin [2.13]. As because the alloy consists of Fe and Si and we have experimentally determined the lattice parameter of the alloy nanograin for the two compositions at different temperatures. It is easy to calculate the Si content in the nanograins from the data of Pearsons who was established the relationship between the lattice parameter as dependent on Si content in Fe-Si alloys covering a wide range of compositions [4.2]. From the relationship, we have constructed a simple equation to calculate Si content from lattice parameter. The equation is

$$X = \frac{(a_0 - 2.8812)}{0.0022} \quad (4.5)$$

where X is at. % Si in the nanograins, a_0 is the determined lattice parameter of nanograins. Si-contents for the nanograin develop during the isothermal annealing at various temperatures have been calculated.

4.5 Magnetization Measurement Techniques

In the present study magnetization has been performed using a Vibrating Sample Magnetometer (VSM).

4.5.1 Vibrating Sample Magnetometer (VSM)

A vibrating sample magnetometer (VSM) operates on Faraday's Law of Induction, which tells us that a changing magnetic field will produce an electric field.

This electric field can be measured and can tell us information about the changing magnetic field. A VSM is used to measure the magnetic behavior of magnetic materials. VSM is a versatile and sensitive method of measuring magnetic properties developed by S. Foner [4.3-4.4] and is based on the flux change in a coil when the sample is vibrated near it. The VSM is designed to continuously measure the magnetic properties of materials as a function of temperature and field. In this type of magnetometer, the sample is vibrated up and down in a region surrounded by several pickup coils. The magnetic sample is thus acting as a time-changing magnetic flux, varying inside a particular region of fixed area. From Maxwell's law it is known that a time varying magnetic flux is accompanied by an electric field and the field induces a voltage in pickup coils. This alternating voltage signal is processed by a control unit system, in order to increase the signal to noise ratio. The result is a measure of the magnetization of the sample.

4.5.2 Principle of VSM

The principle of VSM is as follows: when the sample of a magnetic material is placed in a uniform magnetic field, a dipole moment proportional to the product of the sample susceptibility times the applied field is induced in sample. If the sample is made to undergo a sinusoidal motion, an electrical signal is induced in suitably located stationary pick-up coils. This signal which is at the vibrating frequency, is proportional to the magnetic moment, vibration amplitude and vibration frequency. In order to obtain the reading of the moment only, a capacitor is made to generate another signal for comparison which varies in its moment, vibration amplitudes and vibration frequency in the same manner as does the signal from the pick-up coil. These two signals are applied to the two inputs of a differential amplifier, and because the differential amplifier passes only difference between the two signals, the effects of vibration amplitude and frequency changes are cancelled. Thus only the moment determines the amplitude of the signal at the output of the differential amplifier. This signal is in turns applied to a lock-in amplifier, where it is compared with the reference signal which is at its internal oscillator frequency and is also applied to transducer which oscillation the sample rod. Thus the output of the lock-in amplifier is proportional to the magnetic moment of the sample only avoiding any noise of frequency other that of the signal. The lock-in action yields an accuracy of 0.05% of

full scale. The absolute accuracy of this system is better than 2% and reproducibility is better than 1%. Least measurable moment is 5×10^{-4} emu.



Fig. 4.10 Vibrating Sample Magnetometer (VSM)

These measurements were carried out at Materials Science Division, Atomic Energy Center, Dhaka. We use Hirst VSM02 which is an automatic VSM for characterization of soft and hard magnetic materials manufactured by HIRST Magnetic Instruments Ltd. The Hirst VSM system arrangement is shown in the Fig. 4.10.

4.5.3 Electronic Circuits of the VSM

The function of the associated electronic circuits is:

- (i) To permit accurate calibration of the signal output obtained from the detection coils.
- (ii) To produce a convenient AC output signal which is directly related to the input and which can be recorded.
- (iii) To produce sufficient amplification for high sensitivity operation.

The block diagram of the electronic circuit used for the VSM consists of a mechanical vibrator, a sine wave generator, an audio amplifier, a ratio transformer, a

phase-shifter, a lock-in amplifier, a pick-up coil system, a reference coil system and an electromagnet as shown in Fig.4.11.

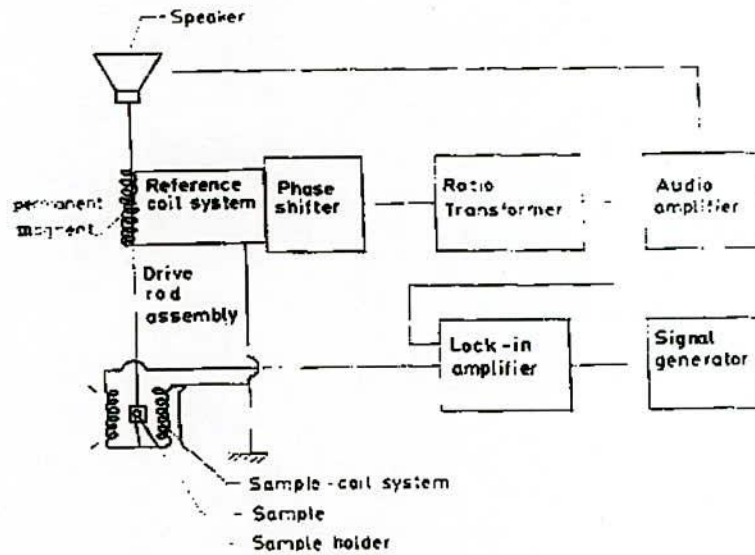


Fig. 4.11 Electronic Circuit of the VSM

The sample magnetized by the electromagnet generates an e.m.f in pick-up coils PC. The strength of this signal is proportional to the magnetization of the sample. The vibrating permanent magnet also generates an e.m.f of fixed amplitude in the surrounding reference coils. This reference signal is stepped down with the help of a ratio transformer so that its amplitude is equal to that the sample signals. The two signals are then brought in phase and put to the lock-in amplifier. The Lock-in amplifier works as a null detector. The ratio transformer reading is to be calibrated using spherical shape sample S of 99.99% pure Nickel.

4.5.3.1 Sensitivity Limits

Limits of sensitivity are determined by signal to noise ratio at the input circuit, where noise is defined as any signal not due to the sample magnetic moment of the sample. The major sources of noise are the Johnson noise of the wire used for the pickup coils, and the magnetic responses of the sample holder which superimposes undesired signals in-phase with the wanted signal. Use of a minimum mass of weakly diamagnetic material for a sample holder, carefully checked to contain no ferromagnetic impurities, is essential to minimize this coherent noise contribution. Corrections for the small magnetic contribution of the sample holder can then be

made by measurements with the sample removed. Obviously, this correction is much less than the equivalent case with a moving coil system. The simplest measurement used the standard nickel sample our standard sample used for calibration was spherical shaped specimen of mass 0.0584 gm. A change in susceptibility, Δx , of 5×10^{-9} could be detected at the oscilloscope, and $\Delta x \cong 5 \times 10^{-9}$ could be observed after synchronous phase detection (band width $\cong 2 \times 10^{-2}$ cps). The other tests used a small current carrying coil mounted in place of the sample. Either a direct current was passed through this coil as it was vibrated at 90 Hz, or an alternating current at 90 Hz was passed through the coil which remained stationary. In both cases, $\Delta x \cong 2 \times 10^{-10}$ were detectable with optimum conditions and synchronous detection. Probably a factor of 10 improvement can be expected with minor modifications. These results compare favorably with some of the most sensitive force methods. A particularly high sensitivity force method, developed by Stevens and Crawford [4.5] permits $x \cong 2 \times 10^{-10}$ to be measured.

4.5.3.2 Stability Tests of Differential Measurements

With only the Lock-in amplifier (band width $\cong 1$ Hz) and the oscilloscope as a null detector, it was found that the 0.0584 gm Ni sample signal could be balanced reproducibly. Such reproducibility indicated that the long time drifts caused by the combined effects of vibration, amplitude changes and frequency changes a bridge sample position, and any other effects not considered here were negligible. Chosen synchronous phase detector added (band width $\cong 2 \times 10^{-2}$ Hz) differential changes about one-tenth this size that could be recorded reproducibly. These results demonstrate that the average stability of the instrument is exceptional.

4.5.3.3 Vibration Amplitude

The peak-to-peak vibration amplitude has been varied from less than 0.1 mm up to 1.0 mm in order to examine errors caused by amplitude changes. Such tests show that the measured magnetic moment varied by less than $\pm 0.5\%$ over this range of amplitude, although a somewhat sharper balance is obtained at higher vibration amplitudes because of the larger signals involved. Measurements usually are made with vibration amplitudes of about 0.1 mm. Insensitivity to small amplitude variation is also demonstrated by results of Stability Tests-Differential Measurements.

4.5.3.4 Image Effects

Image effects were also examined with a small vibrating coil carrying a DC current. The image effect was no greater than $\pm 1\%$ for fields up to 5KG produced in an air gap of 3.6 cm. undoubtedly there is an image induced in the magnet poles. It appears, however, that when the sample is vibrated, the effective image vibration is reduced by eddy-current shielding.

4.5.3.5 Vibration Frequency

The vibration frequency is not critical. High-frequency operation is limited by the driving mechanism and capacitive shunting in the detection coils. Frequencies of 100 Hz or less permit use of inexpensive components and minimize eddy-current shielding by the vacuum chamber. The measurements are completely independent of eddy-currents in surrounding parts if measurements and calibration are made at the same temperature. A correction for changes of penetration depth with temperature may be required if the conducting parts are thick. The thickness of conducting parts has been minimized, so that the temperature dependence of penetration depth is less than 1%.

4.5.3.6 Vibration Problems

Mechanical coupling between the vibrating system and the fixed detection coils must be avoided. Although the coils are arranged for minimum sensitivity to external vibration, a noticeable background signal is obtained when the vacuum chamber contacts the detection coils. Such mechanical effects are difficult to eliminate electronically, because the spurious background signal has the same frequency as the sample signal and maintains a constant phase difference with respect to the sample signal. The unwanted background signal may also be field-dependent if the coils subtend a region of non-uniform field. Usually the magnetometer and detection coils are both supported by the magnet, so that some mechanical coupling may be noticed at highest sensitivity. This effect can be eliminated by shock-mounting either the magnetometer or the detection coil system as required by the particular experiment. Rigid clamping of the detection coils to the magnet pole faces has also been successful.

CHAPTER V

RESULTS AND DISCUSSION

RESULTS AND DISCUSSION

5 Results and Discussion

5.1 Crystallization Behavior of Fe-Cr-Cu-Nb-Si-B Alloys

The crystallization kinetics of magnetic amorphous nanocrystalline alloys has enormous scientific and technological interest because the enhancement as well as deterioration of magnetic properties extremely depends on the degree of crystallization. Crystallization kinetics is often determined from Differential Scanning Calorimetry (DSC), Differential Thermal Analysis (DTA) and magnetic materials from Thermo Mechanical Analysis (TMA) [5.1-5.3]. The calorimetric studies of amorphous alloys provide substantial fundamental information concerning the kinetics of the crystallization have been studied calorimetrically by Clements and Cantor [5.4] and both calorimetrically and magnetically by Luborsky [5.5] in a variety of amorphous magnetic alloys. Crystallization has also been studied by a variety of techniques including high resolution transmission electron microscope (HRTEM), in-situ XRD, external X-ray absorption fine structure (EXAFS) measurements and resistance measurements. For the present research on $\text{Fe}_{73.5-x}\text{Cr}_x\text{Nb}_3\text{Cu}_1\text{Si}_{13.5}\text{B}_9$ [$x = 7, 9, 10 \text{ \& } 12.5$] nanocrystalline amorphous alloys, DTA has been performed to identify the crystallization temperatures as well as the activation energy required for crystallization. The X-ray diffraction experiment was performed to identify the evolution of phases with heat treatment.

5.2 DTA Results of Fe-Cr-Nb-Cu-Si-B ribbons as affected by Cr-content

Crystallization is a non-reversible, exothermic process [5.6]. Calorimetric studies of amorphous alloy provide substantial and fundamental information concerning the kinetics of crystallization. DTA is a direct and effective way to analyze the kinetics of nanocrystalline materials in respect of phase transition. The change of composition affects atomic ordering through nucleation and growth of crystallites. Again, the composition of alloy affects both the primary and secondary crystallized phases, because the time needed for the constituent atoms to arrange themselves in a long range order depends on their bond energies [5.7].

DTA is an important experimental tool to study crystallization kinetics of amorphous materials through which the onset of crystallization, the temperature of primary and secondary crystallization phenomena can be revealed. Fig. 5.1 displays the DTA traces with a heating rate of 50°C/min, where the primary crystallization and secondary crystallization peak temperatures are well demonstrated for the Fe_{73.5-x}Cr_xNb₃Cu₁Si_{13.5}B₉ [x = 7, 9, 10 & 12.5] nanocrystalline amorphous alloys in the form of ribbons, prepared by melt spinning technique. In each of the curves, two exothermic peaks are distinctly observed. Corresponding to different crystallization events initiated at temperature T_{x1} and T_{x2} respectively. The primary crystallization temperature T_{x1} corresponds to evolution of nanocrystalline bcc-Fe(Si) phase which provides the expected soft magnetic properties. The secondary crystallization temperature T_{x2} corresponds to the boride phase i.e. FeB and / or Fe-Cr-B phase which cause magnetic hardening of nanocrystalline alloy. Thus, the identification of these two temperatures is necessary to understand the appropriate temperature range for the heat treatment in order to achieve the nanocrystalline phase and thereby, suitable range of temperature for the application of this alloy. The numerical values of T_{x1} and T_{x2} for all the samples are shown in Table 5.1.

Table 5.1 Onset temperature of 1st and 2nd crystallization states of the nanocrystalline amorphous ribbons with composition Fe_{73.5-x}Cr_xNb₃Cu₁Si_{13.5}B₉ [x = 7, 9, 10 & 12.5] alloy during continuous heating rate 50°C/min

Cr-content at. %	1 st starting T _{x1} °C	1 st Peak T _{p1} °C	2 nd starting T _{x2} °C	2 nd Peak T _{p2} °C	T _{x2} -T _{x1} In °C	T _{p2} -T _{p1} In °C
x = 7	559.8	580.4	717.6	731.4	157.8	151.0
x = 9	548.2	571.3	705.5	718.6	157.3	147.3
x = 10	549.9	578.8	711.0	731.9	161.1	153.1
x = 12.5	577.4	592.1	705.1	718.7	127.7	126.6

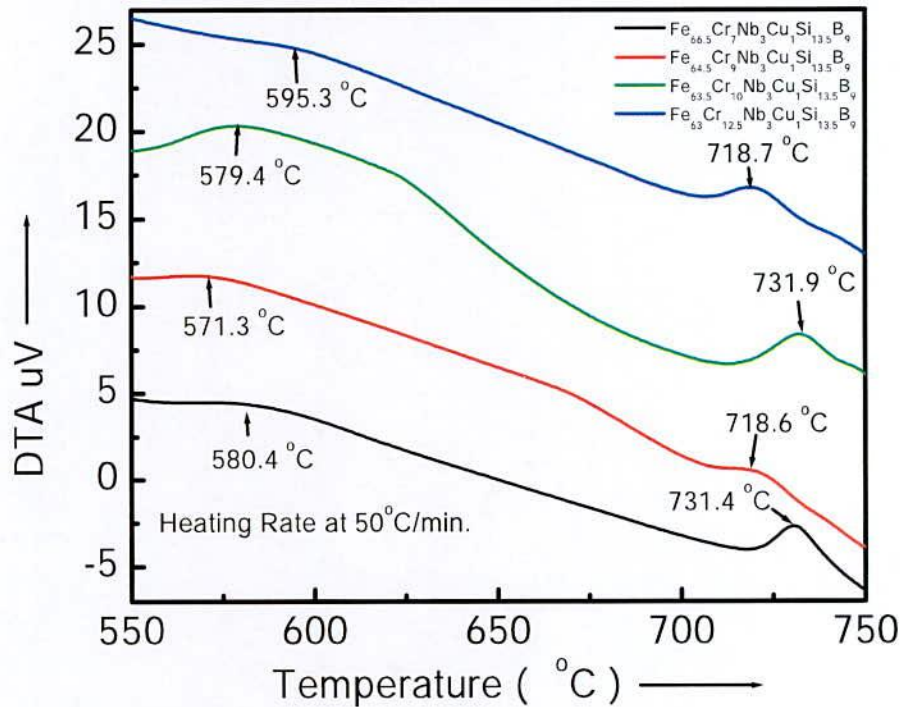


Fig. 5.1 DTA traces of as-cast nanocrystalline amorphous ribbon Fe_{73.5-x}Cr_xNb₃Cu₁Si_{13.5}B₉ [x = 7, 9, 10 & 12.5] at the heating rate of 50°C/min

It is observed from Fig. 5.1, that the crystallization of each phase has occurred over a wide range of temperatures and the primary crystallization temperatures shifts higher temperature as the Cr concentration is increased. There is a difference of $\approx 160 \pm 5^\circ\text{C}$ for the two crystallization temperature but this difference decreases as the Cr-content is increased. For x = 12.5, it is observed two crystallization peaks are close to each other. The secondary crystallization peak temperature for the boride phase is found to slightly shift lower Cr-content to upper Cr-content. The results indicate that the Cr has enhanced the thermal stability of the amorphous alloys against crystallization. This is to note that for obtaining good soft magnetic properties, T_{x1} and T_{x2} corresponding to primary and secondary crystallized phases should be well separated from each other at annealing temperature T_{x1} < T_a < T_{x2}. So that only primary crystallization product α -Fe(Si) is crystallized. The reason is that the secondary crystallization product Fe-B is extremely detrimental for the soft magnetic properties. From our results on the onset of crystallization temperature T_{x1} and T_{x2}, it is

immediately clear that the alloys with higher Cr ($x = 12.5$) are not expected to show good soft magnetic properties.

5.2.1 Study of DTA traces of $\text{Fe}_{66.5}\text{Cr}_7\text{Nb}_3\text{Cu}_1\text{Si}_{13.5}\text{B}_9$ Alloy

DTA traces of as-cast nanocrystalline amorphous ribbon $\text{Fe}_{66.5}\text{Cr}_7\text{Nb}_3\text{Cu}_1\text{Si}_{13.5}\text{B}_9$ alloy taken in nitrogen atmosphere with the heating rates of $10^\circ\text{C} - 50^\circ\text{C}/\text{minute}$ at the step of 10°C with continuous heating from room temperature to 800°C , are presented in Fig. 5.2 (a) to Fig. 5.2 (e) respectively. In each of the figure, two exothermic peaks are distinctly observed which corresponds to two different crystallization events at temperature T_{x_1} and T_{x_2} respectively. The softest magnetic ribbon corresponds to close in which primary crystallization (T_{x_1}) of $\alpha\text{-Fe}(\text{Si})$ takes place. Secondary crystallization (T_{x_2}) of Fe_2B caused magnetic hardening of the nanocrystalline alloy. Mechanical hardening of the amorphous precursor has been observed in incipient primary crystallization and attributed to Cu nucleation. Phase identification cannot be done from a DTA scan. XRD has been used for the identification of phases and would be discussed later on. Thus, the identification of these two temperature, is necessary to understand the appropriate temperature range for heat treatment in order to achieve the nanocrystalline phase and thereby, suitable range of temperature for application of alloy.

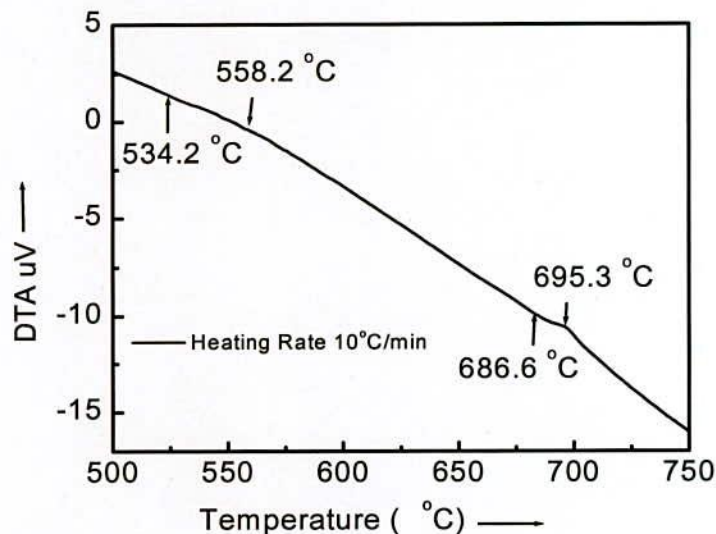


Fig. 5.2 (a) DTA trace of as-cast nanocrystalline amorphous ribbon $\text{Fe}_{66.5}\text{Cr}_7\text{Nb}_3\text{Cu}_1\text{Si}_{13.5}\text{B}_9$ at the heating rate of $10^\circ\text{C}/\text{min}$

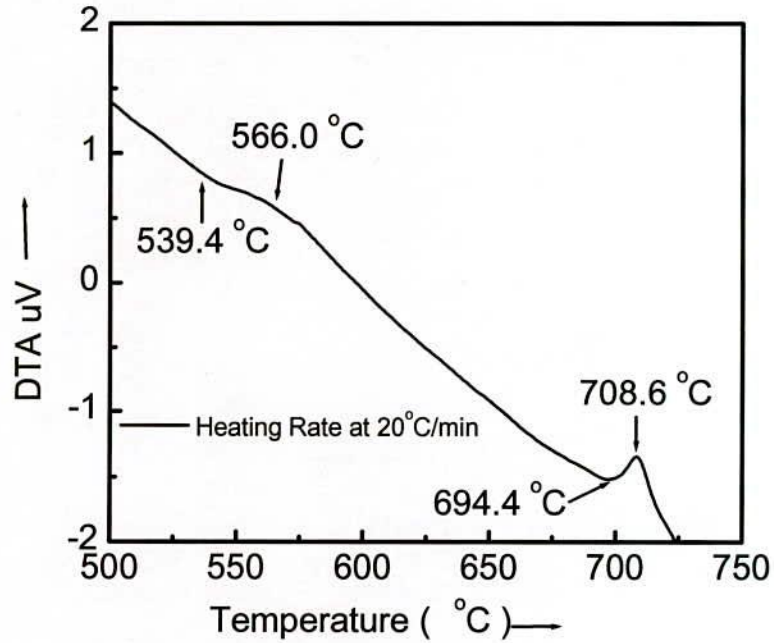


Fig. 5.2 (b) DTA trace of as-cast nanocrystalline amorphous ribbon $\text{Fe}_{66.5}\text{Cr}_7\text{Nb}_3\text{Cu}_1\text{Si}_{13.5}\text{B}_9$ at the heating rate of $20^\circ\text{C}/\text{min}$

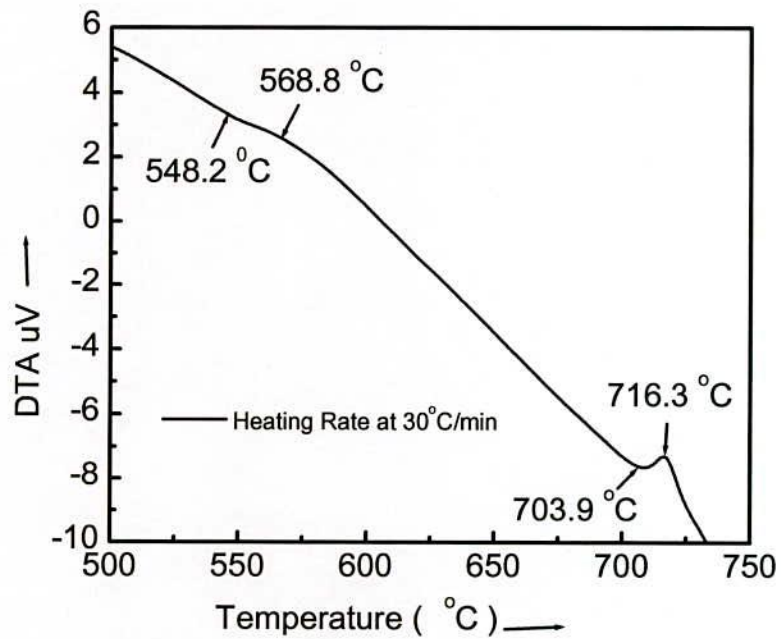


Fig. 5.2 (c) DTA trace of as-cast nanocrystalline amorphous ribbon $\text{Fe}_{66.5}\text{Cr}_7\text{Nb}_3\text{Cu}_1\text{Si}_{13.5}\text{B}_9$ at the heating rate of $30^\circ\text{C}/\text{min}$

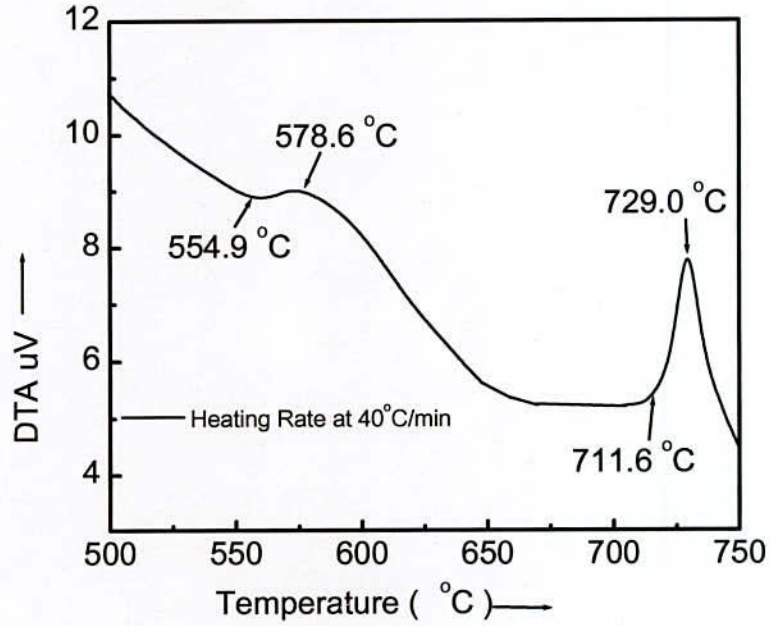


Fig. 5.2 (d) DTA trace of as-cast nanocrystalline amorphous ribbon $\text{Fe}_{66.5}\text{Cr}_7\text{Nb}_3\text{Cu}_1\text{Si}_{13.5}\text{B}_9$ at the heating rate of $40^\circ\text{C}/\text{min}$

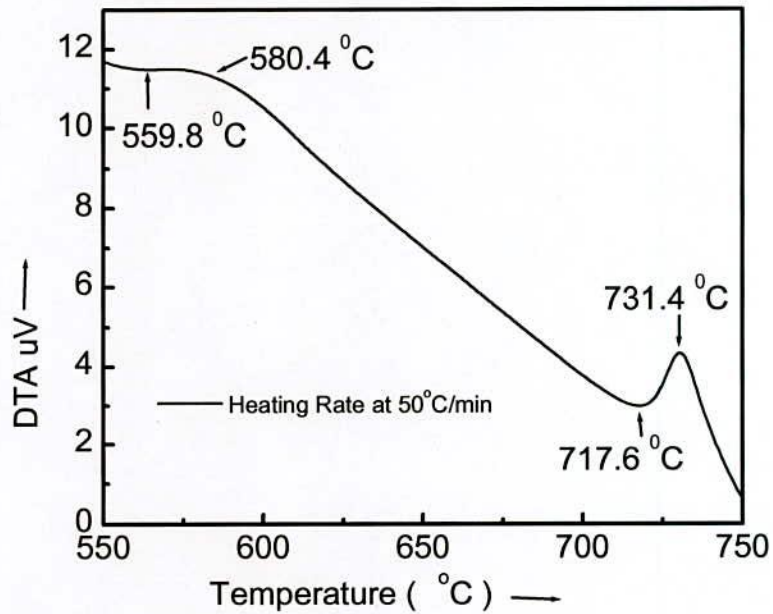


Fig. 5.2 (e) DTA trace of as-cast nanocrystalline amorphous ribbon $\text{Fe}_{66.5}\text{Cr}_7\text{Nb}_3\text{Cu}_1\text{Si}_{13.5}\text{B}_9$ at the heating rate of $50^\circ\text{C}/\text{min}$

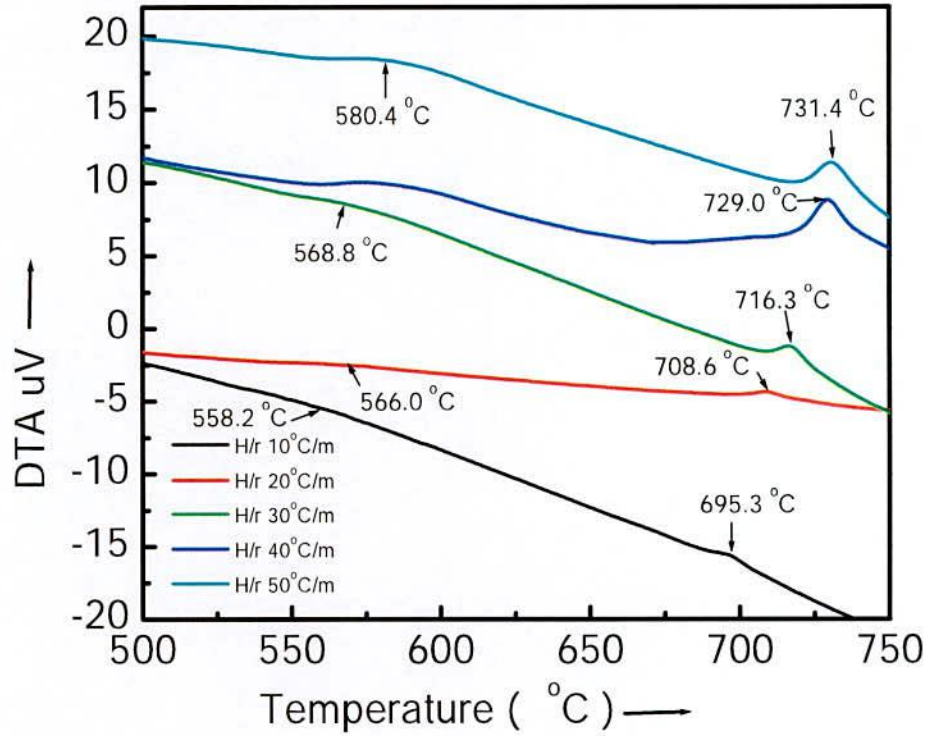


Fig. 5.3 Effects of heating rate on DTA traces of nanocrystalline amorphous ribbons $\text{Fe}_{66.5}\text{Cr}_7\text{Nb}_3\text{Cu}_1\text{Si}_{13.5}\text{B}_9$ at the heating rate of 10°C to $50^\circ\text{C}/\text{min}$

From Fig. 5.3 represents a combination of all DTA traces of amorphous $\text{Fe}_{66.5}\text{Cr}_7\text{Nb}_3\text{Cu}_1\text{Si}_{13.5}\text{B}_9$ ribbons. It is observed that the crystallization of each phase has occurred over a wide range temperatures and that the peak temperatures shift to higher values with the increase of heating rate. That means, it is required more heat energy for the formation of crystalline phases with increasing heating rates.

From each of the DTA traces, it is obvious that the area under the first crystallization peak is larger than the area covered by the second crystallization peak. In the Table 5.2 crystallization peak temperatures of two phases (T_{p1} and T_{p2}) and crystallization onset temperatures of two phases (T_{x1} and T_{x2}) are given for different heating rates.

Table 5.2 Effect of heating rate on 1st and 2nd crystallization states of the nanocrystalline amorphous ribbon with composition $\text{Fe}_{66.5}\text{Cr}_7\text{Nb}_3\text{Cu}_1\text{Si}_{13.5}\text{B}_9$

Heating rate β °C/min	1 st starting T_{x_1} °C	1 st Peak T_{p_1} °C	Temperature range of 1 st state in °C	2 nd starting T_{x_2} °C	2 nd Peak T_{p_2} °C	Temperature range of 2 nd state in °C	$T_{x_2} - T_{x_1}$ In °C	$T_{p_2} - T_{p_1}$ In °C
10	534.2	558.2	24.0	686.6	695.3	08.7	152.4	137.1
20	539.4	566.0	26.6	694.4	708.6	14.2	155.0	142.6
30	548.2	568.8	20.6	703.9	716.3	12.4	155.7	147.5
40	554.9	578.6	23.7	711.6	729.0	17.4	156.7	150.4
50	559.8	580.4	20.6	717.6	731.4	13.8	157.8	151.0

It has been observed that the crystallization temperature range of first phase occurred within 20.6°C to 26.6°C but this range for the second crystallization phase is 8.7°C to 17.4°C. So it is notable that the crystallization temperature range for first peak is always larger than the second peak. It is also observed that the peak temperature shift to higher values and crystallization temperature range increases with the heating rates.

The activation energy of crystallization of T_{x_1} and T_{x_2} phases have been calculated using Kissinger equation [5.8].

$$\beta = T_p^2 e^{-E/KT_p}$$

$$\ln\left(\frac{\beta}{T_p^2}\right) = -\frac{E}{KT_p}$$

$$E = -KT_p \ln\left(\frac{\beta}{T_p^2}\right) \quad (5.1)$$

Where β is the heating rate, T_p is the crystallization temperature, E is the activation energy and K is the Boltzmann constant. The activation energy of T_{x_1} [α -Fe(Si)] and T_{x_2} [Fe_2B] phases has been calculated from table 5.3 and using Kissinger's plot shown in Fig. 5.4 (a) and Fig.5.4 (b). It shows that first thermal crystallization activation energy of α -Fe(Si) phase E_1 is 3.98 eV and second Fe_2B phase E_2 is 3.33 eV.

Table 5.3 Effect of heating rate on 1st and 2nd crystallization of the nanocrystalline amorphous ribbon with composition $\text{Fe}_{66.5}\text{Cr}_7\text{Nb}_3\text{Cu}_1\text{Si}_{13.5}\text{B}_9$ state's calculative data for activation energy calculation data

Heating rate β °C/min	Heating rate β K/min	1 st Peak T_{p1} °K	$\frac{1}{T_{p1}} \times 10^3$	$\ln(\beta/T_{p1}^2)$	2 nd Peak T_{p2} °K	$\frac{1}{T_{p2}} \times 10^3$	$\ln(\beta/T_{p2}^2)$
10	13.41	831.35	1.203	-10.85	968.45	1.033	-11.16
20	26.89	839.15	1.192	-10.17	981.75	1.019	-10.49
30	40.24	841.95	1.188	-9.78	989.45	1.011	-10.09
40	53.66	851.75	1.174	-9.51	1002.15	0.998	-9.84
50	67.07	853.55	1.172	-9.29	1004.55	0.995	-9.61

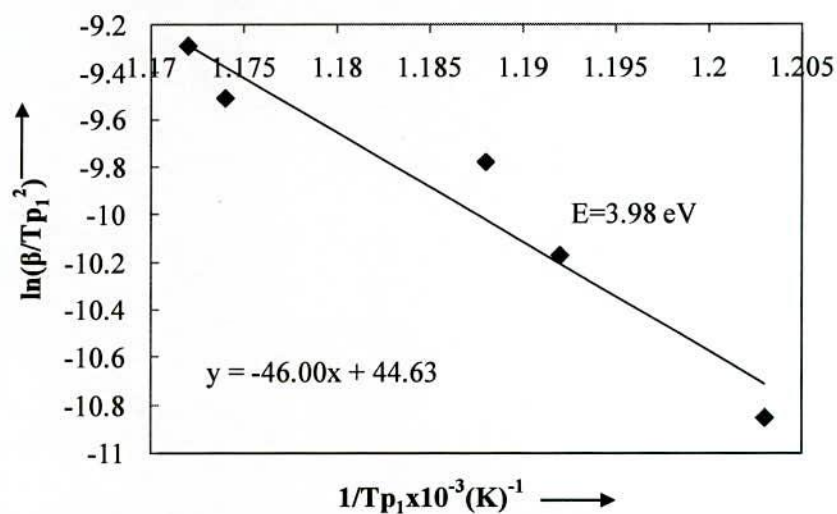


Fig. 5.4 (a) Kissinger's plot to determine the activation of Fe(Si) phase for $\text{Fe}_{66.5}\text{Cr}_7\text{Nb}_3\text{Cu}_1\text{Si}_{13.5}\text{B}_9$ alloy

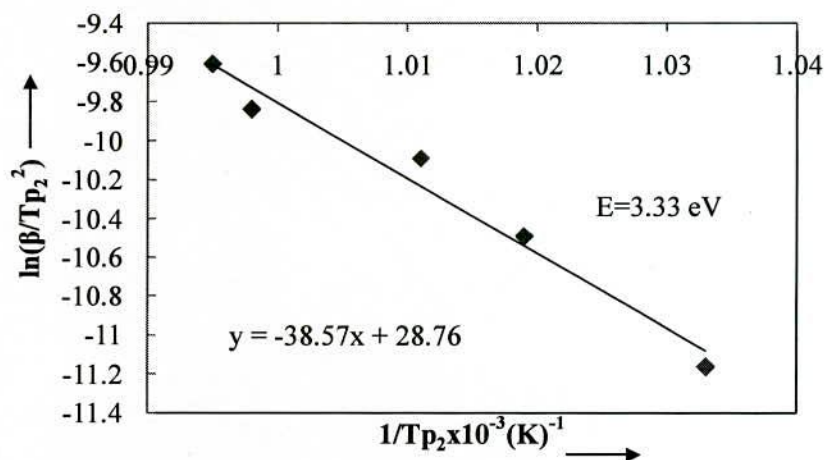


Fig. 5.4 (b) Kissinger's plot to determine the activation of Fe_2B phase for $\text{Fe}_{66.5}\text{Cr}_7\text{Nb}_3\text{Cu}_1\text{Si}_{13.5}\text{B}_9$ alloy

5.2.2 Study of DTA Traces of $\text{Fe}_{64.5}\text{Cr}_9\text{Nb}_3\text{Cu}_1\text{Si}_{13.5}\text{B}_9$ Alloy

DTA traces of as-cast nanocrystalline amorphous ribbon $\text{Fe}_{64.5}\text{Cr}_9\text{Nb}_3\text{Cu}_1\text{Si}_{13.5}\text{B}_9$ alloy taken in the nitrogen atmosphere with the heating rates of $10^\circ\text{C} - 50^\circ\text{C}/\text{minute}$ at the step of 10°C with continuous heating from room temperature to 800°C , are presented in Fig. 5.5(a) to Fig. 5.5(e) respectively. In each of the figures, two exothermic peaks are observed which correspond to two different crystallization events at temperature T_{x1} and T_{x2} respectively. The first one corresponds to the crystallization of $\alpha\text{-Fe (Si)}$ phase and the second one is related to the crystallization of Fe_2B .

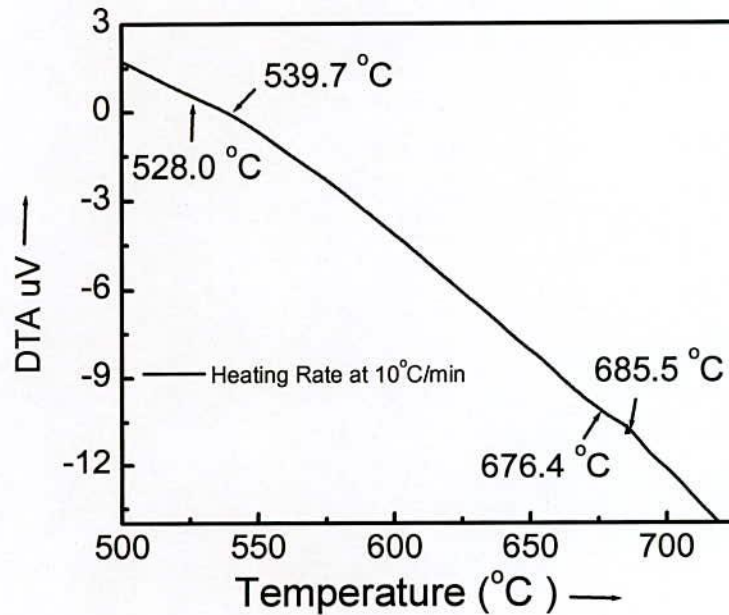


Fig. 5.5 (a) DTA trace of as-cast nanocrystalline amorphous ribbon $\text{Fe}_{64.5}\text{Cr}_9\text{Nb}_3\text{Cu}_1\text{Si}_{13.5}\text{B}_9$ at the heating rate of $10^\circ\text{C}/\text{min}$

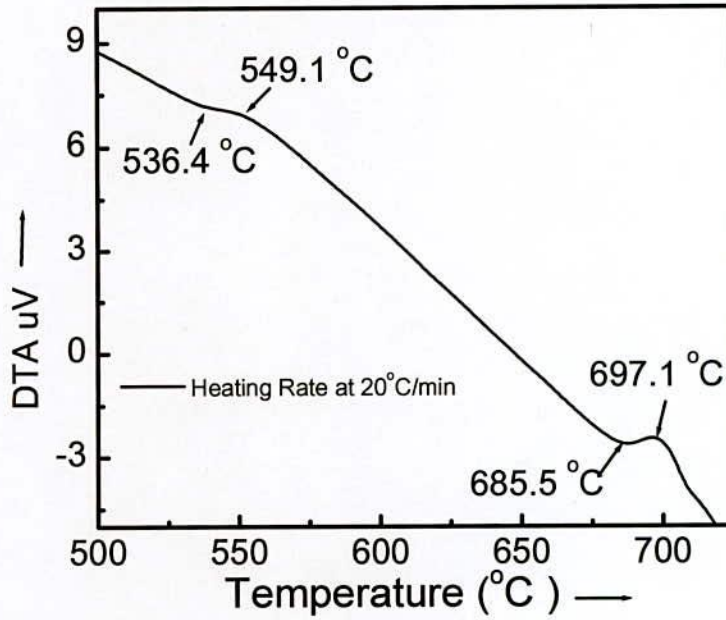


Fig. 5.5 (b) DTA trace of as-cast nanocrystalline amorphous ribbon $\text{Fe}_{64.5}\text{Cr}_9\text{Nb}_3\text{Cu}_1\text{Si}_{13.5}\text{B}_9$ at the heating rate of $20^\circ\text{C}/\text{min}$

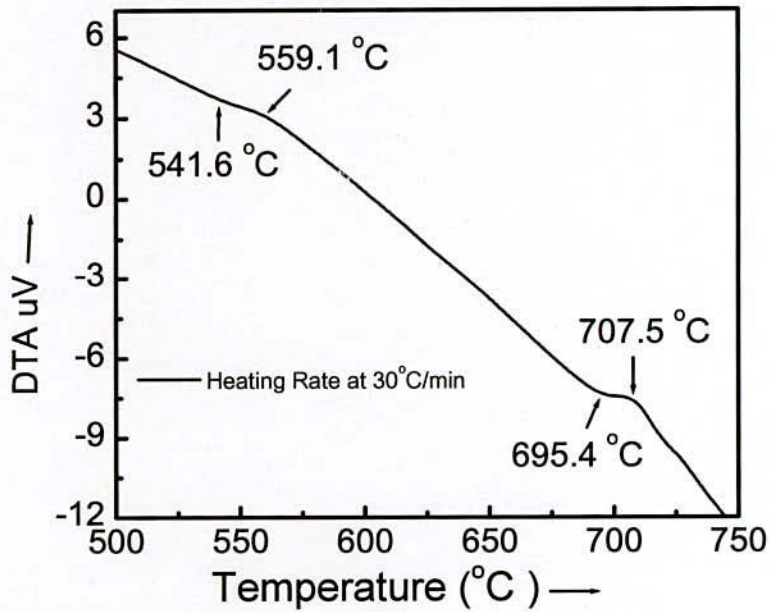


Fig. 5.5 (c) DTA trace of as-cast nanocrystalline amorphous ribbon $\text{Fe}_{64.5}\text{Cr}_9\text{Nb}_3\text{Cu}_1\text{Si}_{13.5}\text{B}_9$ at the heating rate of $30^\circ\text{C}/\text{min}$

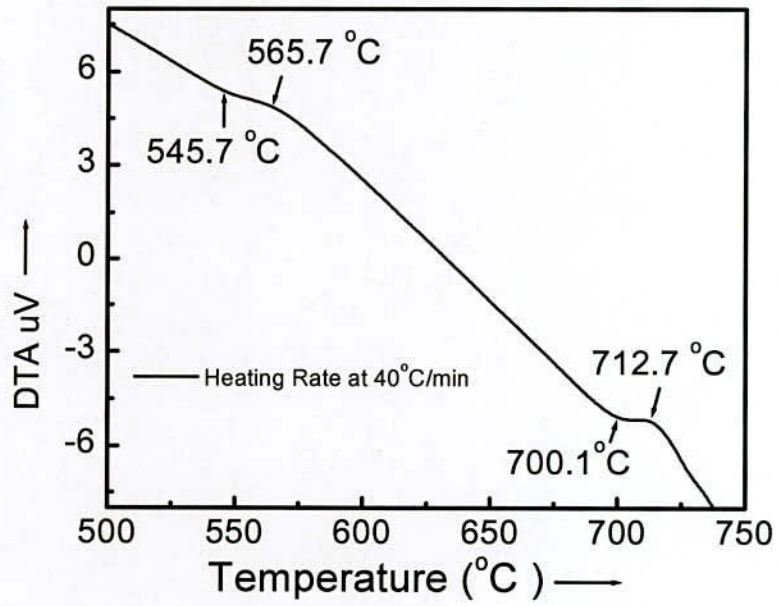


Fig. 5.5 (d) DTA trace of as-cast nanocrystalline amorphous ribbon $\text{Fe}_{64.5}\text{Cr}_9\text{Nb}_3\text{Cu}_1\text{Si}_{13.5}\text{B}_9$ at the heating rate of $40^\circ\text{C}/\text{min}$

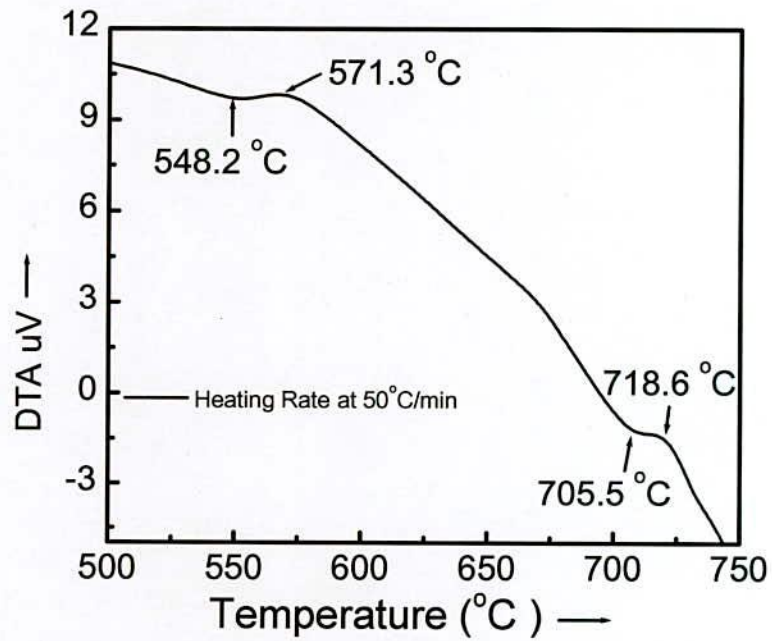


Fig. 5.5 (e) DTA trace of as-cast nanocrystalline amorphous ribbon $\text{Fe}_{64.5}\text{Cr}_9\text{Nb}_3\text{Cu}_1\text{Si}_{13.5}\text{B}_9$ at the heating rate of $50^\circ\text{C}/\text{min}$

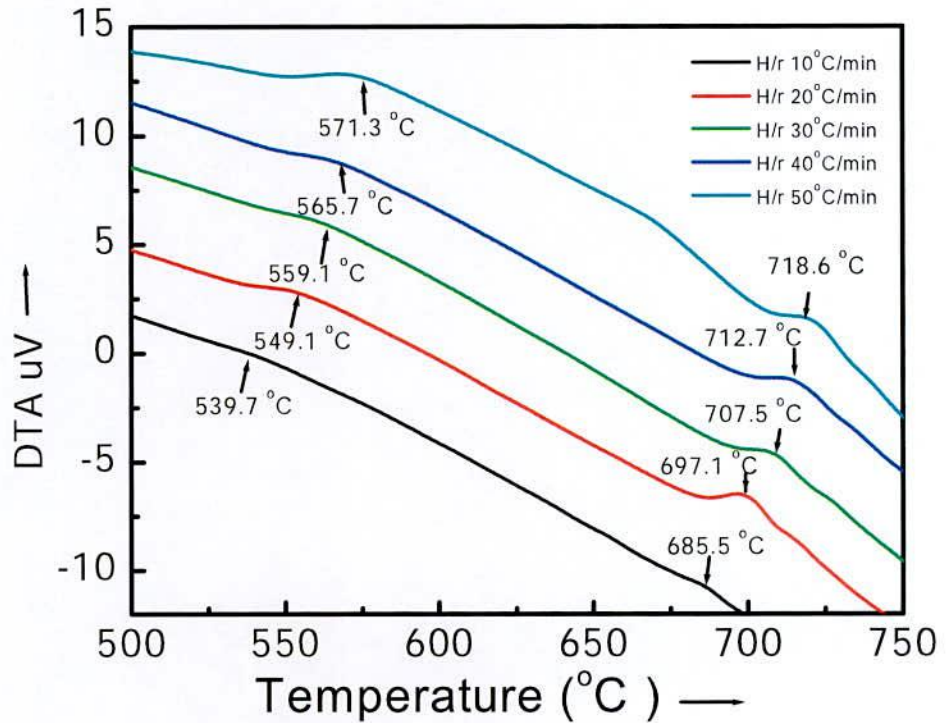


Fig. 5.6 Effects of heating rate on DTA traces of nanocrystalline amorphous ribbon with composition $\text{Fe}_{64.5}\text{Cr}_9\text{Nb}_3\text{Cu}_1\text{Si}_{13.5}\text{B}_9$ at the heating rate of 10°C to $50^\circ\text{C}/\text{min}$

From Fig. 5.6 represents a combination of all DTA traces of amorphous $\text{Fe}_{64.5}\text{Cr}_9\text{Nb}_3\text{Cu}_1\text{Si}_{13.5}\text{B}_9$ ribbons. From each of the DTA traces, it is obvious that the area under the first crystallization peak is larger than the area covered by the second crystallization peak. In the Table 5.4 crystallization peak temperatures of two phases (T_{p1} and T_{p2}) and crystallization onset temperatures of two phases (T_{x1} and T_{x2}) are given for different heating rates.

Table 5.4 Effect of heating rate on 1st and 2nd crystallization states of the nanocrystalline amorphous ribbon with composition $\text{Fe}_{64.5}\text{Cr}_9\text{Nb}_3\text{Cu}_1\text{Si}_{13.5}\text{B}_9$

Heating rate $\beta^\circ\text{C}/\text{min}$	1 st starting $T_{x1}^\circ\text{C}$	1 st Peak $T_{p1}^\circ\text{C}$	Temperature range of 1 st state in $^\circ\text{C}$	2 nd starting $T_{x2}^\circ\text{C}$	2 nd Peak $T_{p2}^\circ\text{C}$	Temperature range of 2 nd state in $^\circ\text{C}$	$T_{x2}-$ T_{x1} In $^\circ\text{C}$	$T_{p2}-T_{p1}$ In $^\circ\text{C}$
10	528.0	539.7	11.7	676.4	685.5	9.1	148.4	145.8
20	536.4	549.1	12.7	685.5	697.1	11.6	149.1	148
30	541.6	559.1	17.5	695.4	707.5	12.1	153.8	148.4
40	545.7	565.7	20	700.1	712.7	12.6	154.4	147
50	548.2	571.3	23.1	705.5	718.6	13.1	157.3	147.3

It has been observed that the crystallization temperature range of first phase occurred within 11.7°C to 23.1°C but this range for the second crystallization phase is 9.1°C to 13.1°C. So it is notable that the crystallization temperature range for first peak is always larger than the second peak. It is also observed that the peak temperature shift to higher values and crystallization temperature range increase with the heating rates.

Table 5.5 Effect of heating rate on 1st and 2nd crystallization of the nanocrystalline amorphous ribbon with composition $\text{Fe}_{64.5}\text{Cr}_9\text{Nb}_3\text{Cu}_1\text{Si}_{13.5}\text{B}_9$ state's calculative data for activation energy calculation data.

Heating rate $\beta^\circ\text{C}/\text{min}$	Heating rate $\beta^\circ\text{K}/\text{min}$	1 st Peak $T_{p1}^\circ\text{K}$	$\frac{1}{T_{p1}} \times 10^3$	$\ln(\beta/T_{p1}^2)$	2 nd Peak $T_{p2}^\circ\text{K}$	$\frac{1}{T_{p2}} \times 10^3$	$\ln(\beta/T_{p2}^2)$
10	13.41	812.85	1.230	-10.81	958.65	1.043	-11.14
20	26.89	822.25	1.216	-10.13	970.25	1.031	-10.46
30	40.24	832.25	1.202	-9.75	980.65	1.020	-10.08
40	53.66	838.85	1.192	-9.48	985.85	1.014	-9.80
50	67.07	844.45	1.184	-9.27	991.75	1.008	-9.59

The activation energy of $T_{x1}[\alpha\text{-Fe}(\text{Si})]$ and $T_{x2}[\text{Fe}_2\text{B}]$ phases has been calculated from table 5.5 and using Kissinger's plot shown in Fig. 5.7 (a) and Fig. 5.7 (b). It shows that first thermal crystallization activation energy of $\alpha\text{-Fe}(\text{Si})$ phase E_1 is 2.81 eV and second Fe_2B phase E_2 is 3.76 eV.

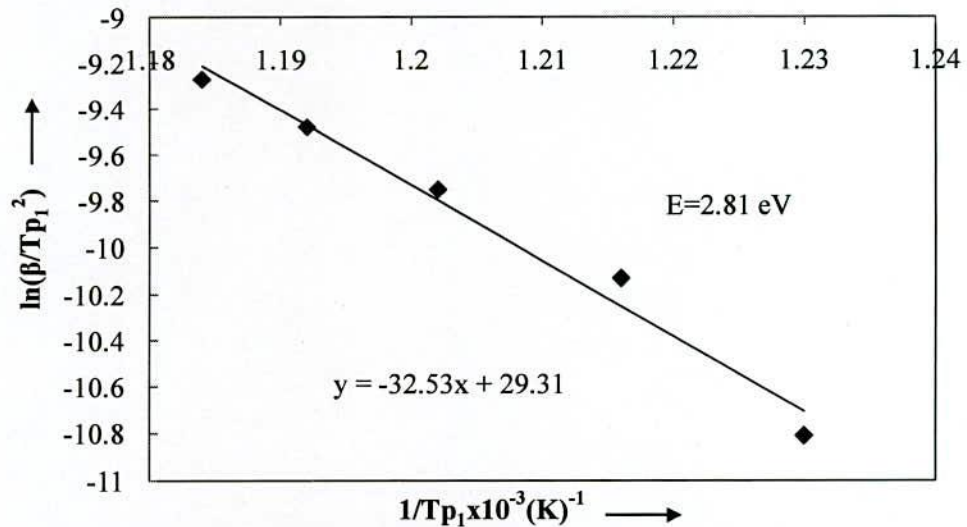


Fig. 5.7 (a) Kissinger's plot to determine the activation of Fe(Si) phase for $\text{Fe}_{64.5}\text{Cr}_9\text{Nb}_3\text{Cu}_1\text{Si}_{13.5}\text{B}_9$ alloy

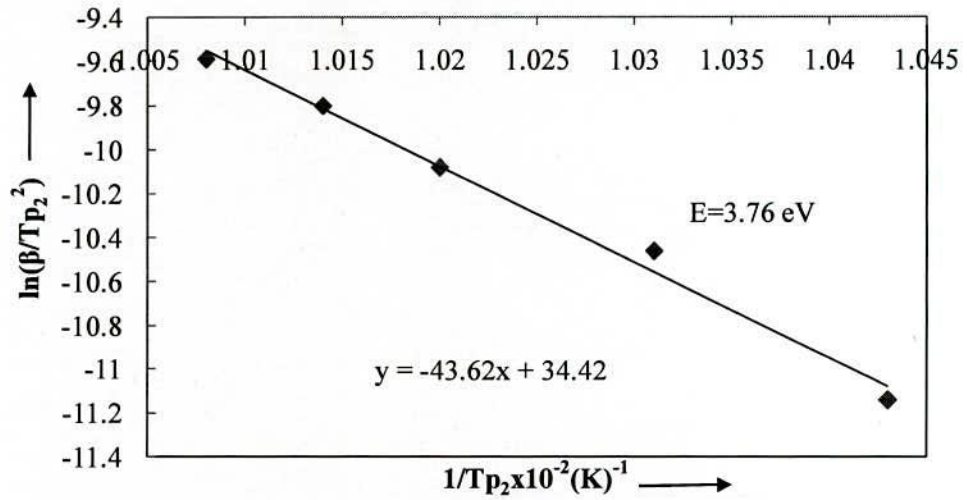


Fig. 5.7 (b) Kissinger's plot to determine the activation of Fe₂B phase for Fe_{64.5}Cr₉Nb₃Cu₁Si_{13.5}B₉ alloy

5.2.3 Study of DTA traces of Fe_{63.5}Cr₁₀Nb₃Cu₁Si_{13.5}B₉ Alloy

DTA traces of as-cast nanocrystalline amorphous ribbon Fe_{63.5}Cr₁₀Nb₃Cu₁Si_{13.5}B₉ alloy taken in the Nitrogen atmosphere with the heating rates of 10°C - 50°C/minute at the step of 10°C with continuous heating from room temperature to 800°C, are presented in Fig. 5.8 (a) to Fig. 5.8 (e) respectively. Two exothermic peaks are observed which corresponds to two different crystallization events at temperature T_{x1} and T_{x2} respectively. The first one corresponds to the crystallization of α -Fe(Si) phase and the second one is related to the crystallization of Fe₂B.

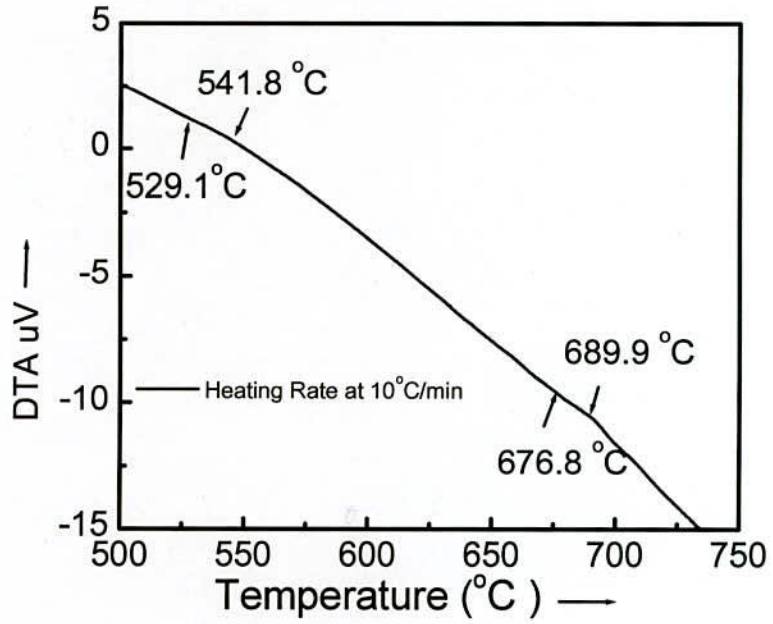


Fig. 5.8 (a) DTA trace of as-cast nanocrystalline amorphous ribbon $\text{Fe}_{63.5}\text{Cr}_{10}\text{Nb}_3\text{Cu}_1\text{Si}_{13.5}\text{B}_9$ at the heating rate of 10 $^{\circ}\text{C}/\text{min}$

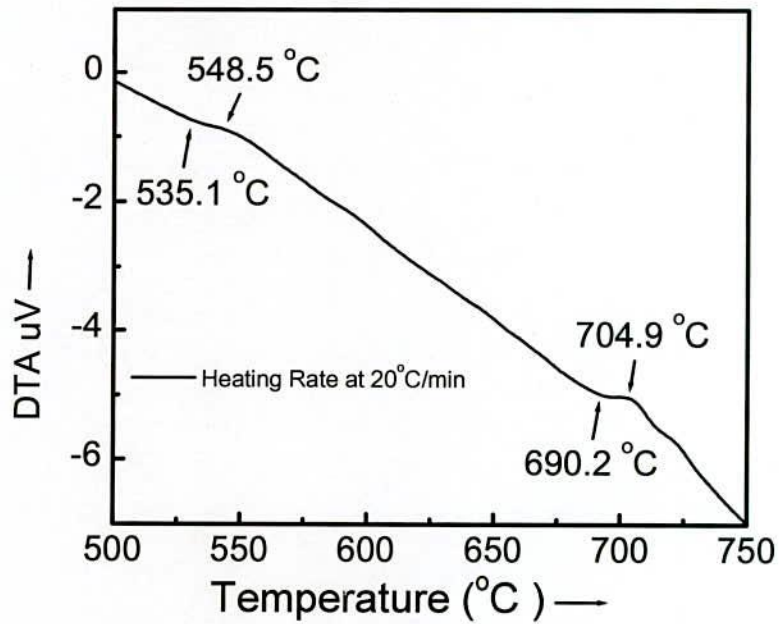


Fig. 5.8 (b) DTA trace of as-cast nanocrystalline amorphous ribbon $\text{Fe}_{63.5}\text{Cr}_{10}\text{Nb}_3\text{Cu}_1\text{Si}_{13.5}\text{B}_9$ at the heating rate of 20 $^{\circ}\text{C}/\text{min}$

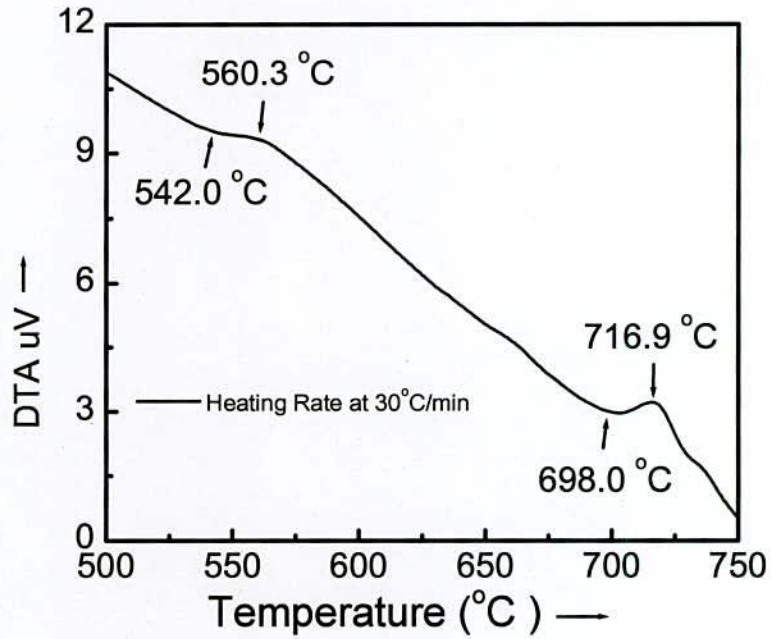


Fig. 5.8 (c) DTA trace of as-cast nanocrystalline amorphous ribbon $\text{Fe}_{63.5}\text{Cr}_{10}\text{Nb}_3\text{Cu}_1\text{Si}_{13.5}\text{B}_9$ at the heating rate of $30^\circ\text{C}/\text{min}$

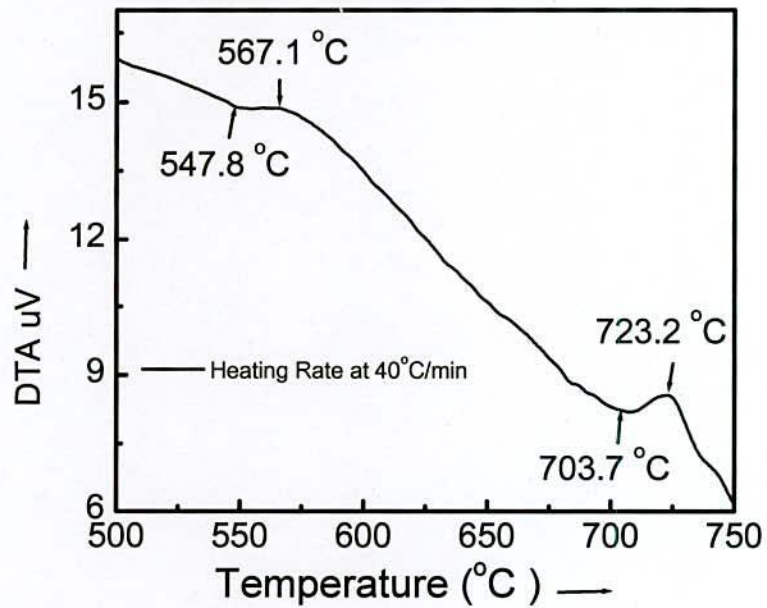


Fig. 5.8 (d) DTA trace of as-cast nanocrystalline amorphous ribbon $\text{Fe}_{63.5}\text{Cr}_{10}\text{Nb}_3\text{Cu}_1\text{Si}_{13.5}\text{B}_9$ at the heating rate of $40^\circ\text{C}/\text{min}$

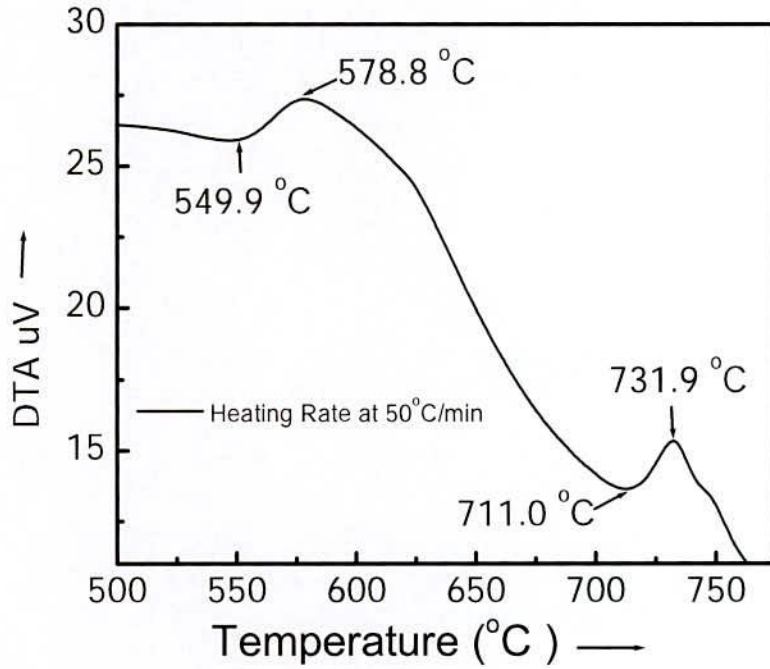


Fig. 5.8 (e) DTA trace of as-cast nanocrystalline amorphous ribbon $\text{Fe}_{63.5}\text{Cr}_{10}\text{Nb}_3\text{Cu}_1\text{Si}_{13.5}\text{B}_9$ at the heating rate of $50^\circ\text{C}/\text{min}$

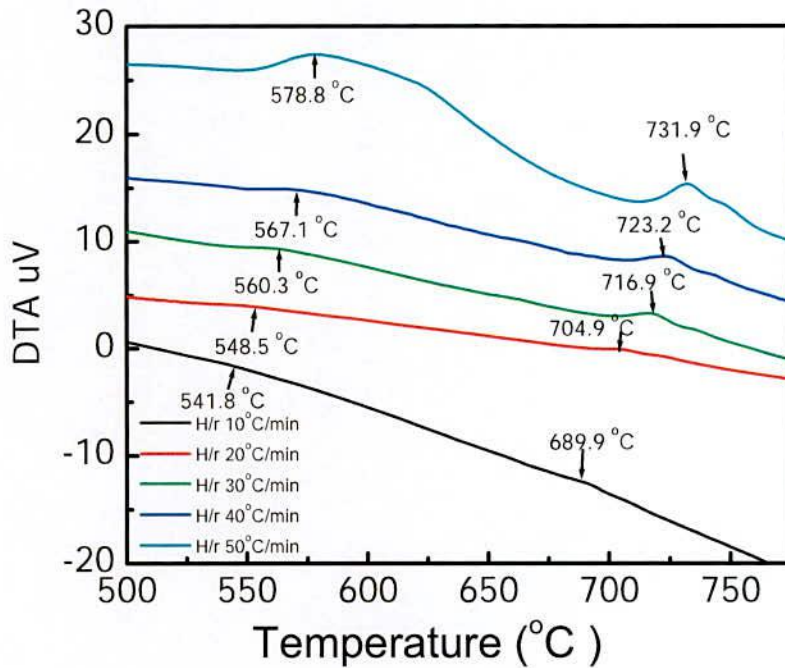


Fig. 5.9 Effects of heating rate on DTA traces of nanocrystalline amorphous ribbon with composition $\text{Fe}_{63.5}\text{Cr}_{10}\text{Nb}_3\text{Cu}_1\text{Si}_{13.5}\text{B}_9$ at the heating rate of 10°C to $50^\circ\text{C}/\text{min}$

From Fig. 5.9 represents a combination of all DTA traces of amorphous $\text{Fe}_{63.5}\text{Cr}_{10}\text{Nb}_3\text{Cu}_1\text{Si}_{13.5}\text{B}_9$ ribbon alloy. It is observed that the crystallization of each phase has occurred over a wide range temperature and that the peak temperatures shift to higher values with the increase of heating rate. That means it requires more energy for the formation of crystalline phases with increasing heating rates. Table 5.6 crystallization peak temperatures of two phases (T_{p1} and T_{p2}) and crystallization starting temperatures of two phases (T_{x1} and T_{x2}) are given for different heating rates.

Table 5.6 Effect of heating rate on 1st and 2nd crystallization states of the nanocrystalline amorphous ribbon with composition $\text{Fe}_{63.5}\text{Cr}_{10}\text{Nb}_3\text{Cu}_1\text{Si}_{13.5}\text{B}_9$

Heating rate β °C/min	1 st starting T_{x1} °C	1 st Peak T_{p1} °C	Temperature range of 1 st state in °C	2 nd starting T_{x2} °C	2 nd Peak T_{p2} °C	Temperature range of 2 nd state in °C	$T_{x2} - T_{x1}$ In °C	$T_{p2} - T_{p1}$ In °C
10	529.1	541.8	12.7	676.8	689.9	13.1	147.7	148.1
20	535.1	548.5	13.4	690.2	704.9	14.7	155.1	156.4
30	542.0	560.3	18.3	698.0	716.9	18.9	156.0	156.6
40	547.8	567.1	19.3	703.7	723.2	19.5	151.2	152.8
50	549.9	578.8	28.9	711.0	731.9	20.9	161.1	153.1

It has been observed that the crystallization temperature range of first phase occurred within 16.8°C to 30.8°C but the range for second crystallization phase is 9.3°C to 25.6°C. So it is notable that the crystallization temperature range for first peak is always larger than the second peak.

Table 5.7 Effect of heating rate on 1st and 2nd crystallization of the nanocrystalline amorphous ribbon with composition $\text{Fe}_{63.5}\text{Cr}_{10}\text{Nb}_3\text{Cu}_1\text{Si}_{13.5}\text{B}_9$ for activation energy calculation data

Heating rate β °C/min	Heating rate β °K/min	1 st Peak T_{p1} °K	$\frac{1}{T_{p1}} \times 10^3$	$\ln(\frac{\beta}{T_{p1}^2})$	2 nd Peak T_{p2} °K	$\frac{1}{T_{p2}} \times 10^3$	$\ln(\frac{\beta}{T_{p2}^2})$
10	13.41	814.95	1.227	-10.81	963.05	1.035	-11.14
20	26.89	821.65	1.217	-10.13	978.05	1.022	-10.48
30	40.24	833.45	1.199	-9.76	990.05	1.010	-10.10
40	53.66	840.25	1.190	-9.48	996.35	1.004	-9.83
50	67.07	851.95	1.174	-9.29	1005.05	0.995	-9.62

The activation energy of $T_{x_1}[\alpha\text{-Fe (Si)}]$ and $T_{x_2}[\text{Fe}_2\text{B}]$ phases have been calculated from Table 5.7 and using Kissinger's plot shown in Fig. 5.10 (a) and Fig. 5.10 (b). It shows that first thermal crystallization activation energy of $\alpha\text{-Fe(Si)}$ phase E_1 is 2.35 eV and second Fe_2B phase E_2 is 3.28 eV.

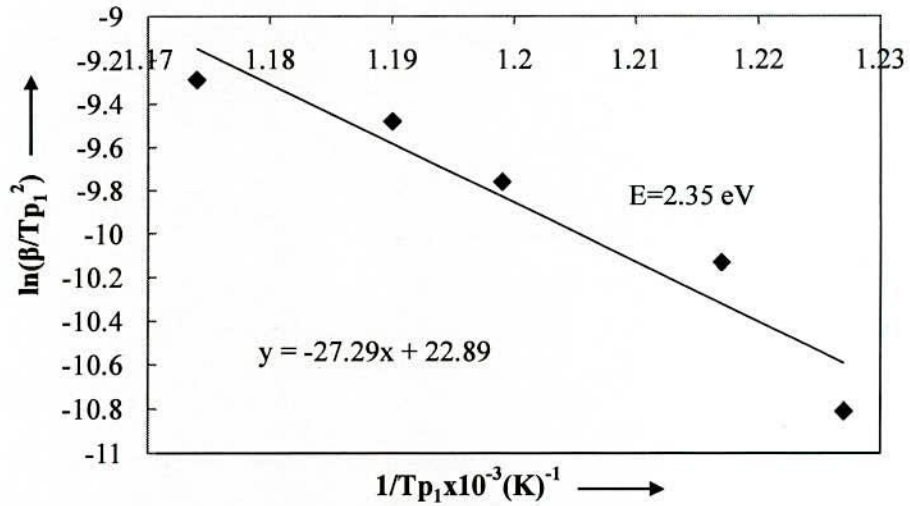


Fig. 5.10 (a) Kissinger's plot to determine the activation of Fe(Si) phase for $\text{Fe}_{63.5}\text{Cr}_{10}\text{Nb}_3\text{Cu}_1\text{Si}_{13.5}\text{B}_9$ alloy

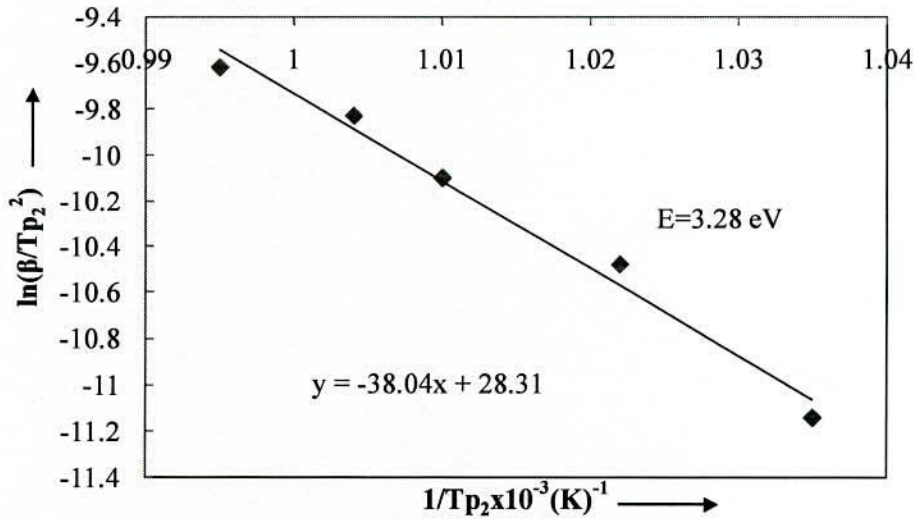


Fig. 5.10 (b) Kissinger's plot to determine the activation of Fe_2B phase for $\text{Fe}_{63.5}\text{Cr}_{10}\text{Nb}_3\text{Cu}_1\text{Si}_{13.5}\text{B}_9$ alloy

5.2.4 Study of DTA traces of $\text{Fe}_{61}\text{Cr}_{12.5}\text{Nb}_3\text{Cu}_1\text{Si}_{13.5}\text{B}_9$ Alloy

DTA traces of as-cast nanocrystalline amorphous ribbon $\text{Fe}_{61}\text{Cr}_{12.5}\text{Nb}_3\text{Cu}_1\text{Si}_{13.5}\text{B}_9$ alloy taken in the nitrogen atmosphere with the heating rates of $10^\circ\text{C} - 50^\circ\text{C}/\text{minute}$ at the step of 10°C with continuous heating from room temperature to 800°C , are presented in Fig. 5.11 (a) to Fig. 5.11 (e) respectively. Two exothermic peaks are observed which corresponds to two different crystallization events at temperature T_{x_1} and T_{x_2} respectively. The first one corresponds to the crystallization of $\alpha\text{-Fe}(\text{Si})$ phase and the second one is related to the crystallization of Fe_2B .

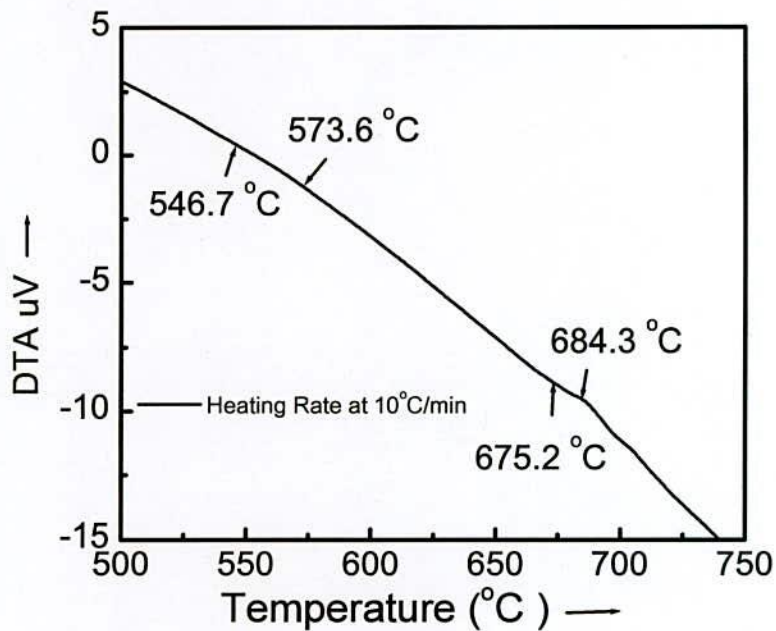


Fig. 5.11 (a) DTA trace of as-cast nanocrystalline amorphous ribbon $\text{Fe}_{61}\text{Cr}_{12.5}\text{Nb}_3\text{Cu}_1\text{Si}_{13.5}\text{B}_9$ at the heating rate of $10^\circ\text{C}/\text{min}$

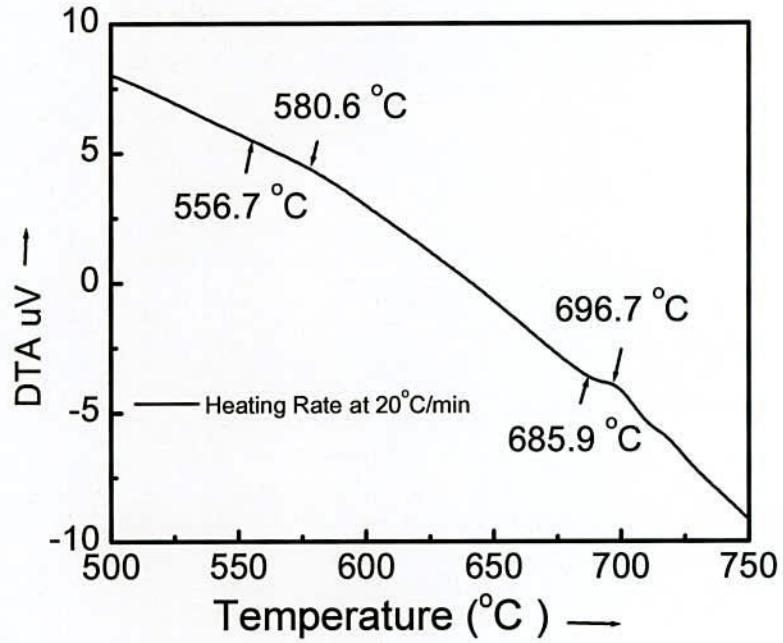


Fig. 5.11(b) DTA trace of as-cast nanocrystalline amorphous ribbon $\text{Fe}_{61}\text{Cr}_{12.5}\text{Nb}_3\text{Cu}_1\text{Si}_{13.5}\text{B}_9$ at the heating rate of $10^\circ\text{C}/\text{min}$

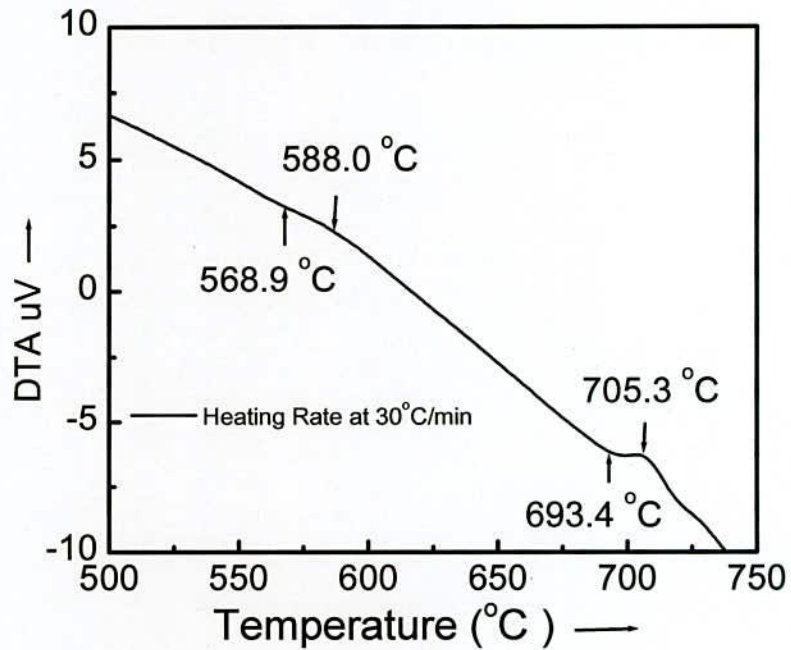


Fig. 5.11(c) DTA trace of as-cast nanocrystalline amorphous ribbon $\text{Fe}_{61}\text{Cr}_{12.5}\text{Nb}_3\text{Cu}_1\text{Si}_{13.5}\text{B}_9$ at the heating rate of $10^\circ\text{C}/\text{min}$

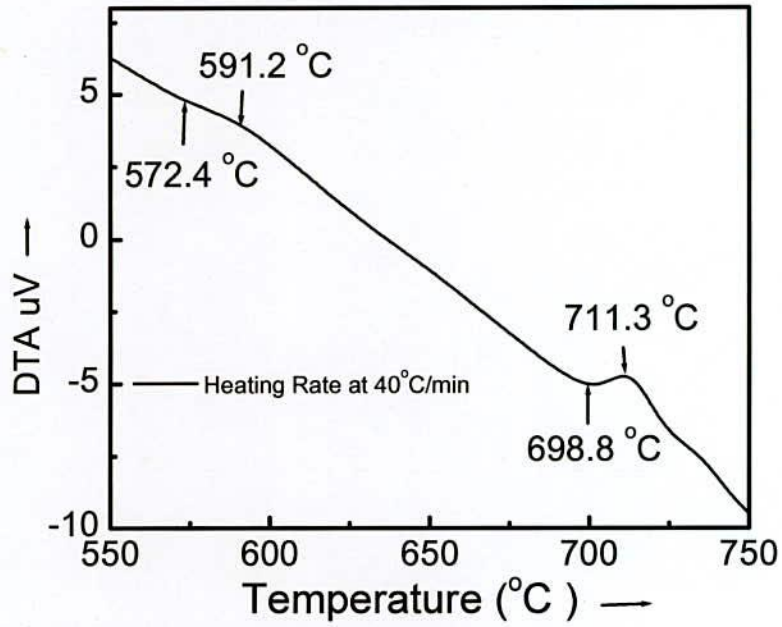


Fig. 5.11(d) DTA trace of as-cast nanocrystalline amorphous ribbon $\text{Fe}_{61}\text{Cr}_{12.5}\text{Nb}_3\text{Cu}_1\text{Si}_{13.5}\text{B}_9$ at the heating rate of $10^\circ\text{C}/\text{min}$

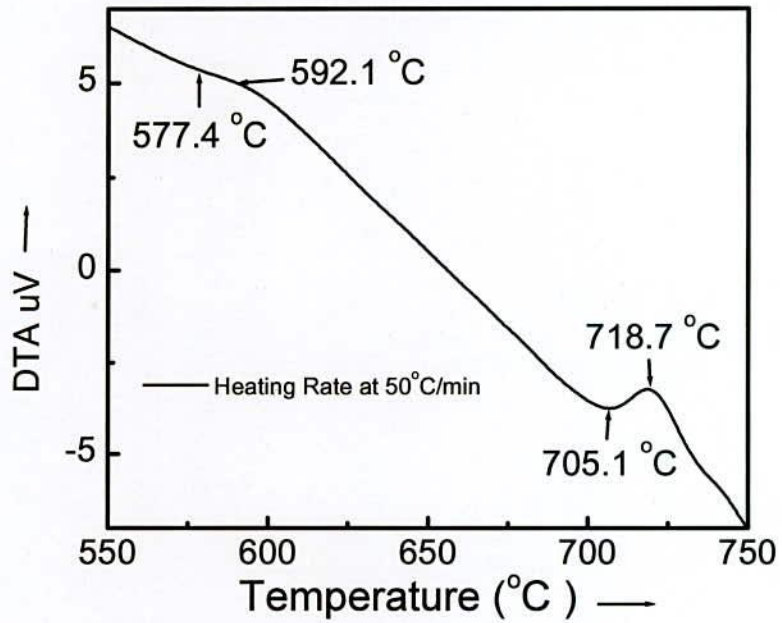


Fig. 5.11(e) DTA trace of as-cast nanocrystalline amorphous ribbon $\text{Fe}_{61}\text{Cr}_{12.5}\text{Nb}_3\text{Cu}_1\text{Si}_{13.5}\text{B}_9$ at the heating rate of $10^\circ\text{C}/\text{min}$

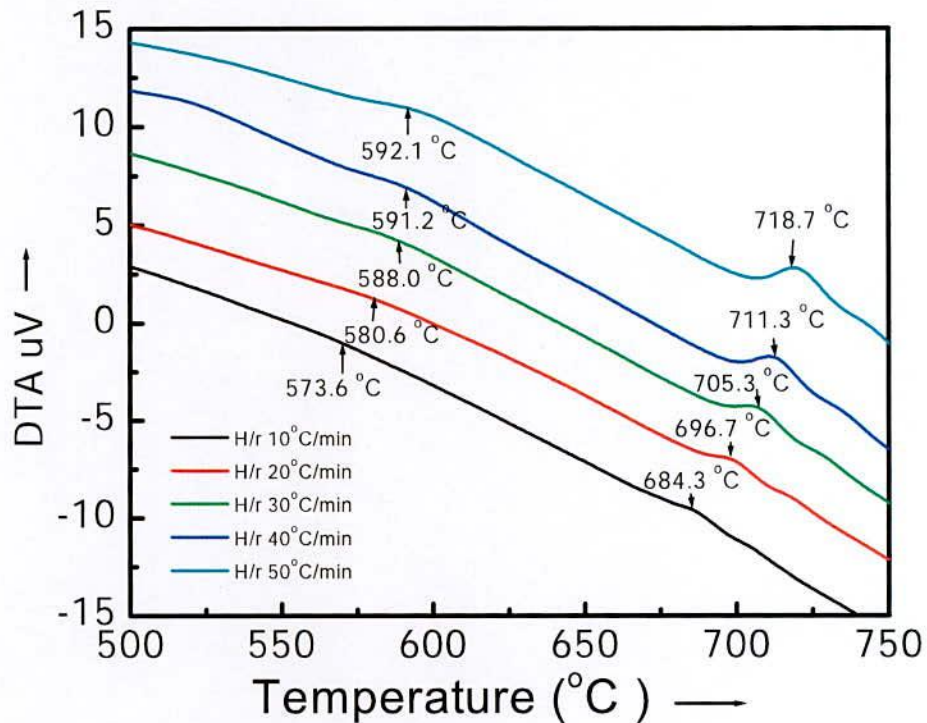


Fig. 5.12 Effects of heating rate on DTA traces of nanocrystalline amorphous Ribbons with composition $\text{Fe}_{61}\text{Cr}_{12.5}\text{Nb}_3\text{Cu}_1\text{Si}_{13.5}\text{B}_9$ at the heating rate of 10°C to $50^\circ\text{C}/\text{min}$

From Fig. 5.12 represents a combination of all DTA traces of amorphous $\text{Fe}_{61}\text{Cr}_{12.5}\text{Nb}_3\text{Cu}_1\text{Si}_{13.5}\text{B}_9$ ribbon alloy. In Table 5.8, crystallization peak temperatures of two phases (T_{p1} and T_{p2}) and crystallization starting temperatures of two phases (T_{x1} and T_{x2}) are given for different heating rates.

Table 5.8 Effect of heating rate on 1st and 2nd crystallization states of the nanocrystalline amorphous ribbon with composition $\text{Fe}_{61}\text{Cr}_{12.5}\text{Nb}_3\text{Cu}_1\text{Si}_{13.5}\text{B}_9$

Heating rate $\beta^\circ\text{C}/\text{min}$	1 st starting $T_{x1}^\circ\text{C}$	1 st Peak $T_{p1}^\circ\text{C}$	Temperature range of 1 st state in $^\circ\text{C}$	2 nd starting $T_{x2}^\circ\text{C}$	2 nd Peak $T_{p2}^\circ\text{C}$	Temperature range of 2 nd state in $^\circ\text{C}$	$T_{x2}-$ T_{x1} In $^\circ\text{C}$	$T_{p2}-$ T_{p1} In $^\circ\text{C}$
10	546.7	573.6	26.9	675.2	684.3	9.1	128.5	110.7
20	556.7	580.6	23.9	685.9	696.7	10.8	129.2	116.1
30	568.9	588.0	19.1	693.4	705.3	11.9	124.5	117.3
40	572.4	591.2	18.8	698.8	711.3	12.5	126.4	120.1
50	577.4	592.1	14.7	705.1	718.7	13.6	127.7	126.6

It has been observed that the crystallization temperature range of first phase occurred within 14.7°C to 26.9°C but the range for second crystallization phase is 9.1°C to 13.6°C. So it is notable that the crystallization temperature range for first peak is always larger than the second peak. It is also observed that the peak temperature shift to higher values and crystallization temperature range increase with the heating rates.

Table 5.9 Effect of heating rate on 1st and 2nd crystallization states of the nanocrystalline amorphous ribbon with composition Fe₆₁Cr_{12.5}Nb₃Cu₁Si_{13.5}B₉ for activation energy calculation data

Heating rate β °C/min	Heating rate β °K/min	1 st Peak T_{p1} °C	$\frac{1}{T_{p1}} \times 10^3$	$\ln(\frac{\beta}{T_{p1}^2})$	2 nd Peak T_{p2} °C	$\frac{1}{T_{p2}} \times 10^3$	$\ln(\frac{\beta}{T_{p2}^2})$
10	13.41	846.75	1.181	-10.89	957.45	1.044	-11.13
20	26.89	853.75	1.171	-10.21	969.85	1.031	-10.46
30	40.24	861.15	1.161	-9.82	978.45	1.022	-10.08
40	53.66	864.35	1.157	-9.54	984.45	1.016	-9.80
50	67.07	865.25	1.155	-9.32	991.85	1.008	-9.59

The activation energy of $T_{x1}[\alpha\text{-Fe}(\text{Si})]$ and $T_{x2}[\text{Fe}_2\text{B}]$ phases has been calculated from Table 5.9 and using Kissinger's plot shown in Fig. 5.13(a) and Fig.5.13(b). It shows that first thermal crystallization activation energy of $\alpha\text{-Fe}(\text{Si})$ phase E_1 is 4.88 eV and second Fe_2B phase E_2 is 3.75 eV.

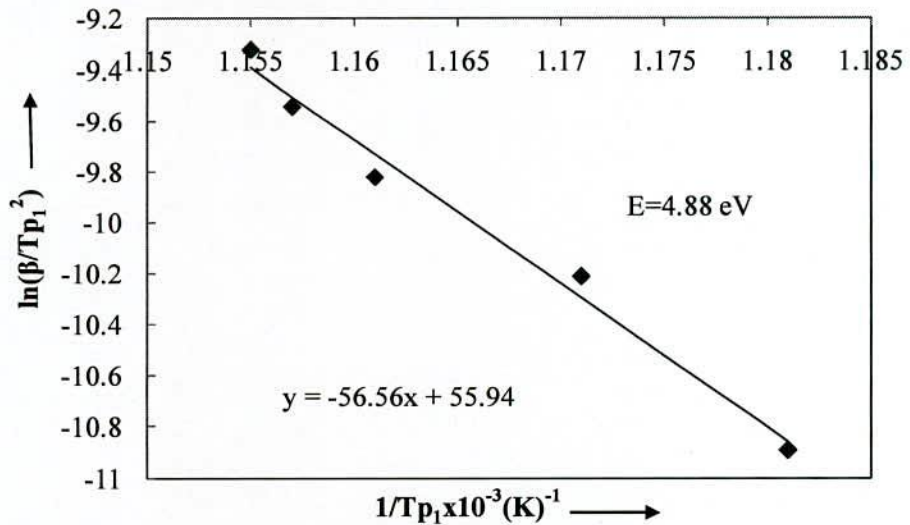


Fig. 5.13(a) Kissinger's plot to determine the activation of Fe(Si) phase for Fe₆₁Cr_{12.5}Nb₃Cu₁Si_{13.5}B₉ alloy

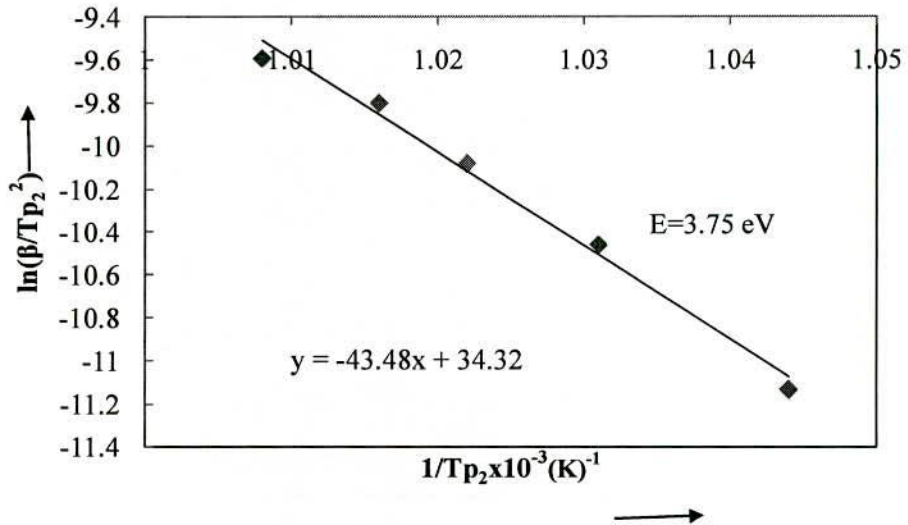


Fig. 5.13(b) Kissinger's plot to determine the activation of Fe_2B phase for $\text{Fe}_{61}\text{Cr}_{12.5}\text{Nb}_3\text{Cu}_1\text{Si}_{13.5}\text{B}_9$ alloy

5.3 Comparison between DTA of Fe-Cr-Cu-Nb-Si-B and original FINEMET

The comparative values of DTA results for present alloy and for original FINEMET sample are given in Table 5.10. The results show that the peak temperature corresponding to crystallization decreases with the increase of Cr substitution for Fe in the $\text{Fe}_{73.5-x}\text{Cr}_x\text{Nb}_3\text{Cu}_1\text{Si}_{13.5}\text{B}_9$ alloys. Table 5.2, Table 5.4 and Table 5.6 shows that the crystallization of each phase has occurred over a wide range of temperatures and the primary crystallization temperature shifts to higher temperature as the Cr-concentration increased. There is difference of $\approx 150 \pm 13^\circ\text{C}$ for the two crystallization temperature. But this difference decreases as the Cr-content is increased for $x = 12.5$, it is observed from Table 5.8. Table 5.10 shows the situation with the secondary crystallization temperature T_{x2} and T_{p2} with exception that for very high Cr content in which T_{x2} and T_{p2} slightly decreases toward the value corresponding to zero Cr content alloys. Primary crystallization T_{x1} in our experiment varies from 539°C for Cr = 7 at % to 557°C for Cr = 12.5 at %. This implies that higher Cr-content alloys weaken the diffusion process to form the crystallization phases since has a melting temperature (1857°C) higher than that of Fe (1536°C). From our experimental

findings it is clearly understood that the partial substitution of Fe by Cr enhance thermal stability of amorphous alloys against crystallization.

Table 5.10 crystallization states (heating rate 20°C/min) and activation energy of different phases of nanocrystalline amorphous ribbons with composition $Fe_{73.5-x}Cr_xNb_3Cu_1Si_{13.5}B_9$ [$x = 7, 9, 10$ & 12.5]

Cr-content	1 st starting T_{x_1} °C	1 st Peak T_{p_1} °C	2 nd starting T_{x_2} °C	2 nd Peak T_{p_2} °C	Activation energy of Fe(Si) phase E_1 in eV	Activation energy of Fe_2B phase E_2 in eV
x = 7	539.4	566.0	694.4	708.6	3.98	3.33
x = 9	536.4	549.1	685.5	697.1	2.81	3.76
x = 10	535.1	548.5	690.2	704.9	2.35	3.28
x = 12.5	556.7	580.6	685.9	696.7	4.88	3.75
x = 0 [5.8]	542	676	554	700	3.21	3.81

The opposite scenario has been observed when the substitution of Co for Fe in the FINEMET $Fe_{73.5-x}Co_xNb_3Cu_1Si_{13.5}B_9$ alloys is made [5.9]. The activation energy for formation of first crystalline Fe-Co(Si) phase is lower than that for the original FINEMET composition which is expected due to replacement of Co. Experimental observed when the substitution of Cr for Fe in the FINEMET $Fe_{73.5-x}Cr_xNb_3Cu_1Si_{13.5}B_9$ alloy. The crystallization peak temperature (T_{p_1}) and the activation energy for the primary crystallization E_1 decreases gradually increase with Cr-content but E_1 increase at Cr = 12.5 at % and given in Table 5.10. This result indicates that the role of Cr is to the formation of crystalline α -Fe(Si) phase. The crystallization activation energy for nucleation and growth increases. The formation of Cu-rich regions reduces the activation energy for nucleation E_1 of α -Fe(Si), so that the phase may nucleate and precipitate preferentially in the Cu-rich regions [5.10]. Secondary crystallization product Fe_2B are varies 3.28 to 3.76 eV. The understanding of the crystallization onset temperature is the crystallization peak temperature and the end of crystallization temperature for nanocrystallization. Temperature and time of annealing is crucial for controlling the size and volume fraction of nanocrystals, which ultimately controls the magnetic properties of the FINEMET of amorphous soft magnetic alloys. The amorphous state that maintains its amorphousity against annealing temperature is said to be stable, i.e. a sample with higher crystallization temperature is said to be stable.

5.4 Microstructural Analysis of Amorphous and Nanocrystalline

$\text{Fe}_{73.5-x}\text{Cr}_x\text{Nb}_3\text{Cu}_1\text{Si}_{13.5}\text{B}_9$ Alloy by XRD Analysis

X-ray diffraction (XRD) is generally used for the identification of various phases while the grain size is estimated by high-resolution transmission electron microscope (HRTEM) and / or by X-ray diffraction. XRD has been used to identify crystalline phase in nanocrystalline materials. Nanocrystalline alloys are above crystalline and because of their crystallinity they exhibit Bragg scattering peaks in XRD experiments. However, due to their small size, significant fine particle broadening is observed in the Bragg peaks. For 50nm particles, a broadening of 0.2° at half width the peak is expected which can easily be measured. Using Scherrer's formula of line broadening, particle size between 5 to 60nm can be measured using XRD.

In the present work, in order to study the crystallization onset temperature, XRD spectra have been recorded for the nominal composition $\text{Fe}_{73.5-x}\text{Cr}_x\text{Nb}_3\text{Cu}_1\text{Si}_{13.5}\text{B}_9$ [$x = 7, 9, 10 \text{ \& } 12.5$] annealed at 450° to 800° for 30 minutes. The approximately annealed samples were subjected to XRD by using a MTI Corporation built GSL-1600x40 tube furnace to examine the micro structural evaluation as a function of annealing temperature. From the experiment, four samples are annealed at different temperatures for 30 minute and every sample was taken under XRD analysis. From the output of XRD analysis three structural parameters such as calculated:

- (i) Lattice Parameter (a_0)
- (ii) Grain Size (D_g)
- (iii) Silicon Content (Si)

(i) Lattice Parameter Calculation

Lattice Parameter of crystalline bcc Fe-Si nanograin was determined at different annealing temperature of the experimental alloys. Structure of the α -Fe(Si) grains depends on the annealing temperature. Normally lattice Parameter of an alloy composition is determined by the Debye-Scherrer method after extrapolation of the diffraction curve for the sample. Generally for an accurate determination of the lattice parameter a number of fundamental peaks are required but in this type of tailored materials upon crystallization only major fundamental peaks (110) is used in

calculation of a_0 . We have, therefore, determined the lattice parameter using only that particular reflection using equation:

$$2d\sin\theta = n\lambda \text{ and } a_0 = d\sqrt{2} \quad (5.1)$$

Where $\lambda = 1.54053 \text{ \AA}$ is the wavelength of Cu- K_α radiation and a_0 is determined lattice parameter of the grain, d is the inter-planar spacing and θ is the diffraction angle.

(ii) Drain Size Determination

In 1963 Kneller and Luborsky [5.11] studied on nanograins. Found that the magnetic properties of isolated grains change drastically as their size is reduced to the nanometer range. When these nanometric grains are consolidated to form a nanostructured material, the magnetic properties are largely determined by the grain size and the exchange interaction between the adjacent grains. Herzer [5.12] successfully established the theoretical explanation on the grain size dependence of superior soft magnetic properties based on his Random Anisotropy Model (RAM) after the pioneer experimental invention of FINEMET alloy by Yoshizawa *et al.* [5.12]. One member of series FINEMET family is the sample $\text{Fe}_{73.5-x}\text{Cr}_x\text{Nb}_3\text{Cu}_1\text{Si}_{13.5}\text{B}_9$ [$x = 7, 9, 10 \text{ \& } 12.5$], which is under the investigation of the present work.

One of the most important aims of this study was to determine crystalline grain size for all the annealing temperatures. Grain size of all annealed samples of the alloy composition was determined using Scherrer method [5.13]. Grain size was determined from XRD pattern of (110) reflection for different annealing temperatures at constant annealing time 30 minutes from which grain size was determined using the formula

$$D_g = \frac{0.9\lambda}{\beta\cos\theta} \quad (5.2)$$

Where $\lambda = 1.54178 \text{ \AA}$ is the wavelength of Cu- K_α radiation, θ is the diffraction angle and β is the full width at half maximum (FWHM) of diffraction peak in radian for different steps of annealing temperature.

(iv) Si Content in Nanograins:

The major elements of the amorphous ribbon were Fe and Si with concentration of 61 to 66.5 at. % Fe and 13.5 at. % Si. Crystalline nanograins were formed on the ribbon in the process of annealing temperature with the alloy

composition of Fe-Si. It is therefore important to determine the concentration of Fe, Cr and Si in the nanograin. As lattice parameter of the nanograins have been measured for different heat treatment conditions, it is easy to calculate the Si content in the nanograin from the quantitative relationship between lattice parameter (a) and Si-content (Si at.%) developed by Bozorth [5.14]. It is easy to calculate the Si content in the nanograin from the Pearson hand book relationship [5.15]. From this relationship we have considered a simple equation to calculate Si-content from lattice parameter. This equation is

$$b = -467a_0 + 1342.8 \quad (5.3)$$

where b is at. % Si in the nanograins, a_0 is the lattice parameter of nanograins.

5.4.1 XRD Analysis of the Nanocrystalline Ribbon with Composition $\text{Fe}_{66.5}\text{Cr}_7\text{Nb}_3\text{Cu}_1\text{Si}_{13.5}\text{B}_9$

In the present work, structure of the $\text{Fe}_{66.5}\text{Cr}_7\text{Nb}_3\text{Cu}_1\text{Si}_{13.5}\text{B}_9$ nanocrystalline ribbon alloys annealed at temperature (T_a) from 450°C to 800°C for annealing time 30 minutes are investigated by the XRD method are presented in Fig. 5.14. It is evident from Fig. 5.14 when the sample annealed below 550°C i.e. at 550°C , it exhibit only one broad peak around $\theta = 45^\circ$ at the position of d_{110} reflection which is generally known as diffuse hallow. This diffuse hallow indicates the amorphous nature of the sample. It means at the annealing temperature below 550°C , no crystalline peak has been detected. Patterns of $T_a=550^\circ\text{C}$ indicates a clear bcc $\alpha - \text{Fe}(\text{Si})$ of said compositions after heat treatment for 30 minutes. The same pattern observed for all the samples at different annealing temperatures indicates the $\alpha - \text{Fe}(\text{Si})$ phase. The crystallization onset temperature from DTA experiments for different heating rates, were formed in the range of 400°C to 800°C , which shows a good consistency with the XRD results. The XRD pattern has taken for the samples annealed from 450°C to 800°C under the same condition. The intensity of the diffracted peak of $\alpha - \text{Fe}(\text{Si})$ phase in the alloy is increased with the increase of annealing temperature. For an annealing at higher temperature i.e. 550°C 600°C 650°C 700°C 750°C and 800°C , the $\alpha - \text{Fe}(\text{Si})$ phase were found at the lower values of 2θ at. % 45.008° , 44.942° , 44.938° , 44.918° , 44.89° and 44.95° respectively with 100% peak intensity on (110) line. The other two fundamental peaks are corresponding to $\alpha - \text{Fe}(\text{Si})$ on (200) and

(211) at $2\theta = 65.81^\circ$ and 83.69° around to bcc Fe (Si) phase. But due to their low intensity; there are not clearly visible before 650°C annealing. The balance of composition is maintained by the distribution of amorphous phase in the system.

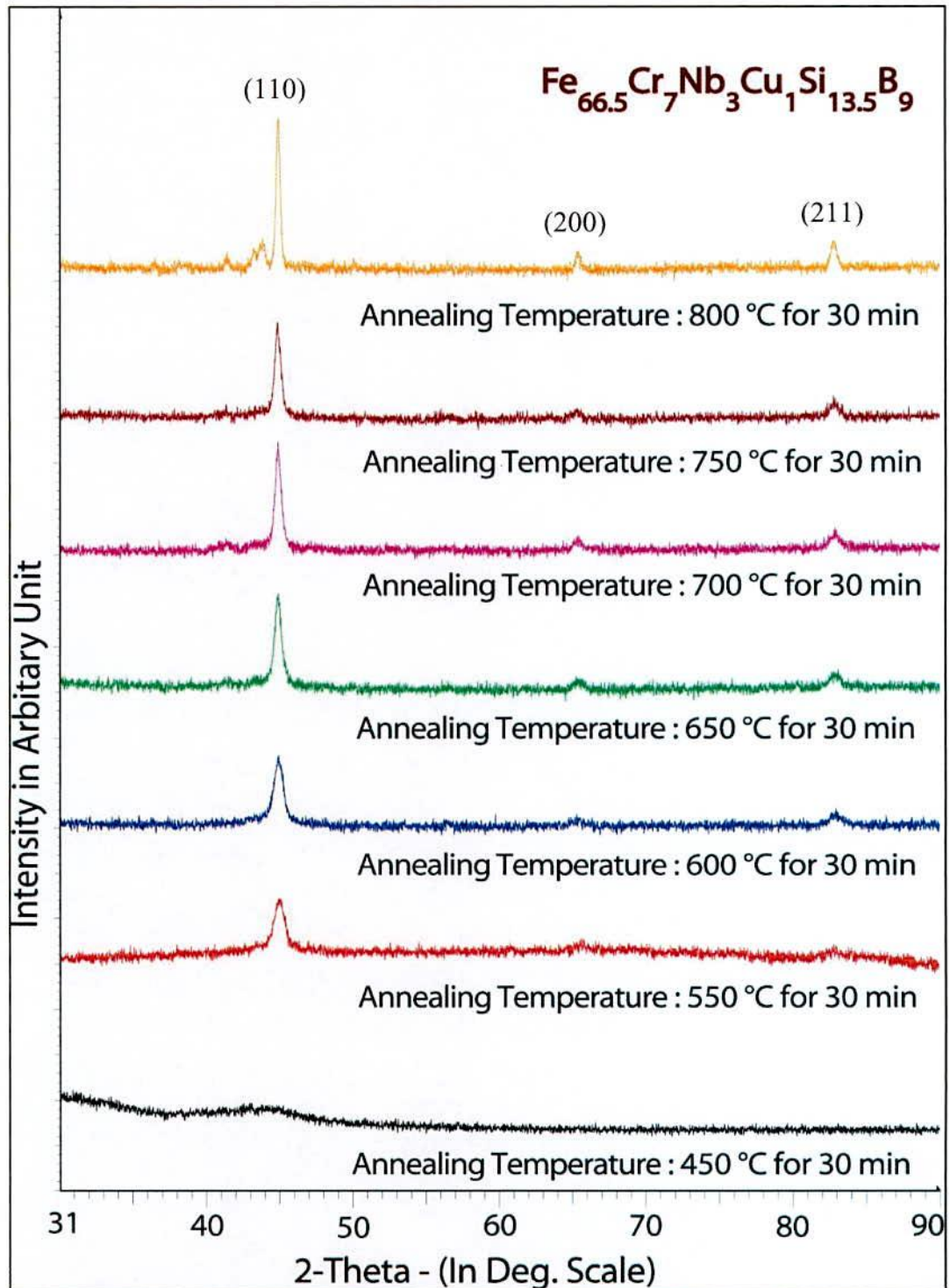


Fig. 5.14 XRD spectra of $\text{Fe}_{66.5}\text{Cr}_7\text{Nb}_3\text{Cu}_1\text{Si}_{13.5}\text{B}_9$ alloys of annealed at different temperatures at constant annealing time 30 min

From DTA result it is expected that boride phase would form beyond 580.6°C but the formation of crystalline phase other than Fe(Si) in the XRD pattern has not been detected for T_a up to around 550°C for the sample as expected from the DTA analysis of samples. The XRD patterns illustrated in Fig. 5.14 reveal that the difference in the Bragg's peak as well as the intensity of the fundamental reflections become gradually stronger as the temperature of the heat treatment increases. This increase in the sharpness of the intensity peaks with the annealing temperature indicates that crystalline volume fraction has been increases and also grains become coarser with increased spectra of the thermally treated samples of Cr substituted FINEMET's evidence of $\alpha - Fe(Si)$ and Fe_2B crystalline phases might be found along with iron oxides ($\alpha - Fe_2O_3$ and $\lambda - Fe_2O_3$) of less than 1% of the total composition [5.12]. The reason of oxide formation lies in fact of performing annealing in air atmosphere. In spite of addition of refractory elements it should be suggested that the heat treatment should be done in an inert (non-reactive) atmosphere to avoid oxidation and other reactions.

The intensity of the diffracted peak of $\alpha - Fe(Si)$ phase in the alloy is increased with the increase of annealing temperature. The systematic but negligible shift of the peak forwards the larger angles with increasing temperature indicates that lattice parameter of the phase gradually decreases due to the increase of Si-content of the $\alpha - Fe(Si)$ phase. Both the decrease in lattice parameter and increase in intensity of the fundamental peak with increasing annealing temperature suggest that Si-atom diffuse most intensively into the bcc-Fe with increase of annealing temperature. The diffusion of Si in bcc $\alpha - Fe$ is finally found as the nanocrystalline bcc $\alpha - Fe(Si)$ lattice which is identified by XRD and therefore we see the increase intensity due to increase of the crystalline part in the alloy.

The lattice parameter, the Si-content in bcc nanograins and the grain size of bcc grain can easily be calculated from the fundamental peak of (110) reflection. All the results are shown in Table 5.11.

Table 5.11 Experimental XRD data of nanocrystalline $Fe_{66.5}Cr_7Nb_3Cu_1Si_{13.5}B_9$ for different annealing temperature

Annealing Temp. in $^{\circ}C$	θ (deg.)	d (\AA)	FWHM (deg.)	a_0 (\AA)	D_g (nm)	Si (at %)
450	--	--	--	--	--	--
550	22.504	2.0141	0.765	2.8484	11	12.61
600	22.471	2.0169	0.660	2.8523	13	10.78
650	22.469	2.0171	0.485	2.5826	18	10.64
700	22.459	2.0179	0.466	2.8538	19	10.08
750	22.445	2.0191	0.460	2.8555	19	09.28
800	22.475	2.0166	0.311	2.8518	28	11.01

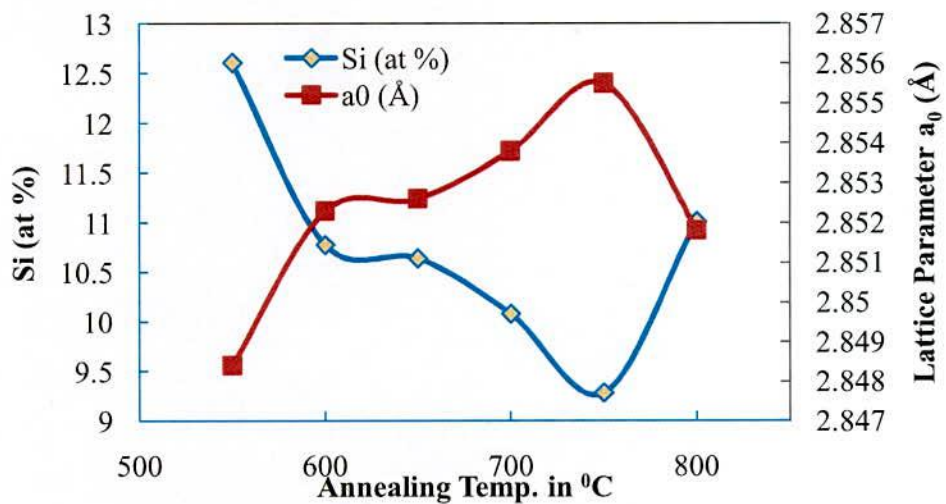


Fig. 5.15 Change of Si (at. %) content and Lattice Parameter with different annealing temperature for the sample with composition $Fe_{66.5}Cr_7Nb_3Cu_1Si_{13.5}B_9$

Fig. 5.15 shows the lattice parameter of $\alpha - Fe(Si)$ crystallites embedded in the amorphous matrix of various annealed samples in the temperature from $550^{\circ}C$ to $800^{\circ}C$ has been performed. With the increases of annealing temperature lattice parameter increases gradually up to $750^{\circ}C$ above this temperature decreases. The lattice parameter of $\alpha - Fe(Si)$ phase is always smaller than that of pure Fe, the value of which is 2.8664\AA [5.16]. When the annealing temperature is above $750^{\circ}C$ there is a decrease of lattice parameter due to the contraction of $\alpha - Fe$ lattice as a result of diffusion of the Si with smaller grain size from a substitution solid solution during the crystallization process of $\alpha - Fe(Si)$. The Si-contents of the alloy $Fe_{66.5}Cr_7Nb_3Cu_1Si_{13.5}B_9$ at different annealing temperature $550^{\circ}C$ to $800^{\circ}C$ for 30

minutes annealing time are found to be in the range of 9.28% to 12.61%. All these results are presented in Table 5.11 and the pattern of change in Si-content with respect to annealing temperature is presented in Fig. 5.15. Percentage of Si is the controlling parameter of structural change for the nanocrystalline alloy. Percentage of Si in the $Fe(Si)$ phase has a point of saturation i.e. maximum value. For this sample it is about 9.28% Si and obtained at $750^{\circ}C$. Above this critical temperature of Si increases i.e. lattice parameter decreases. So Si-content and lattice parameter is closely related which is expressed in Pearson Hand book relationship [5.15].

Instrumental broadening of the system was determined from $\theta - 2\theta$ scan of standard Si. At the position of (110) reflections, the value of instrumental broadening was found to be $0.07^{\circ}C$. This value instrumental broadening was obtained FWHM value of each peak. Asymmetrical broadening of the peak due to stacking fault of bcc crystal was corrected negligible in the present case. All determined grain size was values for every step of heat treatment are listed in Table. 5.11. In Fig. 5.14 it is clear that at low annealing temperature $550^{\circ}C$, the FWHM of the peak is large and with the increases of annealing temperature, the values of FWHM are getting smaller. The peaks are, therefore becoming sharper with the shifting the peak position towards higher 2θ value. The peak shifts indicate the change of the values of Si-content of nanograins and therefore, the change of the values of lattice parameter of nanograins.

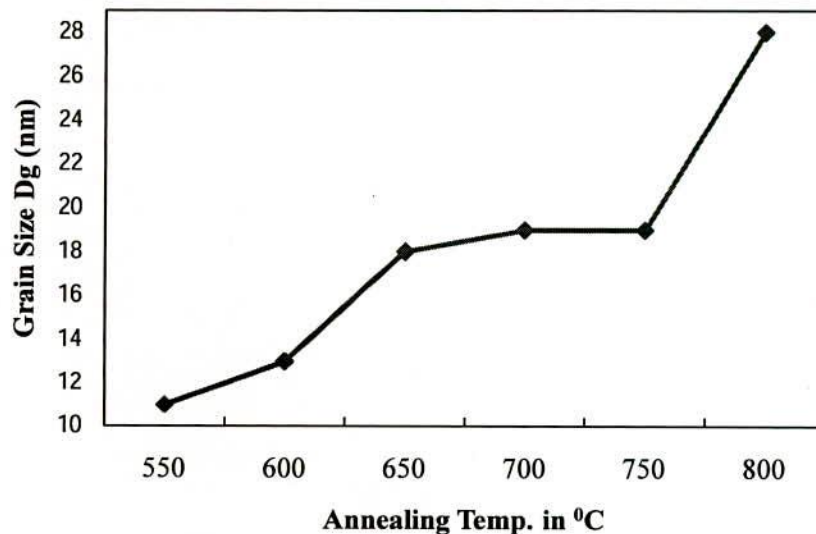


Fig. 5.16 Change of Grain Size with different annealing temperature for the sample with composition $Fe_{66.5}Cr_7Nb_3Cu_1Si_{13.5}B_9$

Fig. 5.16 and Table 5.11 that grain size increases with annealing temperature from a value of $D_g = 11$ nm for $T_a = 550^\circ\text{C}$ to $D_g = 28$ nm for the sample annealed at $T_a = 800^\circ\text{C}$ while Si-content decreases with annealing temperature. The increases of annealing temperature initiates partitioning of Si in the bcc Fe phase and thus grain growth due to formation of nanocrystalline bcc Fe(Si) grains. In the range of annealing temperature 550°C to 750°C , the grain size remains in the range of 11 to 19 nm corresponding to soft magnetic bcc Fe(Si) phases. Above 750°C , grain grow rapidly at attain value of 28 nm at 800°C indicating formation of Fe_2B phase. Formation of boride phase is detrimental to soft magnetic properties. Thus fact reveals that heat treatment temperature should be limited with 650°C to 750°C to obtain soft magnetic behavior, which will be clear that constant grain size. The formation of the nanometric microstructure corresponding to the grain growth with increase of annealing temperature is ascribed to combined effects of Cu and Nb and their low solubility in Fe. Cu which is insoluble in $\alpha - \text{Fe}(\text{Si})$, segregates prior to at the very beginning of nanocrystallization forming Cu-rich clusters and the nucleation of Fe(Si) grains is thought to be multiplied by clustering of Cu which stands as the reason for the grain growth at the initial stage of crystallization. It was observed that grain size 11nm for the sample annealed at 550°C for 30 minutes to a limiting value of 13-19 nm between annealing temperature 600°C to 750°C .

5.4.2 XRD Analysis of the Nanocrystalline Ribbon with Composition $\text{Fe}_{64.5}\text{Cr}_9\text{Nb}_3\text{Cu}_1\text{Si}_{13.5}\text{B}_9$

Fig. 5.17 shows typical XRD patterns of bcc $\alpha - \text{Fe}(\text{Si})$ phase for the sample of composition $\text{Fe}_{64.5}\text{Cr}_9\text{Nb}_3\text{Cu}_1\text{Si}_{13.5}\text{B}_9$ after heat treatment (30 minutes) at different temperature. From 450°C to 800°C pattern of $T_a = 450^\circ\text{C}$ & 550°C indicates the amorphous nature. After heat treatment at $T_a = 600^\circ\text{C}$ initiation of crystallization takes place. The same patterns were observed for all samples at different annealing temperature indicating the bcc $\alpha - \text{Fe}(\text{Si})$ phase which are developed on amorphous ribbon after heat treatment. Moreover, the bcc Fe-phase is unique crystalline of the alloys annealed at 600°C to 800°C , the variation of intensity of the diffraction lines in patterns obtained under the same condition, reveals that the peak of bcc Fe-phase in the alloys is increased with increase of the annealing temperature of crystalline

nanograin of bcc Fe (Si) phase. All the results of θ , d-value, FWHM, a_0 , D_g and Si (at. %) at different annealing temperature of these composition are listed in Table 5.12. For a annealing at higher temperature i.e., 600°C, 650°C, 700°C, 750°C and 800°C, the $\alpha - Fe(Si)$ phase were found at the lower values of 2θ at % 45.46°, 44.92°, 44.8°, 44.989° and 44.908° respectively with 100% peak intensity on (110) line. The other two fundamental peaks corresponding to $\alpha - Fe(Si)$ on (200) and (211) diffraction line for annealing temperatures at and above 650°C is obtained in this Fig. 5.17. But due to their low intensity, they are not clearly visible before 600°C annealing.

In the Fig. 5.18 the lattice parameter of $\alpha - Fe(Si)$ crystallites embedded in the amorphous matrix of various annealed samples in the temperature range between 600°C to 800°C has been performed. With the increase of annealing temperature lattice parameter increases gradually up to 700°C above this temperature decreases. The lattice parameter of $\alpha - Fe(Si)$ phase is always smaller than that of pure-Fe, the value of which is 2.8664 Å. The Si-content of the alloy $Fe_{64.5}Cr_9Nb_3Cu_1Si_{13.5}B_9$ at different annealing temperature 600°C to 800°C at constant annealing time 30 minutes are found to be in the range of 9.00% to 10.87%. All these results are presented in Table 5.12 and the pattern of change in Si-content with respect to annealing temperature is presented in Fig. 5.18. It is observed that the Si-content in $\alpha - Fe(Si)$ phase decreases with increases annealing temperature up to 700°C and above then Si-content increases again. Above or below this critical annealing temperature % Si decreases as lattice parameter increases. In Table 5.12 it is clear that with the increase of annealing temperature the value of FWHM decreases. The peak is, therefore, getting sharper with the shifting of peak position forwards higher 2θ value.

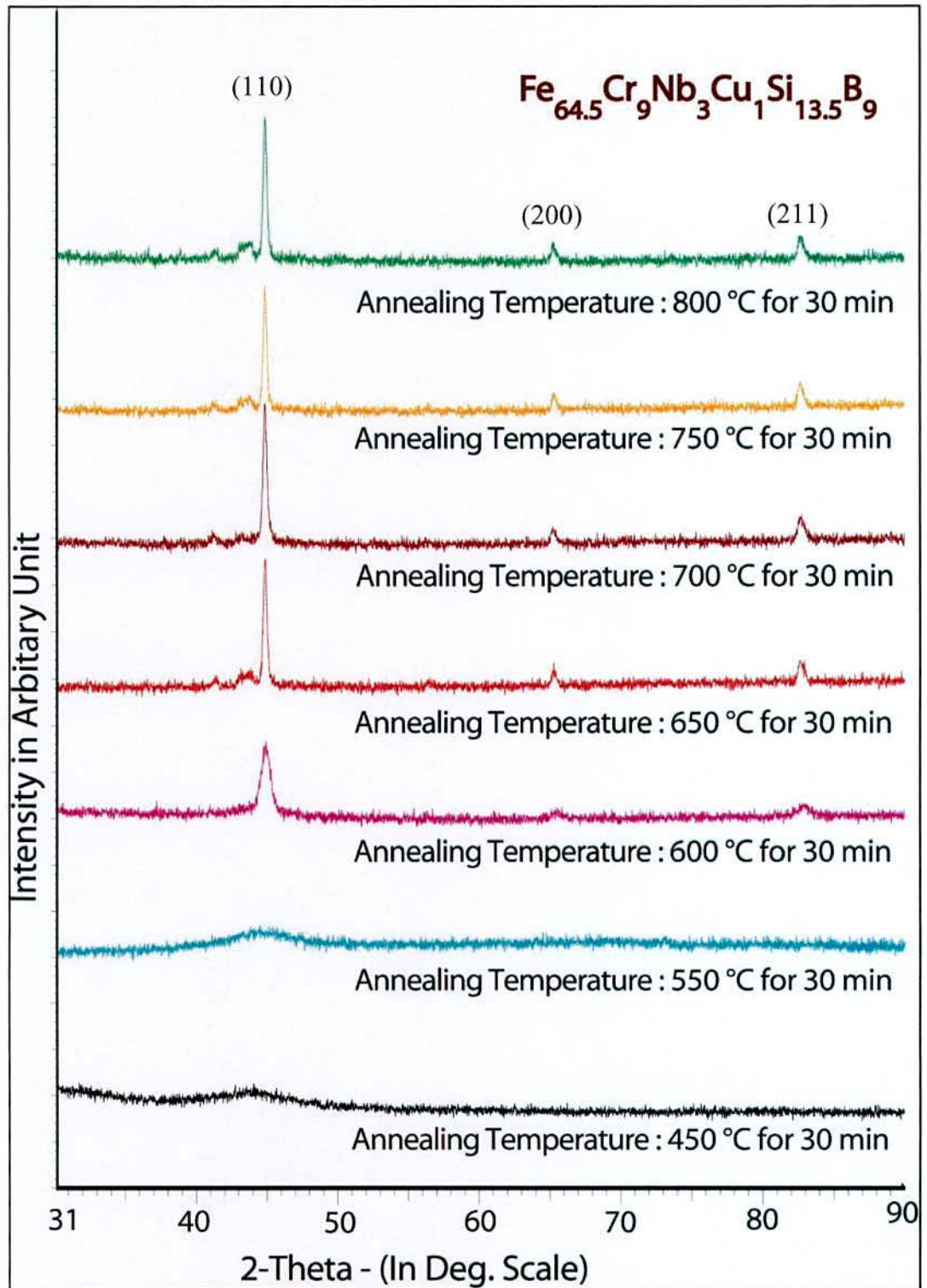


Fig. 5.17 XRD spectra of $\text{Fe}_{64.5}\text{Cr}_9\text{Nb}_3\text{Cu}_1\text{Si}_{13.5}\text{B}_9$ alloys of annealed at different temperature at constant annealing time 30 min

Table 5.12 Experimental XRD data of nanocrystalline $\text{Fe}_{64.5}\text{Cr}_9\text{Nb}_3\text{Cu}_1\text{Si}_{13.5}\text{B}_9$ amorphous ribbon at different annealing temperatures

Annealing Temp. in $^{\circ}\text{C}$	θ (deg.)	d (\AA)	FWHM (deg.)	a_0 (\AA)	D_g (nm)	Si (at %)
450	--	--	--	--	--	--
550	--	--	--	--	--	--
600	22.473	2.0167	0.653	2.8521	13	10.87
650	22.460	2.0178	0.307	2.8536	28	10.17
700	22.440	2.0195	0.315	2.8561	27	09.00
750	22.449	2.0188	0.288	2.8550	30	09.52
800	22.454	2.0183	0.287	2.8544	30	09.81

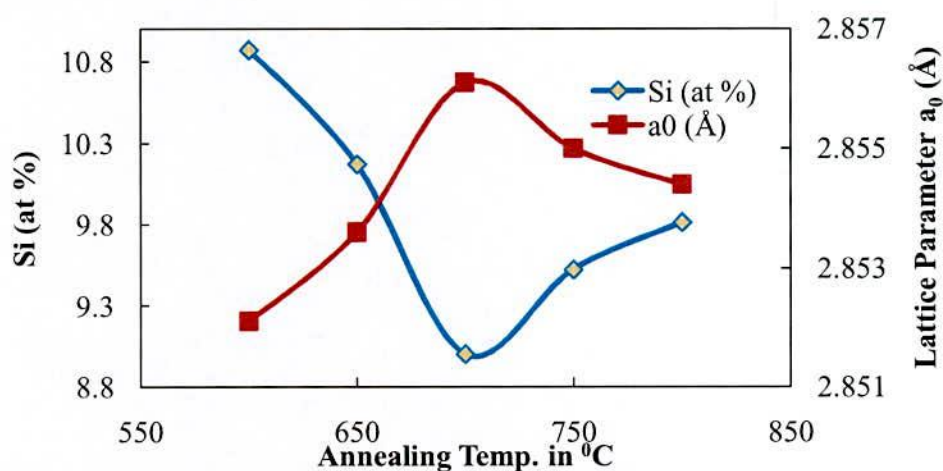


Fig. 5.18 Change of Si (at %) content and Lattice Parameter with different annealing temperature for the sample with composition $\text{Fe}_{64.5}\text{Cr}_9\text{Nb}_3\text{Cu}_1\text{Si}_{13.5}\text{B}_9$

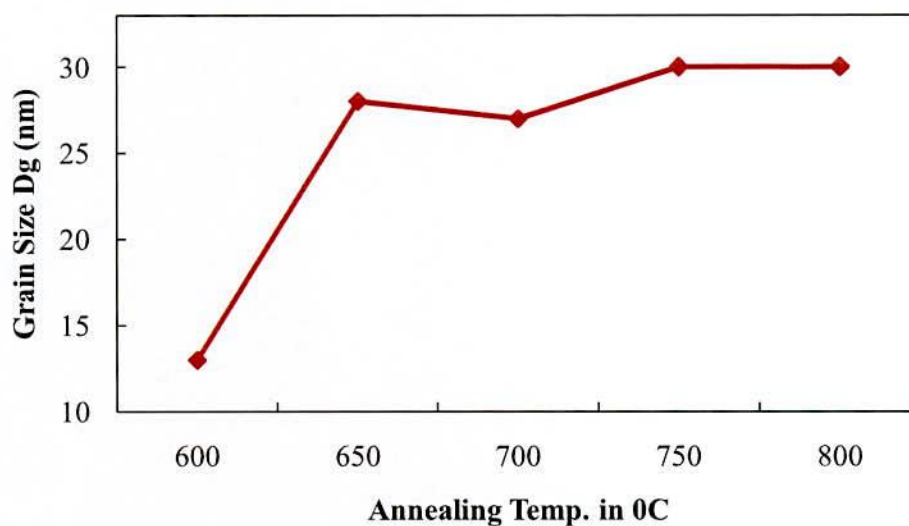


Fig. 5.19 Change of Grain Size with different annealing temperature For the sample with composition $\text{Fe}_{64.5}\text{Cr}_9\text{Nb}_3\text{Cu}_1\text{Si}_{13.5}\text{B}_9$

In Fig. 5.19 the mean grain size of the nanograins determined from the X-ray fundamental line (110) using the Scherrers formula are presented. The increasing of annealing temperature initiates partitioning of Si in the bcc Fe phase and thus grain growth due to formation of nanocrystalline bcc Fe(Si) grains. In the range of annealing temperature 600°C to 800°C, the grain size remains in the range 13 to 30 nm. These facts reveal that heat treatment temperature should be limited with 650°C to 800°C to obtained soft magnetic behavior which will be clear that nearly constant grain size.

5.4.3 XRD analysis of the Nanocrystalline Ribbon with composition

$\text{Fe}_{63.5}\text{Cr}_{10}\text{Nb}_3\text{Cu}_1\text{Si}_{13.5}\text{B}_9$

The XRD patterns for the $\text{Fe}_{63.5}\text{Cr}_{10}\text{Nb}_3\text{Cu}_1\text{Si}_{13.5}\text{B}_9$ annealed at temperature (T_a) 450°C, 550°C, 600°C, 650°C, 700°C, 750°C and 800°C each for 30 minutes are presented in Fig. 5.20. Form 450°C to 800°C pattern of $T_a = 450^\circ\text{C}$ and 550°C indicates the amorphous nature. Due to annealing at 600°C, the first crystallization peak was found at the angle 45.04°. It means at the annealing temperature below 600°C, no crystalline peak has been detected. After heat treatment at $T_a = 600^\circ\text{C}$ initiation of crystallization takes place. For annealing at higher temperature i.e., 600°C, 650°C, 700°C, 750°C and 800°C, the bcc $\alpha - \text{Fe}(\text{Si})$ phase were found at the lower values of 2θ at % 45.04°, 44.902°, 44.852°, 44.864° and 44.896° r espectively with 100% peak intensity on (110) line. The other two fundamental peaks corresponding to $\alpha - \text{Fe}(\text{Si})$ on (200) and (211) diffraction line for annealing temperatures at and above 650°C is obtained in this Figure. But due to their low intensity, they are not clearly visible before 600°C annealing. The balance of composition is obtained by distribution of amorphous phase in the system.

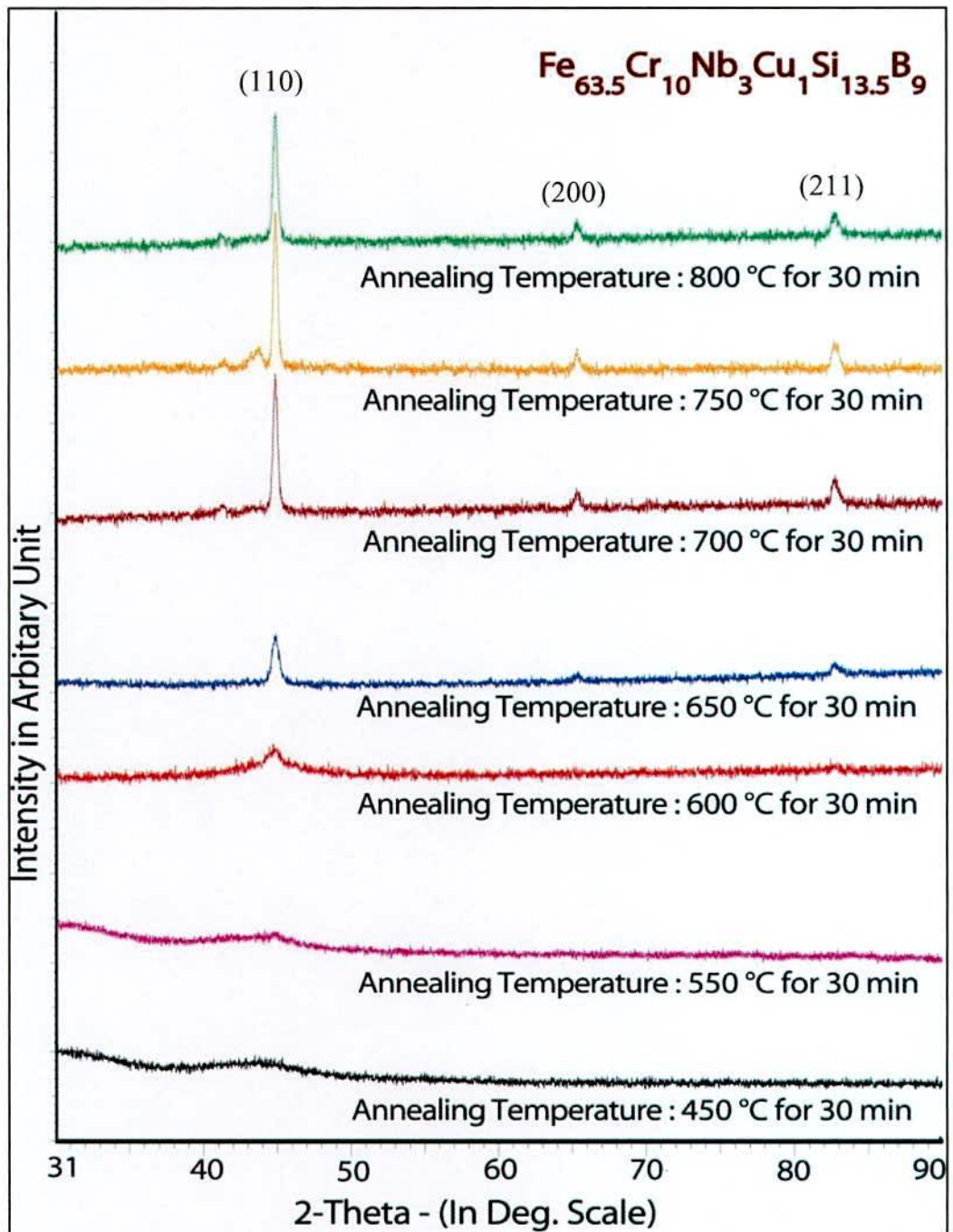


Fig. 5.20 XRD spectra of $Fe_{63.5}Cr_{10}Nb_3Cu_1Si_{13.5}B_9$ alloys annealed at different temperatures at constant annealing time 30 min

The XRD patterns illustrated in Fig. 5.20 reveal that the difference in the Bragg's peak as well as the intensity of the fundamental reflections becomes gradually stronger as the temperature of the heat treatment increases. This increase in the sharpness of the intensity peaks with the annealing temperature indicates that the crystalline volume fraction has been increased and also grains become coarser with

increased crystallinity. The systematic but negligible shift of peak forwards the larger angles with decreasing temperature indicates that lattice parameter of the phase gradually increases due to the decreasing of Si-content of the $\alpha - Fe(Si)$ phase. The lattice parameter, the Si-contents in bcc nanograins and the grain size of bcc grain can easily be calculated from the fundamental peak of (110) reflection. All the results are shown in Table 5.13.

Table 5.13 Experimental XRD data of nanocrystalline $Fe_{63.5}Cr_{10}Nb_3Cu_1Si_{13.5}B_9$ amorphous ribbon at different annealing temperatures

Annealing Temp. in °C	θ (deg.)	d (Å)	FWHM (deg.)	a_0 (Å)	D_g (nm)	Si (at. %)
450	--	--	--	--	--	--
550	--	--	--	--	--	--
600	22.520	2.0127	0.737	2.8464	12	13.53
650	22.451	2.0186	0.525	2.8547	16	09.66
700	22.426	2.0207	0.344	2.8578	25	08.21
750	22.432	2.0202	0.340	2.8570	29	08.58
800	22.448	2.0189	0.332	2.8551	26	09.47

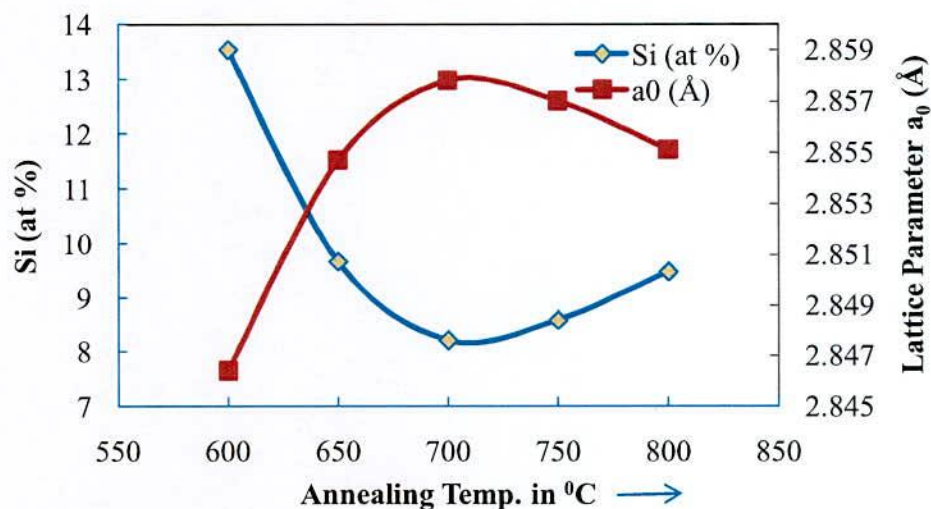


Fig. 5.21 Change of Si (at. %) content and Lattice Parameter with different annealing temperature for the sample with composition $Fe_{63.5}Cr_{10}Nb_3Cu_1Si_{13.5}B_9$

Fig. 5.21 shows that, with the increase in annealing temperature lattice parameter increasing up to 700°C, above the annealing temperature decreases. The lattice parameter of pure Fe is 2.8664Å. But the lattice parameter at various annealing temperature for the present alloy are significantly less than that of pure Fe. It is

notable that Si-contents in the nanocrystallites at different annealing temperatures are higher than Si-content of the amorphous precursor which 13.53 at %. The percentage of partitioned Si in the nanocrystalline $\alpha - Fe(Si)$ phase is maximum at 600°C. After 600°C, decrease in Si-content is observed up to 700°C, explained by the fact that at higher temperatures silicon diffuses out of nanograins due to crystallization corresponding to formation of boride phase which is consistent with the result of other FINEMET's. Fig. 5.21 presents the inverse relationship between lattice parameter and Silicon content. When the sample up to 700°C, the increase of lattice parameter with subsequent decrease of Si-content, as showed in Fig. 5.21 indicates that silicon diffuse out of $\alpha - Fe(Si)$ grains for which the size of $\alpha - Fe$ lattice is regained.

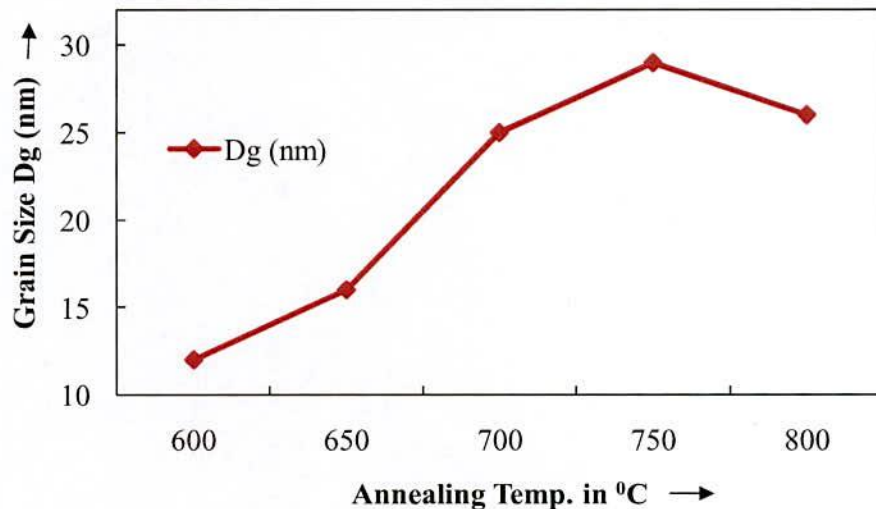


Fig. 5.22 Change of Grain Size with different annealing temperature for the sample with composition $Fe_{63.5}Cr_{10}Nb_3Cu_1Si_{13.5}B_9$

From Fig. 5.22 and Table 5.13 that grain size decreases with annealing temperature up to 750°C and above this annealed temperature grain size increase. In the range of annealing temperature 600°C to 800°C, the grain size remains in the range of 12 to 29 nm. Grain growth rapidly and attain value of 25 nm at 700°C indicating formation of boride phase. Formation of boride phase is detrimental to soft magnetic properties. These facts reveal that heat treatment temperature should be limited within 600°C to 650°C to obtain optimum soft magnetic behavior, which will be clear that nearly same grain size.

5.4.4 XRD Analysis of the Nanocrystalline Ribbon with composition



Fig. 5.23 shows typical XRD patterns of bcc $\alpha - Fe(Si)$ phase for the sample of composition $\text{Fe}_{61}\text{Cr}_{12.5}\text{Nb}_3\text{Cu}_1\text{Si}_{13.5}\text{B}_9$ after heat treatment (30 minutes) at different annealing temperature (T_a). From 450°C to 800°C pattern of $T_a = 450^\circ\text{C}$ to 600°C indicates are the amorphous nature. After heat treatment at $T_a = 650^\circ\text{C}$ initiation of crystallization takes place. The same patterns were observed for all samples at different annealing temperature indicating the bcc $\alpha - Fe(Si)$ phase which are developed on amorphous ribbon after heat treatment. For a annealing at higher temperature i.e., 650°C , 700°C , 750°C and 800°C , the bcc $\alpha - Fe(Si)$ phase were found at the lower values of 2θ at 44.82° , 44.788° , 44.82° and 44.864° respectively with 100% peak intensity on (110) line. The other two fundamental peaks corresponding to $\alpha - Fe(Si)$ on (200) and (211) diffraction line for annealing temperatures at and above 700°C is obtained in this figure. But due to their low intensity, they are not clearly visible before 700°C annealing. The balance of composition is obtained by distribution of amorphous phase in the system. The XRD patterns illustrated in Fig. 5.23 reveals that the difference in the Bragg's peak as well as the intensity of the fundamental reflections becomes gradually stronger as the temperature of the heat treatment increases. All the results of θ , d-value, FWHM, lattice parameter a_0 , the grain size (D_g) and the Si-content in bcc nanograins (at. %) can easily calculated from the fundamental peak of (110) reflection. All the results are shown in Table 5.14.

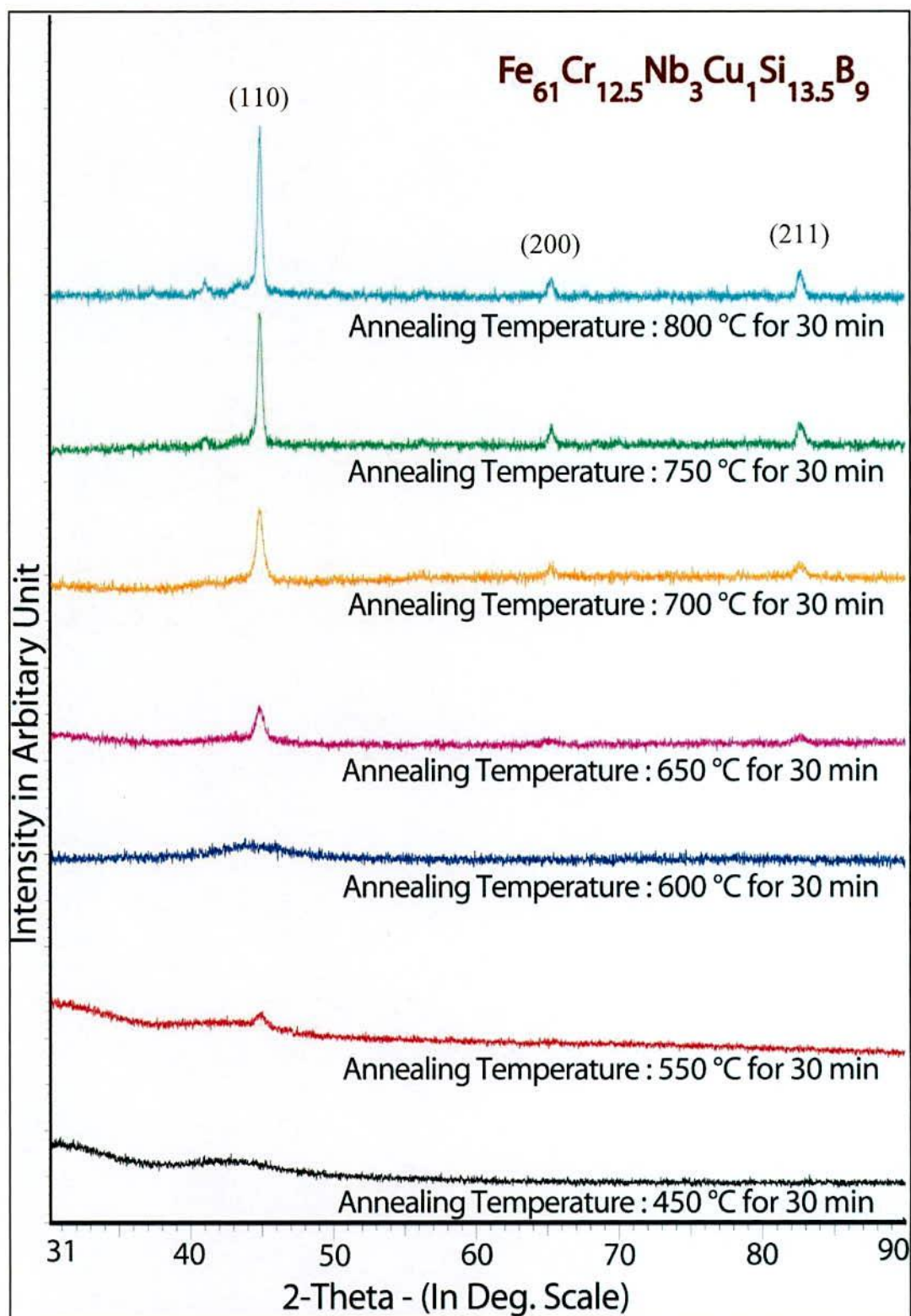


Fig. 5.23 XRD spectra of $\text{Fe}_{61}\text{Cr}_{12.5}\text{Nb}_3\text{Cu}_1\text{Si}_{13.5}\text{B}_9$ alloys of annealed at different temperature at constant annealing time 30 min

Table 5.14 Experimental XRD data of nanocrystalline $Fe_{61}Cr_{12.5}Nb_3Cu_1Si_{13.5}B_9$ amorphous ribbon at different annealing temperatures

Annealing Temp. in °C	θ (deg.)	d (Å)	FWHM (deg.)	a_0 (Å)	D_g (nm)	Si (at. %)
550	--	--	--	--	--	--
600	--	--	--	--	--	--
650	22.410	2.0201	0.556	2.8597	16	07.32
700	22.394	2.0235	0.524	2.8616	16	06.43
750	22.410	2.0221	0.349	2.8597	25	07.32
800	22.432	2.0202	0.296	2.8570	29	08.28

Fig. 5.24 shows that, with the increase in annealing temperature lattice parameter increasing up to 700°C, above this T_a lattice parameter drops rapidly. But a_0 at various annealing temperature for the present alloy are significantly less than that of pure Fe. The value of which is 2.8664Å. Above 700°C there is a decrease of lattice parameter due to the contraction of $\alpha - Fe$ lattice as a result of diffusion of the Si. From Fig. 5.24 it is observed that the Si-content in $\alpha - Fe(Si)$ phase decrease with annealing temperature up to 700°C. After 700°C increase in Si-content is observed. So Si-content and lattice parameter are closely related that is expressed in Pearson Hand book. Percentage of Si-content is the controlling parameter of structural change for the nanocrystalline alloy. Fig. 5.24 presents the inverse relationship between lattice parameter and Silicon content.

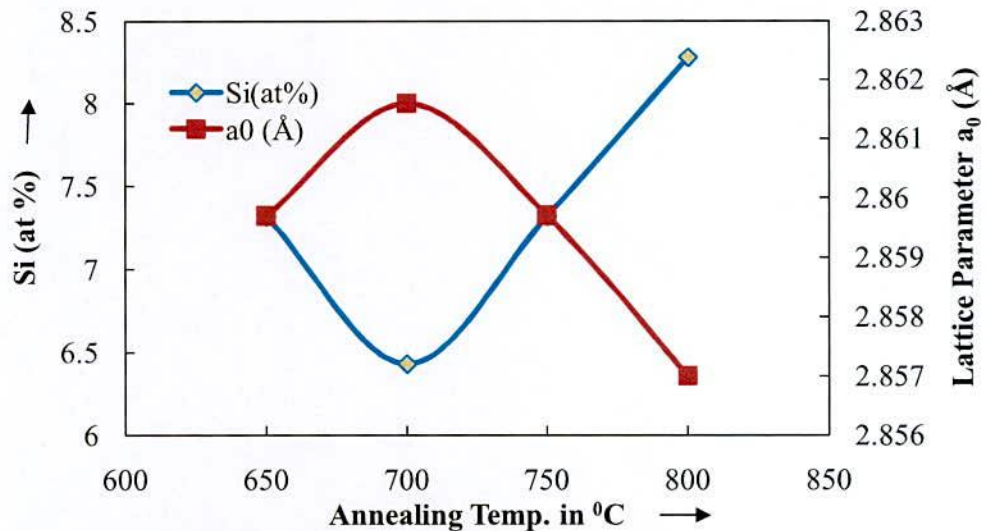


Fig. 5.24 Change of Si (at. %) content and Lattice Parameter with different annealing temperature for the sample with composition $Fe_{61}Cr_{12.5}Nb_3Cu_1Si_{13.5}B_9$

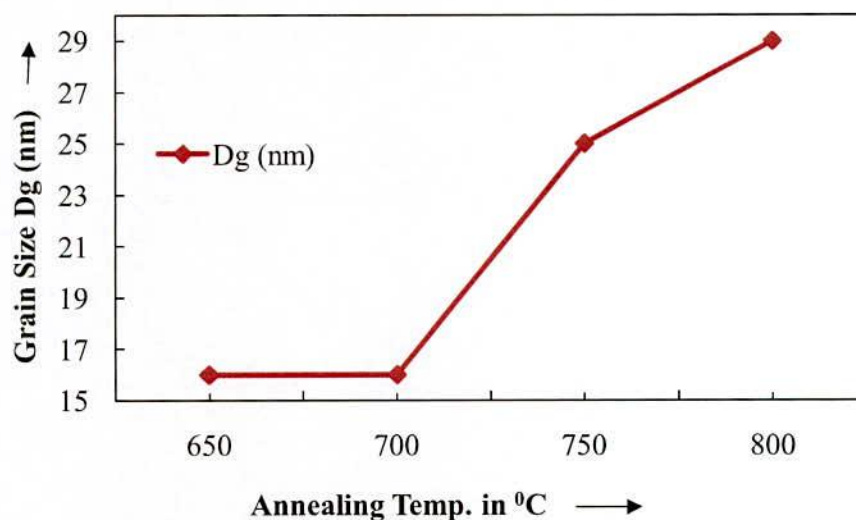


Fig. 5.25 Change of Grain Size with different annealing temperature for the sample with composition $\text{Fe}_{61}\text{Cr}_{12.5}\text{Nb}_3\text{Cu}_1\text{Si}_{13.5}\text{B}_9$

From Fig. 5.25 and Table 5.14 that grain size (d_g) constant up to 700°C and above this annealed temperature grain size increases. In the range of annealing temperature 650°C to 800°C , the grain size remains in the range of 16 to 29 nm. Grain growth rapidly and attain value of 25 nm at 750°C indicating formation of Boride phase. These facts reveal that heat treatment temperature should be limited within 650°C to 700°C to obtain optimum soft magnetic behavior, which will be clear that constant grain size.

5.5 Specific Magnetization Measurement of Fe-Cr-Nb-Cu-Si-B Nanocrystalline Amorphous Ribbons.

The magnetization of $\text{Fe}_{73.5-x}\text{Cr}_x\text{Nb}_3\text{Cu}_1\text{Si}_{13.5}\text{B}_9$ [$x = 7, 9, 10 \text{ \& } 12.5$] ribbon is measured as a function of magnetic field using a vibrating sample magnetometer (VSM) [5.17]. The magnetometer was used as a field measuring device which was not affected by the presence of sample for its low susceptibility. In this type of magnetometer the sample is vibrated up and down in a region surrounded by several pick up coils. The magnetic sample is thus acting as a time changing magnetic flux, varying inside a particular region of fixed area. The lock-in-action of VSM yields an accuracy of 0.05% of the full scale. The absolute accuracy of this system is better than 2% and the reproducibility is better than 1%. Least measurable moment is $5 \times 10^{-4} \text{ emu}$. The proportionality constant accounting for the particular coil geometry

and susceptibility is obtained by calibration with a high purity circular disk shaped Ni-sample. This sample has a saturation magnetization of about 54.75 emu/g with a saturation flux of about 4kOe at room temperature. A relative accuracy of about 1% is obtained with a double coils, the absolute accuracy depends on the calibration method. The ribbon samples were cut in to small shapes, weighed and glued to a standard sample holder

5.5.1 Specific Magnetization at Room Temperature

The Specific Magnetization of these Fe-Cr-Nb-Cu-Si-B ribbons with composition $\text{Fe}_{73.5-x}\text{Cr}_x\text{Nb}_3\text{Cu}_1\text{Si}_{13.5}\text{B}_9$ [$x = 7, 9, 10$ & 12.5] in as quenched condition is measured, using a VSM. The magnetization process of the nanocrystalline amorphous ribbons with different field are shown in Fig. 5.26. Specific saturation magnetization (M_s) process for these ribbons has lower values for increasing replacement of Fe by Cr. In contrast, magnetization measurement at room temperature, the sample with $x = 7, 9$ & 10 are saturated with an applied field of 8kOe. The sample with Cr content $x = 12.5$ do not show any sign of ferromagnetic nature, rather a very small value of magnetization is observed which increases almost linearly up to field of $H = 10\text{kOe}$. It is evident from the results that the M_s decreases as the Cr contents increase. The M_s for these ribbons have higher values for higher percentage of Fe. This is quite understandable from the consideration of higher contribution of magnetic moments in Fe-rich ribbons. It is observed that while the ribbon with composition $\text{Fe}_{66.5}\text{Cr}_7\text{Nb}_3\text{Cu}_1\text{Si}_{13.5}\text{B}_9$ reaches its saturation value around 5kOe, $\text{Fe}_{64.5}\text{Cr}_9\text{Nb}_3\text{Cu}_1\text{Si}_{13.5}\text{B}_9$ requires 7kOe and $\text{Fe}_{63.5}\text{Cr}_{10}\text{Nb}_3\text{Cu}_1\text{Si}_{13.5}\text{B}_9$ requires 4.5kOe. Magnetization is also evaluated as a function of field to find the dependence of magnetization on the domain structure.

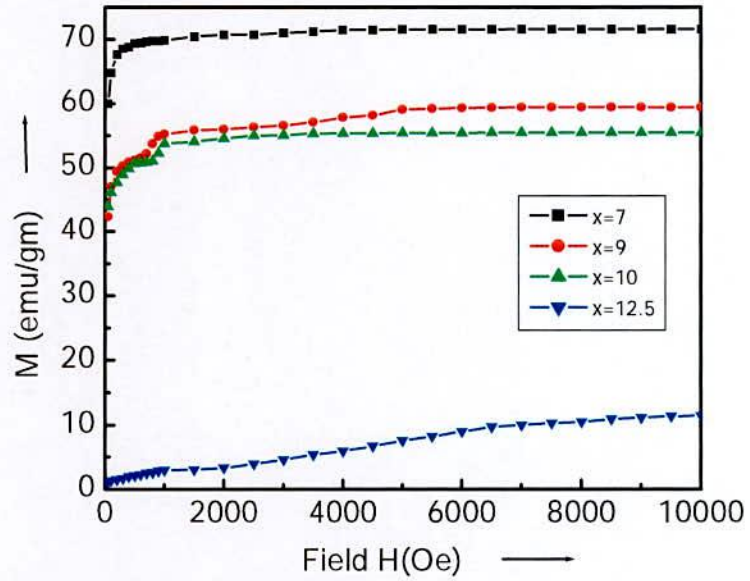


Fig. 5.26 Field dependence of magnetization of amorphous $\text{Fe}_{73.5-x}\text{Cr}_x\text{Nb}_3\text{Cu}_1\text{Si}_{13.5}\text{B}_9$ ribbons with $x = 7, 9, 10$ & 12.5 alloys at room temperature

The saturation magnetization, M_s and Magnetization (M) 10kOe for different samples as calculated are shown in Table 5.16.

Table 5.16 Curie temperature and saturation magnetization of nanocrystalline amorphous ribbons with $\text{Fe}_{73.5-x}\text{Cr}_x\text{Nb}_3\text{Cu}_1\text{Si}_{13.5}\text{B}_9$ alloys

Cr-content x at%	Saturation Magnetization M_s in emu/s at room temperature	Magnetization M in emu/s at 10kOe	Curie Temperature T_c in $^{\circ}\text{K}$	Curie Temperature T_c in $^{\circ}\text{C}$
$x=7$	71.52	71.52	410	137
$x=9$	59.12	59.12	372	99
$x=10$	55.41	55.41	366	93
$x=12.5$	-----	11.12	246	- 28

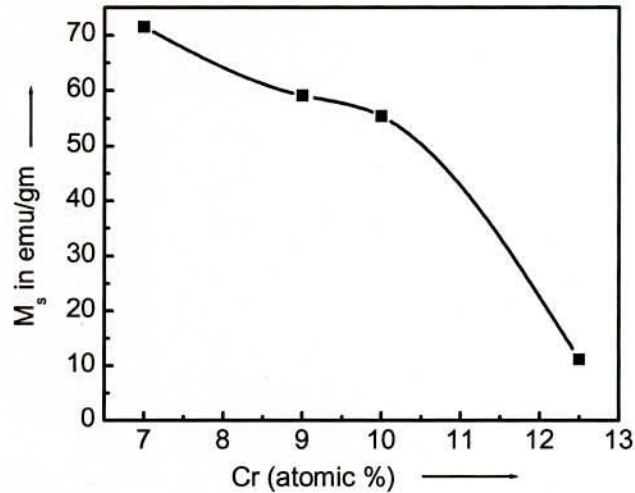


Fig. 5.27 Variation of Saturation magnetization due to change in the Cr-content in $Fe_{73.5-x}Cr_xNb_3Cu_1Si_{13.5}B_9$ nanocrystalline ribbons at constant applied field 10kOe

The magnetization, M decreases with increasing Cr-content as shown in Fig. 5.27. This may be attributed to the dilution of Fe magnetic moment by the substitution of non-magnetic Cr. Saturation magnetization value of $M_s = 160$ emu/g at room temperature for $x = 0$ which decreases monotonically with the successive substitution of Fe by Cr and attains a value of $M_s = 55.41$ emu/g at room temperature for $x = 10$. The saturation magnetization value M_s for the original FINEMET alloy i.e. $x = 0$ was found to be comparable within an experimental error of $\pm 5\%$ by several investigators [5.18-5.20]. Magnetic saturation can be achieved only for Fe-based alloys. In this case, the total anisotropy is small and the next nearest neighbor exchange coupling leads to ferromagnetic order. The critical composition for the disappearance of ferromagnetism full of curve M_s with the replacement Fe by Cr, where the nearest neighbor coupling is no longer dominant and an intermediate range occur, giving rise to a significant portion of antiferromagnetic interaction.

5.5.2 Temperature Dependence of Specific Magnetization Fe-Cr-Nb-Cu-Si-B Nanocrystalline Amorphous Ribbons

The variation of saturation magnetization (M_s) as a function of temperature in the range 300K to 600K measured with an applied field of 10kOe in the amorphous state for the nanocrystalline amorphous samples with composition $Fe_{73.5-x}Cr_xNb_3Cu_1Si_{13.5}B_9$ are shown in Fig. 5.28(a), 5.28(b) and 5.28(c). The magnetization

of all the samples decreases gradually with increasing temperature since the thermal energy is acting on opposition to the magnetic coupling or exchange energy between neighboring atoms. From these curve Curie temperature (T_c) has been determined as the temperature corresponding to the inflexion point where the rate of change of magnetization with respect to temperature is maximum shown in Fig. 5.30. As the temperature approaches to the T_c , magnetization falls more rapidly near to zero as the thermal energy exceeds the magnetic ordering or the exchange energy. Fig. 5.29 shows the T_c determined in this method varies 100 to 400K for $x = 12.5$ at % Cr within an experimental uncertainty $\pm 3K$; since magnetization was recorded. It is clearly observed from the curves of Fig. 5.29 that the saturation magnetization of the sample at low temperature decreases gradually as the sample $Fe_{61}Cr_{12.5}Nb_3Cu_1Si_{13.5}B_9$ ribbon. It is also noticed that magnetization at low temperature decreases slowly with the increase of temperature and falls faster the T_c . As a result the samples undergoes a ferro-paramagnetic phase transition at $T = T_c$ in the amorphous state. It is observed that the magnetization and the T_c of all the amorphous nanocrystalline samples both decreases as the Cr-content increase implying the effect of Cr on the dilution of magnetic moment as well as the weakening of exchange interaction between Fe magnetic moments are shown in table 5.16. The reduction of T_c with the substitution of non-magnetic Cr may be attributed to this simultaneous weakening of the strength of exchange interaction between the Fe magnetic moments. In spite of careful determination of T_c of the amorphous alloys by various methods ambiguity of T_c values still remains a open question specially for the amorphous glassy metal alloys are basically metastable materials. It has been demonstrated by numerous experimental evidences that when the materials with the same composition are produced with different quenching rate, magnetic properties, in particular the T_c can vary substantially. This fact prevents a reliable comparison between results obtained different laboratories [5.21]. The T_c of original FINEMET has been found to vary from 590K to 630K. Therefore the initial amorphous state should be taken in to account.

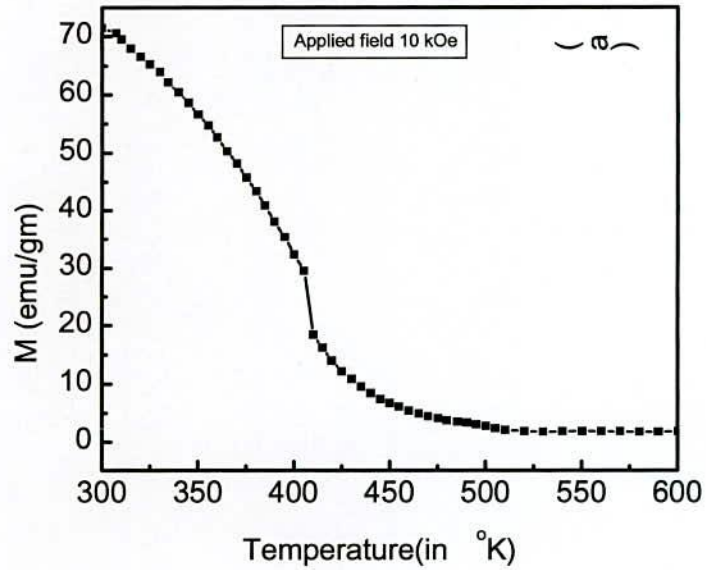


Fig. 5.28(a) Temperature dependence of specific magnetization of amorphous nanocrystalline ribbons with composition $\text{Fe}_{66.5}\text{Cr}_7\text{Nb}_3\text{Cu}_1\text{Si}_{13.5}\text{B}_9$ alloy

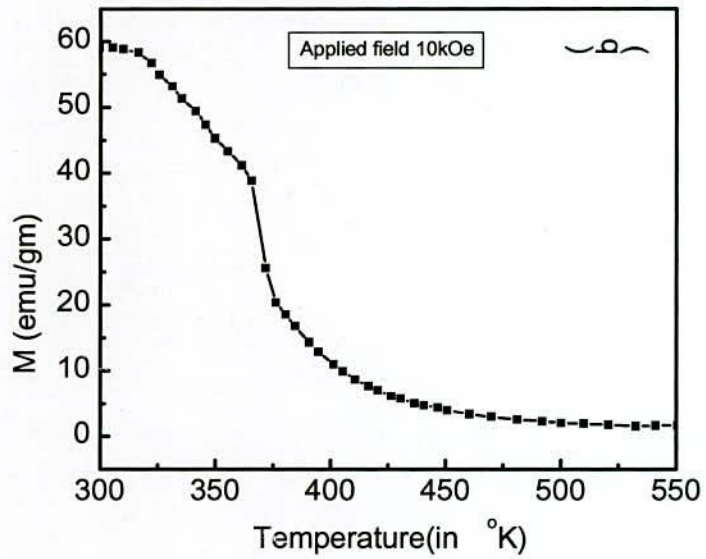


Fig. 5.28(b) Temperature dependence of specific magnetization of amorphous nanocrystalline ribbons with composition $\text{Fe}_{64.5}\text{Cr}_9\text{Nb}_3\text{Cu}_1\text{Si}_{13.5}\text{B}_9$ alloy

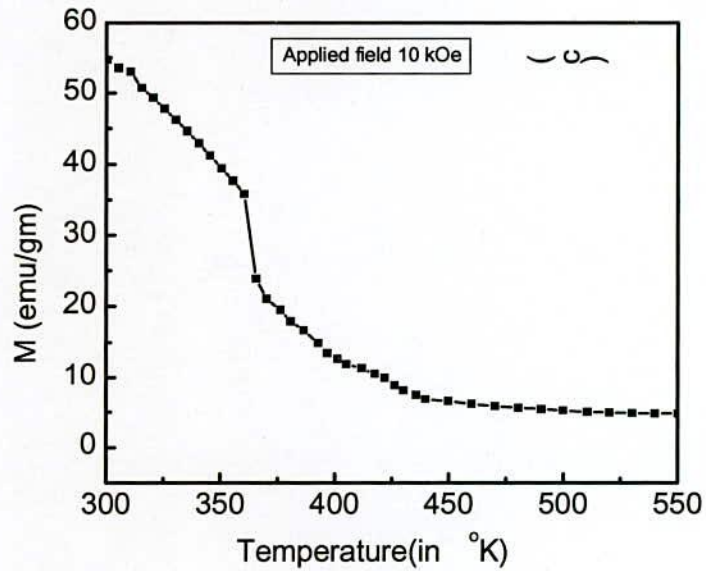


Fig. 5.28(c) Temperature dependence of specific magnetization of amorphous nanocrystalline ribbons with composition $\text{Fe}_{63.5}\text{Cr}_{10}\text{Nb}_3\text{Cu}_1\text{Si}_{13.5}\text{B}_9$ alloy

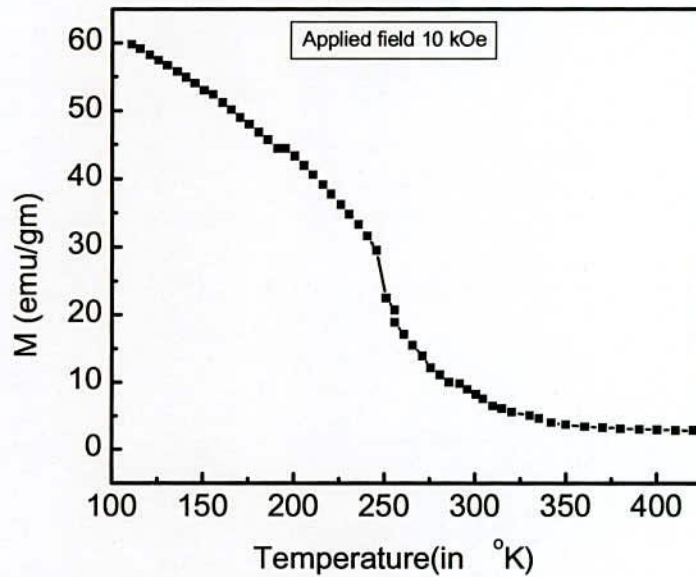


Fig. 5.29 Temperature dependence of specific magnetization of amorphous nanocrystalline ribbons with composition $\text{Fe}_{61}\text{Cr}_{12.5}\text{Nb}_3\text{Cu}_1\text{Si}_{13.5}\text{B}_9$ alloys at constant applied field 10kOe

From the above measurements it has been elucidated that the thermomagnetic measurement is a powerful technique to analyze the crystallization behavior

of amorphous ferromagnetic materials provided the crystallization products are ferromagnetic and the T_c of amorphous alloys lie below the crystallization temperature.

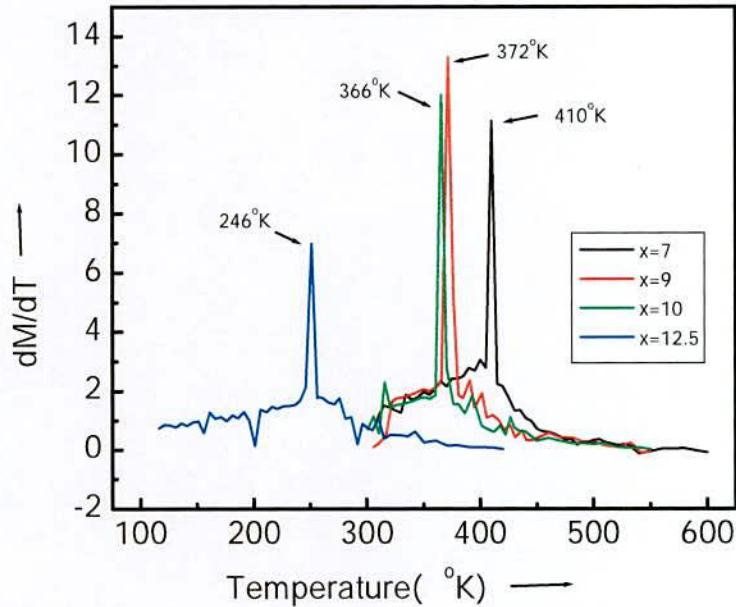


Fig. 5.30 $\frac{dM}{dT}$ versus temperature curve of amorphous Nanocrystalline ribbons with composition $Fe_{73.5-x}Cr_xNb_3Cu_1Si_{13.5}B_9$ [$x = 7, 9, 10 \& 12.5$]

5.6 Variation of Specific Magnetization with Isothermal Annealing of Higher Cr-content Amorphous Nanocrystalline Alloys.

This is well known that amorphous state is metastable. Metastability of amorphous or glassy metal alloys offers the possibility of phase separation diffusion of various species and structural relaxation even through the alloys remains amorphous when they are annealed at temperature well below the crystallization temperature. The specific magnetization of the nanocrystalline amorphous ribbons of composition $Fe_{73.5-x}Cr_xNb_3Cu_1Si_{13.5}B_9$ [$x = 7, 9, 10 \& 12.5$] alloys annealed for constant 30 minutes annealing time at varying temperature $500^\circ C$ to $600^\circ C$ have been measured as a function of magnetic field generated by an electromagnet using vibrating sample magnetometer (VSM). The present work is mainly aimed at studying the magnetization process of Fe-Cr-Nb-Cu-Si-B nanocrystalline ribbons as affected by varying annealing temperature at constant annealing temperature. Anneal effect on the intrinsic magnetic properties such as Curie temperature (T_c), Saturation

magnetization (M_s) and magnetostriction. It has been demonstrated that M_s and T_c of FINEMET alloys in the amorphous state increase on annealing up to annealing temperature (T_a) corresponding to the early stage of crystallization, beyond which M_s and T_c both decrease [5.18, 5.20, 5.22]. This provides information about the nature of residual strain in as prepared melt-spun ribbons and their effect on domain wall pinning. This study also provides important technical information about the possibility of using ribbons at elevated annealing temperature and the optimum operating points of these ribbons; when they are used as soft magnetic materials under varying fields. The detailed quantitative analysis of the situation is, therefore, very complex and present understanding of the problem of magnetization process as affected by these defects is not yet clear.

We can distinguish reversible and irreversible types of relaxation due to annealing temperature. Irreversible types of relaxation are these which are connected with thermally initiated microscope jumps of defects or ordering atomic pairs which correspond to irreversible domain wall movement under external field [5.23-5.25]. Thus reversibility of magnetization is not possible in these cases by reversing the external field. The reversible relaxation on the other hand means microstructural atomic rearrangement within the domain wall potential in a way that allows the reversal of the magnetic domain wall movements through reversing of the direction of the magnetic field. The present work will be confined to the later situation only. The criteria for the softest magnetic materials demand very high magnetization, high permeability and / or extremely low coercivity and these properties necessitate the anisotropy energy and the magnetoelastic energy and towards zero. These unique demands are fulfilled when the FINEMET type of nanocrystalline materials are thermally treated around their primary crystallization temperature which facilitates the evolution of nanometric size of the Fe(Si) grains (11-16nm) that are exchanged couple through the remaining thin residual amorphous interface. The present results are interpreted in terms of conventional domain theory of ferromagnetization, where it is postulated that the effect of annealing temperature is to partially remove the pinning centers of the domain wall and thereby improving the magnetic softness of these ribbons.

5.6.1 Effect of Annealing Temperature on Specific Magnetization at Room Temperature

The FINEMET is ferromagnetic at room temperature. It has been observed in the Table 5.17.

Table 5.17 The values of saturation magnetization of $Fe_{73.5-x}Cr_xNb_3Cu_1Si_{13.5}B_9$ [$x = 7, 9, 10 \text{ \& } 12.5$] alloys at different annealing temperature with constant annealing time 30 minutes and constant applied field 10kOe

Cr – Content x at %	M_s at room temperature in emu/g	M_s at $T_a=500^\circ C$ in emu/g	M_s at $T_a=550^\circ C$ in emu/g	M_s at $T_a=600^\circ C$ in emu/g
x = 7	71.52	86.25	96.62	99.86
x = 9	59.2	67.81	73.58	89.76
x = 10	55.41	63.02	68.91	85.43
x = 12.5	11.12	23.68	33.72	47.86

Present investigations those amorphous crystalline alloys $Fe_{73.5-x}Cr_xNb_3Cu_1Si_{13.5}B_9$ with $x = 7, 9, 10 \text{ \& } 12.5$, at room temperature show an increase of magnetization (M) at room temperature when annealed below the onset crystallization temperature. M_s at room temperature has been measured annealed samples. The annealing has been out for 30 minutes at $T_a = 500^\circ C$ to $600^\circ C$. Fig. 5.31 to Fig. 5.34 shows the field dependence of M for nanocrystalline amorphous ribbon and there by treated samples measured by VSM. From the curves it is clearly evidenced that the M is saturate for all samples in the annealed states within an applied filed 10kOe. Maximum M_s is reached at $600^\circ C$ for the all samples. It can be seen that clearly demonstrates an increase of magnetization upon T_a for all these four samples. Aranda *et. at.* [5.26] have studied the approach to saturation in nanocrystalline FINEMET materials. The magnetization prior to saturation is associated with reversible rotation and has been fitted to the law

$$M(H) = M_s \left[1 - \frac{a_1}{H} - \frac{a_2}{H^2} \right] + bH^{1/2} \quad (5.4)$$

where the term $\frac{a_2}{H^2}$ was described as being a direct consequence of the random anisotropy model, and attributable to Fe-Si grains. The co-efficient a_2 reflects the Herzer's predicted effective magnetic anisotropy of the nanocrystalline material,

whereas in amorphous alloys it is postulated as being caused by local stress and magneto elastic coupling M_s . It is to be noted that an increase in M_s due to structural relaxation has also been detected in Fe based metallic glass [5.27], with reference to the enhancement of magnetization of annealed samples. DTA thermograms have been taken on samples annealed at $T_a = 500^\circ\text{C}$, 550°C , 600°C along with the as-cast samples. M_s increases substantially only up to 600°C which is close to the onset of crystallization temperature (T_{x1}) for these alloy according to DTA data of Table 5.1. The amorphous nanocrystalline alloys $\text{Fe}_{61}\text{Cr}_{12.5}\text{Nb}_3\text{Cu}_1\text{Si}_{13.5}\text{B}_9$ has been paramagnetic at room temperature shown in Fig. 5.34. The area under the first crystallization event Fe(Si) phase slightly diminishes for $x = 10$ and 12.5 implying that initiation crystallization seems to take place and accordingly M Vs H curves sharply rises and look like ferromagnetic for $x = 12.5$ which is paramagnetic in the amorphous condition with $T_c = 246$ K. This increase of magnetization for the sample $x = 12.5$ is due to the evolution of ferromagnetic Fe(Si) crystallites.

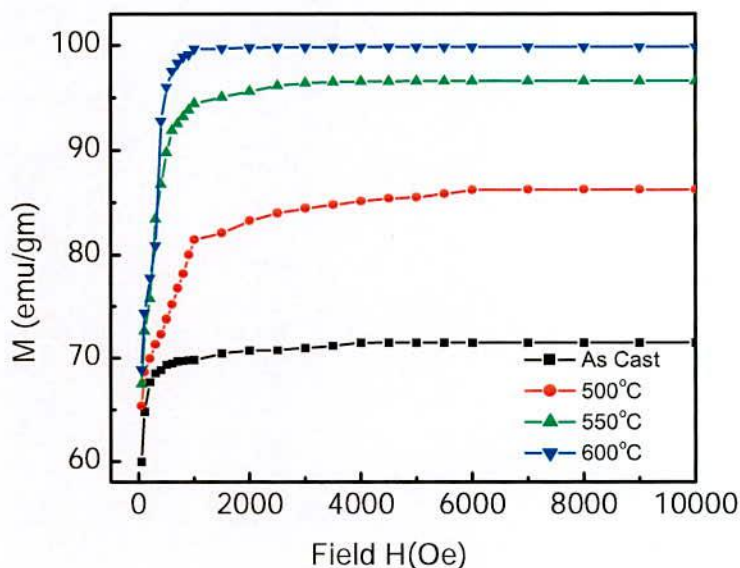


Fig. 5.31 Field dependence of specific magnetization curves of amorphous nanocrystalline ribbons with composition $\text{Fe}_{66.5}\text{Cr}_7\text{Nb}_3\text{Cu}_1\text{Si}_{13.5}\text{B}_9$ alloy in the as-cast and different annealed samples

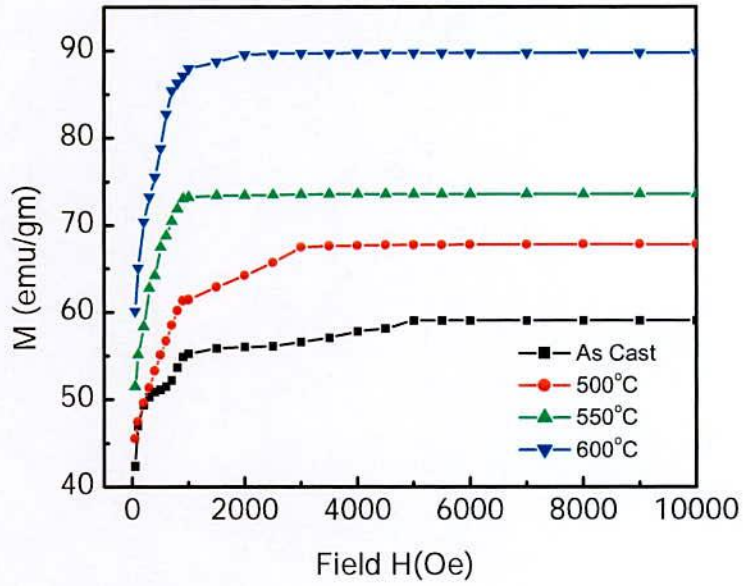


Fig. 5.32 Field dependence of specific magnetization curves of amorphous nanocrystalline ribbons with composition $\text{Fe}_{64.5}\text{Cr}_9\text{Nb}_3\text{Cu}_1\text{Si}_{13.5}\text{B}_9$ alloy in the as-cast and different annealed samples

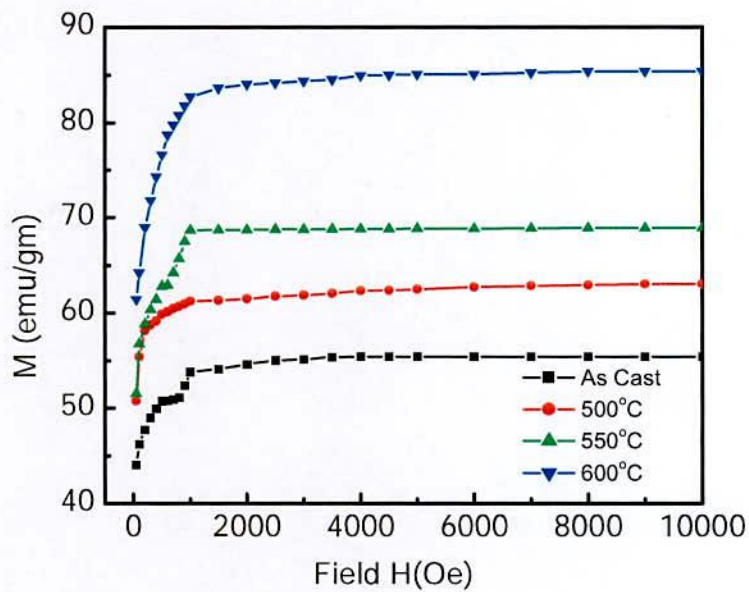


Fig. 5.33 Field dependence of specific magnetization curves of amorphous nanocrystalline ribbons with composition $\text{Fe}_{63.5}\text{Cr}_{10}\text{Nb}_3\text{Cu}_1\text{Si}_{13.5}\text{B}_9$ alloy in the as-cast and different annealed samples

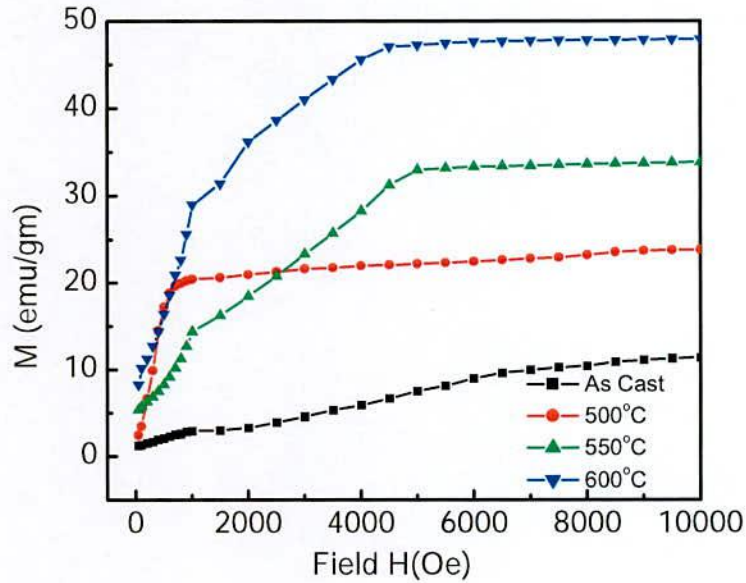


Fig. 5.34 Field dependence of specific magnetization curves of amorphous nanocrystalline ribbons with composition $\text{Fe}_{61}\text{Cr}_{12.5}\text{Nb}_3\text{Cu}_1\text{Si}_{13.5}\text{B}_9$ alloy in the as-cast and different annealed samples

An increase of M_s for the annealed samples at 500°C to 600°C compared with amorphous state is due to the irreversible structural relaxation, changing the degree of chemical disorder of the amorphous state [5.27] and enhanced volume fraction of $\text{Fe}(\text{Si})$ nanocrystals that are exchange coupled. The M_s are shown in Table 5.17. In Fig. 5.31 to Fig. 5.34 it has been evidence that from the temperature above T_c^{annl} , i.e. $T_a = 500^\circ\text{C}$, 550°C , 600°C , magnetization value of the studied samples ($x = 7, 9, 10$ & 12.5) is nearly zero since they are paramagnetic in this temperature range (shown in Fig. 5.28(a), Fig. 5.28(b), Fig. 5.28(c) and Fig. 5.29). At $T_a = 410^\circ\text{C}$ (shown in Table 5.16) above the crystallization behavior of the amorphous samples has been well demonstrated as the temperature continue to rise other. The sharp rise of magnetization of all the annealed amorphous nanocrystalline samples in their paramagnetic state is connected to the onset crystallization of $\alpha - \text{Fe}(\text{Si})$ ferromagnetic phase in the remaining amorphous matrix. The onset of primary crystallization temperature corresponds well with that of DTA thermograph measured with the same heating rate. The magnetization of this newly evolved ferromagnetic phase rises fast with increase of annealed temperature due to enhanced volume fraction of crystallized $\alpha - \text{Fe}(\text{Si})$ phase and passes through a maximum, beyond

which it decreases to a very low value. It is clearly observed from the XRD spectra at 600°C annealed samples [shown in Fig. 5.14, Fig. 5.17, Fig. 5.20 and Fig. 5.23] that the height of the peak related to the crystallization process of $\alpha - Fe(Si)$ phase decreases remarkably with increasing Cr-content indicating the stabilization effect of Cr against primary crystallization together with the reduction of magnetization of the nanograins [shown in Table 5.17]. Similar effect of substitution of Fe by Al in FINEMET has been observed by Zorkevskaja *et. al.*[5.28]. The decrease of M after passing through the maximum is M_s connected to the T_a of magnetization of $Fe(Si)$ crystallization phase which undergoes a FM-PM phase at $T_a = 600^\circ C$. It indicates that the crystallization $Fe(Si)$ phase is completely suppressed for higher Cr content alloy which has also confirmed the DTA thermogram.

CHAPTER VI

CONCLUSION

CONCLUSION

6.1 Conclusion

Nanocrystalline amorphous ribbon of FINEMET family with a nominal composition $Fe_{73.5-x}Cr_xNb_3Cu_1Si_{13.5}B_9$ [$x = 7, 9, 10$ & 12.5] has been studied to find out the correlation between microstructural features and magnetic properties dependent on various stages of nanocrystalline during the isothermal annealing around the crystallization temperature of their amorphous precursors. The crystallization behavior of the samples was investigated by DTA. The amorphous and annealed samples were examined by XRD. Magnetization measurement as a function of temperature and field were performed by VSM. From the systematic investigation on the crystallization, structural and magnetization of the present system to following conclusions can be outlined.

DTA experiments were performed for five different heating rates 10 to $50^\circ C/min.$ in steps of $10^\circ C/min.$ up to a temperature of $800^\circ C.$ From the DTA thermogram with continues heating, two well-defined exothermic peaks corresponding to $\alpha - Fe(Si)$ and FeB phase respectively. The knowledge of crystallization temperatures has been fruitfully utilized during the isothermal annealing of these amorphous ribbons for nanocrystallization which is ultimately controls the magnetic properties of FINEMET alloys. The primary crystallization temperature depends sensitively on Cr concentration which shifts to higher temperature as the Cr-concentration is increased. However, for higher Cr-content alloys, the two crystallization temperatures are almost merged with each other since the secondary crystallization temperature of higher Cr-content alloys are hardly affected by Cr-content. The crystallization of each phase occurred over a wide range of temperature and the primary crystallization shifts to higher temperature as the higher content Cr-concentration increased. But this difference decreases as the Cr-content is increased for $x = 12.5$. This samples that higher Cr-content alloys weaken the diffusion process to form crystallization phases. It is clearly understood that the partial substitution of Fe by Cr enhance thermal stability of amorphous alloys against crystallization.

The activation energy of first crystallization phase $\alpha - Fe(Si)$ and second crystalline phase FeB calculated using Kissinger's plot. The activation for the primary crystallization, E_1 decreases gradually increase with Cr-content but E_1 increase at Cr =

12.5 at. %. The activation energy of secondary crystallization product Fe_2B , E_2 are varies 3.28 to 3.76 eV. The knowledge of crystallization temperatures is important to determine to appropriate annealing temperature for nanocrystallization, which finally controls the magnetic properties of the FINEMET type of alloys. The temperature difference between two crystallization peaks ($T_{p2} - T_{p1}$) are found to exist around 151°C for $x = 7$, 147°C for $x = 9$, 153°C for $x = 10$ and 126°C for $x = 12.5$ at constant heating rate $50^\circ\text{C}/\text{min}$. This peak separation temperature is important for the stability of primary crystallization phase $\alpha - \text{Fe}(\text{Si})$ against detrimental boride phases while is necessary for fabrication of higher quality inductors.

The amorphous stage of the as-cast ribbons has been confirmed by XRD. The evaluation of primary phase on annealed samples has been confirmed as bcc- $\text{Fe}(\text{Si})$ and their sizes have been determined from the line broadening of fundamental peaks (110) from XRD pattern as affected by annealing around the crystallization temperature. The temperature corresponding to the onset of crystallization obtained from the XRD pattern is slightly lower than that of DTA data. The reason might be the two different methods of measurements. XRD measurement has been carried out on isothermal annealed samples while that of DTA on an isothermal. The grain size determined for the sample $x = 7$ from 11 to 28nm for the annealing temperature from 550°C to 800°C , $x = 9$ from 13 to 30nm for the annealing temperature from 600°C to 800°C , $x = 10$ from 12 to 29nm for the annealing temperature from 600°C to 800°C and $x = 12.5$ from 16 to 29nm for the annealing temperature from 650°C to 800°C . The higher Cr-content alloys ($x = 12.5$) do not show any sign of crystallization in their XRD pattern even at an annealing temperature of 600°C for 30 min. This is quite reasonable since their crystallization onset temperature is 650°C and higher. The lattice parameter and Si at. % shows an inverse relationship indicating that Si diffuses out of $\alpha - \text{Fe}(\text{Si})$ grains for which the size of $\alpha - \text{Fe}$ lattice is regained. Grain growth rapidly and attain values 19nm at 750°C for $x = 7$, 27nm at 700°C for $x = 9$, 25nm for $x = 10$ and 25nm for $x = 12.5$. For $x = 12.5$ indicating formation of boride phase (Fe_2B). The formation of boride phase is detrimental to soft magnetic properties.

The saturation magnetization values of all the studies samples at room temperature decreases as the Cr-contents increase. Magnetic saturation can be

achieved only for Fe-based alloys. It is evident from the results that the M_s decrease as the Cr-contents increase. It is observed in the present investigation that the nanocrystalline sample $Fe_{61}Cr_{12.5}Nb_3Cu_1Si_{13.5}B_9$ is paramagnetic at room temperature shows an increase of M at room temperature when annealed below the onset crystallization temperature. The Curie temperature of interfacial amorphous phase has been found to decrease as the Cr-content increasing implying the effect of Cr on the dilution of magnetic moment as well as the weakening of exchange interaction between Fe magnetic moment. Magnetization (M) of the amorphous state increases with the increases of annealing temperature corresponding to the early stage of crystallization due to irreversible structural relaxation. The room temperature M values for the high Cr-content nanocrystalline alloy ($x = 12.5$), which are paramagnetic at room temperature are found to increase substantially when annealed below the crystallization onset temperature. This understanding soft magnetic properties of studied samples have been achieved due to averaging out of the magnetic anisotropy energy by exchange interaction between the monometric Fe(Si) grains with appropriate volume fraction transmitted through their intergranular amorphous layer.

6.2 Scope for Future Work

There is much scope for future research in controlling the magnetic characteristics by changing composition and heat treatment certain important parameter like temperature dependence magnetization, anisotropy magnetostriction and Mössbauer effect can be study in detail for a better understanding of microstructure property relationship of Cr-based FINEMET type alloys.

REFERENCE

REFERENCE

Chapter I

- [1.1] H. Gleiter; "Nanocrystalline Materials", Progress in Materials Science, 33 223-315, 1989
- [1.2] Judit Kopniczky; "Nanostructures studied by atomic force microscopy"; Ph.D. Thesis, Uppsala University, Sweden, 2003
- [1.3] Y. Yoshizawa and K. Yamauchi; "Fe-based soft magnetic alloys composed of ultrafine grain structure"; Materials Transaction. JIM. Vol. 31, No. 4 307-314, 1990
- [1.4] G. Herzer; J. Magn. Magn. Mat., 157/158, 133-136, 1996
- [1.5] G. Herzer; "Grain structure and Magnetism of Nano crystalline Ferromagnetic"; IEEE Terns. Magn., 26, pp 1397 – 1402, 1990
- [1.6] T. Kulik, A. Hernando; "Magnetic properties of two-phase nanocrystalline alloy determined by anisotropy and exchange interactions through amorphous matrix"; J. Magn. Magn. Mat.;138, 270-280, 1994
- [1.7] L. K. Varga, E. Bakos, E. Kisdi-Koszo, E. Zsoldos, L. F. Kiss; "Time and temperature dependence of nanocrystalline structure formation in a finemet-type amorphous alloy"; J. Magn. Magn. Mat.; 133, 280-282, 1994
- [1.8] M. Muller, N. Mattern, U. Kuhn; "Corelation between magnetic and structural properties of nanocrystalline soft magnetic alloys"; J. Magn. Magn. Mat.; 157/158, pp. 209-210, 1996
- [1.9] Y. Yoshizawa, S. Oguma, K. Yamauchi; "New Fe-based soft magnetic alloys composed of ultra-fine grain structure"; J. Appl. Phys. 6044-6046, Vol. 64, 1988
- [1.10] G. Herzer; "Nanocrystalline Soft Magnetic Alloys"; Chapter 3 in Hand Book of Materials, Vol. 10 ed., K. H. J. Buchow, Elsevier Pub. Co. p.417, 1997
- [1.11] M. A. Hakim; "Magnetic softening of nanocrystalline Fe-Cu-Nb-Si-B alloys on annealing"; J. Bangladesh Electronic Society; Vol. 4 pp. 40-45, 2004
- [1.12] S. N. Kane, S. Sarabhai, Ajoy Gupta, L. K. Varga, T. Kulik; "Effect of quenching rate on crystallization in $Fe_{73.5}Nb_3Cu_1Si_{13.5}B_9$ alloy"; J. Magn. Magn. Mat.; Vol. 215-216, pp. 372-374, 2000

- [1.13] I. Z. Rahman, Md. Kamruzzaman, M. A. Rahman; "Crystallization behavior in Fe-based metallic glass ribbons"; the 2nd international conference on structure, processing and properties of materials; SPPM; 25-27 February-2004, Dhaka, Bangladesh; pp. 607-614
- [1.14] R. Alben, J. J. Becker, M. C. Chi; "Random anisotropy in amorphous ferromagnets"; J. Appl. Phys. Vol. 49, pp. 1653, 1978
- [1.15] O. Ohnuma, D. H. Pins, T. Abe, H. Onodera, K. Hono and Y. Yoshizawa; "Optimization of the microstructure and properties of Co-substituted Fe-Si-B-Nb-Cu nanocrystalline soft magnetic alloys"; J. Appl. Phys.; Vol. 93, No.11, pp. 1986 – 9194, 1 June 2003
- [1.16] A. Fernandez, M. J. Perez, M. Tejedor, V. Madurga; "Thermo magnetic analysis of amorphous $(\text{Co}_x\text{Fe}_{1-x})_{73.5}\text{Nb}_3\text{Cu}_1\text{Si}_{13.5}\text{B}_9$ metallic glasses"; J. Magn. Magn. Mat.; 221; 338-344, 2000
- [1.17] A. Zorkovska, J. Kovac, P. Sovak, P. Petrovic, M. Konc; "Structure and Magnetic behavior of Fe-Cu-Nb-Si-B-Al alloys" ; J. Magn. Magn. Mat.; 215-216; 472-494, 2000
- [1.18] S. H. Lim, W. K. Pi, T. H. Noh, H. J. Kim and I. K. Karg; "Effects of Al on the magnetic properties of nanocrystalline $\text{Fe}_{73.5}\text{Nb}_3\text{Cu}_1\text{Si}_{13.5}\text{B}_9$ alloys" J. Appl. Phys.; Vol. 73, No. 10, 15 May 1993
- [1.19] L. Del. Riego, M. El Ghannami, M. Dominguez, C. F. Conde, A. Conde; "Super paramagnetic behavior of a nanocrystalline Fe(Cr-Mo)Si B Cu Nb alloy"; J. Magn. Magn. Mat.; 197, 201-203, 1999
- [1.20] V. Franco, C. F. Conde, A. Conde; "Magnetic properties and crystallization of a $\text{Fe}_{63.5}\text{Cr}_{10}\text{Nb}_3\text{Cu}_1\text{Si}_{13.5}\text{B}_9$ alloy"; J. Magn. Magn. Mat.; 203; 60-62, 1999
- [1.21] T. H. Noh, M. B. Lee, H. J. Kim, I. K. Kang; "Relationship between crystallization process and magnetic properties of Fe-(Cu-Nb)-Si-B amorphous alloys"; J. Appl. Phys. 67, 5568, 1990
- [1.22] Y. Yoshizawa and K. Yamachi; Magnetic properties of Fe-Cu-M-Si-B (M = Cr, V, Mo, Nb, Ta, W) alloy"; Mater. Sci. Eng. A (b) 133, 176, 1991
- [1.23] M. Muller, and N. Matern, "The influence of refractory element additions on the magnetic properties and on the crystallization behavior of nanocrystalline soft magnetic Fe-B-Si-Cu alloys"; J. Magn. Magn. Mater. 136,79, 1994
- [1.24] P. K. Roy; M. Phil Thesis, Department of Physics, KUET, Khulna, May - 2007

- [1.25] G. Herzer; In: Buschow KHJ Editor, "Hand book of magnetic materials"; Amsterdam: Elsevier Science, 10, 415, 1997
- [1.26] N. Murillo, J. Gonzalez, J. M. Blanco, J. M. Gonzalez; *J. Appl. Phys.*, 79, 5465, 1996
- [1.27] Le Minh, Bach Thanh Cong, Tran Quoc and Nguyen Chau; Proceeding of the 2nd International Workshop on Materials Science (IWOMS'95) Hanoi, Oct. 1995
- [1.28] E. Estevez Rams, J. Fidler, M. Dahlgren, R. Grossinger, M. Knobel, P. Tiberto, P. Alia and F. Vinal; *J. Phys. D; Appl. Phys.* 29 848-854, 1996
- [1.29] Saroat Noor, M. Phil Thesis, Department of Physics, KUET, Khulna, March-2005
- [1.30] Saroat Noor, S. S. Sikder, D. k. Saha and M. A. Hakim; "Time and Temperature Dependence of Nanocrystallization and initial Permeability of FINEMET alloy"; *Nuclear Science and Applications*, Vol. 15, No.1, 9-13, 2006
- [1.31] T. H. Noh, M. B. Lee, H. J. Kim, I. K. Kang "Relationship between crystallization process and magnetic properties of Fe-(Cu-Nb)-Si-B amorphous alloys", *J. Appl. Phys* 67, 5568, 1990
- [1.32] N. Kataoka, T. Matsunaga, A. Inoue, T. Masumoto; "Soft magnetic properties of b.c.c Fe-Au-X-Si-B (X=early transition metal) alloys with fine grain structure"; *Mater. Trans. JIM.* 30, 947-950, 1989
- [1.33] M. Müller and N. Matern; "The influence of refractory element additions on the magnetic properties and on the crystallization behavior of nanocrystalline soft magnetic Fe-B-Si-Cu alloys"; *J. Magn. Mater.* 136, 79, 1994
- [1.34] P. K. Roy; M. Phil Thesis, Department of Physics, KUET, Khulna, May - 2007
- [1.35] A. Inoue, K. Kobayashi, J. Kanerhira and T. Masumoto; "Mechanical properties and thermal stability of (Fe-Co-Ni)-M-B (M = IV, V and VI group transition metals) amorphous alloys with low Boron concentration"; *Sci. Rep. Res. Inst. Tohoku Univ.* vol. A 29, p.331-342, 1981
- [1.36] K. Suzuki, A. Makino, N. Kataoka, A. Inoue, and T. Masumoto; "Soft magnetic properties of nanocrystalline b.c.c. Fe-Zr-B and Fe-M-B-Cu (M= transition metals) alloys with high saturation magnetization"; *J. Appl. Phys.*, 70(10), 6232, 1991

- [1.37] K. Suzuki, A. Makino, A. Inoue, and T. Masumoto; "Low core losses of nanocrystalline Fe-M-B (M = Zr, Hf or Nb) alloys"; J. Appl. Phys., 74, 3316, 1993
- [1.38] G. Herzer; "Grain Size dependence of Coercivity and Permeability in nanocrystalline ferromagnets" IEEE Trans. Mag. 26(5), 1397-1402, 1990
- [1.39] A. Hakim, S. Manjura Haque; "Effect of structural parameters on soft magnetic properties of two phase nanocrystalline alloy of $Fe_{73.5}Ta_3Cu_1Si_{13.5}B_9$ " J. Magn. Magn. Mater, 284, 395-402, 2004
- [1.40] S. Manjura Haque, A. Hakim; "Ultra-soft magnetic properties of devitrified $Fe_{75.5}Cu_{0.6}Nb_{2.4}Si_{13}B_{8.5}$ " J. Materials Chemistry and Physics, 101 112-117, 2007
- [1.41] V. Franco, C. F. Conde, A. Conde, L. F. Kiss; "Super paramagnetic behavior in a $Fe_{76}Nb_3Cu_1Si_{10.5}B_{9.5}$ alloy" J. Magn. Mater. 215-216, 400-403, 2000
- [1.42] A. Slawska –Wanicwska, M. Gutowski, H. Lachowicz, T. Kulix, M. Matiya; Phys. Rev. B 46, 14 594, 1992
- [1.43] H. K. Lachowicz, A. Slawska –Wanicwska; J. Magn. Magn. Mat., 133, 238, 1994
- [1.44] Md. Sultan Mahmud, S. S. Sikder and M. A. Hakim; "Crystallization behavior and Initial Permeability of Fe (Cr) Cu Nb Si B Nanocrystalline alloys"; Journal of Science & Arts, Issue 1, Vol. 1, 33-41, 2004
- [1.45] N. Chau, P. Q. Thanh, N. Q. Hoa and N. D. The, "The existence of giant magnetocaloric effect and laminar structure in $Fe_{73.5-x}Cr_xNb_3Cu_1Si_{13.5}B_9$ "; J. Magn. Mater. 304 36-40, 2006
- [1.46] N. Chau, P. T. Hue, N. Q. Hoa, H. D. Anh, N. H. Luong, M. A. Asgar, S. S. Sikder, Md. Sultan Mahmud; "An existence of Laminar Structure in nanocrystalline ribbon in finemet with partial substitution of Fe by Cr". Proceedings of the seventh Vietnamese – German Seminar on Physics and Engineering, Halong City, March 28 to April 5, 2004
- [1.47] D. K. Saha and M. A. Hakim; "Crystallization behavior of $Fe_{73.5}Au_1Nb_3Si_{13.5}B_9$ Amorphous Nanocrystalline soft magnetic alloy"; Bangladesh Academy of Science, Vol. 30 No. 2, p. 177-187, 2006
- [1.48] M. A. Hakim, S. S. Sikder, Md. Sultan Mahmud and S. Manjura Hoque; "Dilution of magnetic moment of Fe by Cr for $Fe_{73.5-x}Cr_xNb_3Cu_1Si_{13.5}B_9$ and field cooled and zero field cooled behavior for higher Cr-content"; Journal of Korean Physical Society (JKPS), Vol. 52, No. 5, 2008

- [1.49] Md. Sultan Mahmud; PhD thesis, Department of Physics, KUET, Khulna, April, 2008
- [1.50] A. Lovas, L. F. Kiss, I. Balong; "Saturation magnetization and amorphous Curie point changes during the early stage of amorphous nanocrystalline transformation of a FINEMET – type alloy"; *J. Magn. Mater.* **215-216**, 463, 2000
- [1.51] A. E. Berkowitz, J. L. Walter, K. F. Wall; "Magnetic properties of amorphous particles produced by Spark Erosion"; *Phys. Rev. Lett.* **46**, 1484, 1981

Chapter II

- [2.1] P. Duwez; *J. Am Inst. Metal Eng.* 191: 765, 1951
- [2.2] P. Duwez, R. H. Willens and W. Klement; *J. Appl. Phys.* 31, 1136, 1960
- [2.3] P. Duwez; *Trans. Am SOC Met.* 60: 607, 1967
- [2.4] P. Duwez; *Ann Rev. Mat. Sci.* 6: 83, 1967
- [2.5] S. Mader; *Nowick As.; Appl. Phys. Lett.* 7: 57, 1965
- [2.6] C. C. Tsuei, P. Duwez; *J. Appl. Phys.* 37: 435, 1960
- [2.7] M. A. Mc Henry, M. A. Willard and D. E. Laughlin; "Amorphous and nanocrystalline materials for applications as soft magnets"; *Prog. Mat. Sci.* 44 291- 433, 1999
- [2.8] T. Mizoguchi; IBM Research report, RC 6045, 1976
- [2.9] R. Alben, J. I. Budnic and G. S. Gargil; *a₁₁₁ Metalliclasses*, "American SOC. for metals"; pp304, 1978
- [2.10] Y. Yoshizawa, S. Ogma and K. Yamachi; "New Fe-Based Soft Magnetic Alloys Composed of Ultra-fine Grains Structure"; *J. Appl. Phys.* 64, 6044, 1988
- [2.11] Y. Yoshizawa and K. Yamachi; "Magnetic Properties of Fe-Cu-M-Si-B (M = Cr, V, Mo, Nb, Ta, W) alloy"; *Mater. Sci. Eng. A (b)*. 133, 176, 1991
- [2.12] Y. Yoshizawa and K. Yamachi; "Fe-based soft magnetic alloys composed of ultra-fine grains structure"; *Mater. Trans. JIM. (a)* 31, 307, 1990
- [2.13] G. Herzer, H. Warlimont; *Nanostructured materials*, 1, 263-268, 1992
- [2.14] K. Hono and T. Sakurai; "Atom Probe studies of nanostructured alloys"; *Appl. Surf. Sci.* 87/88, 166, 1995

- [2.15] K. Hono, K. Higara, Q. Wang, A. Inoue and T. Sakurai; "The microstructure evolution of a $Fe_{73.5}Nb_3Cu_1Si_{13.5}B_9$ nanocrystalline Soft Magnetic material"; *Acta. Metall. Mater.* 40(9) 2137-2147, 1992
- [2.16] G. Herzer; "Nanocrystalline Soft Magnetic Alloys"; *Hand Book of Materials*, K. H. J. Buchow (ed), 10, 415-462, 1997
- [2.17] U. Koster, M. Schonmann, Blank-Bewersdorff S. Brauer, M. Sutton and G. B. Stephemon; *Mat. Sci. Eng.* **A133** 611, 1991
- [2.18] G. Herzer; In: *Proc of Int. Symp. On 3ab Transition-Semi Metal Thin Films. Magnetism and Processing* (Japan SOC for the promotion of Science, Committee, Sendia, Japan) **131** 130, 1991
- [2.19] H. Warlimont; *Mater. Sci. Eng.* 99, 1988
- [2.20] A. Makino, A. Inoue, T. Masumoto; *Mat. Trans. JIM* **36**, 924, 1995
- [2.21] D. Turnbull; *Contemp. Phys.* 10, 473, 1969
- [2.22] P. Duwez, R. H. Willens and W. Kelton Jr.; *J Appl. Phys.* 31, 1136, 1960
- [2.23] J.M.D. Coey and H. Sun; *J. Magn. Mater.* **87** 1251, 1991
- [2.24] K. Schnitzke, L. Schultz, J. Wecker and M. Katter; *Appl. Phys. Lett.*, **57** 2853, 1990

Chapter III

- [3.1] D. Turnbull; "Under what conditions can a glass be formed?"; *Contemp. Phys.* 10, 473-488, 1969
- [3.2] W. L. Johnson; "Thermodynamic and Kinetic aspects of the crystal to glass transformation in metallic materials; *Progress in materials Science*, **30**, PP. 81-134, 1986
- [3.3] D. Louca, K. Ahn, V. Ponnambalam and S. J. Poon; "local order in amorphous Fe-alloys"; *Mat. Res. SOC. Proc. Vol. 754*, PP. CC 7.7.1-CC7.7.6. 2003
- [3.4] J. W. Martin, R. D. Doherty, B. Canter; "Stability of microstructure in metallic systems"; Cambridge, UK, 1997
- [3.5] W. Kauzmann; *Chem. Rev.*; **43** PP. 219-256, 1948
- [3.6] *The IUPAC Compendium of Chemical Terminology*, **66** 583, 1997
- [3.7] H. Jones, *Rep. Prog. Phys.*, **36** 1425, 1973

- [3.8] D. Turnbull, *J. de physique*, **35** C4-1, 1974
- [3.9] S. Takayama; "Amorphous structure and their formation and stability"; *J. Materials Sci.* Vol. 11(1) 164-185, 1976
- [3.10] J. T. S. Irvine, E. Amano, A. Huanosta, R. Valenzuela, A. R. West; "Solid State should peak at T_c "; *Ionic* 40/41, 220, 1990
- [3.11] M. H. Cohen and D. Turnbull; "Composition Requirements for Glass Formation in Metallic and Ionic Systems"; *Nature* 189 131-132, 1961
- [3.12] G. Gargil, III; *J. Appl. Phys.*, 41, 2248, 1970
- [3.13] H. S. Chen; *Acta. Mat.* 22, 1505, 1974
- [3.14] S. R. Nageland, J. Taue; "Nearly- free- electron Approach to the theory of Metallic Glass Alloys"; *Phys. Rev. Lett.*, 35, 380, 1975
- [3.15] A. E. Berkowitz, J. L. Walter, K. F. Wall; "Magnetic Properties of amorphous particles produced by Spark Erosion"; *Phys. Rev. Lett.* 46, 1484, 1981
- [3.16] P. Murray and J. White; "Kinetics of the thermal dehydration of clays"; *Trans. Brit. Ceram. SOC.* 48, 187-206, 1949
- [3.17] P. Murray and J. White; "Kinetics of the thermal decomposition of clay 2, Isothermal decomposition of clay materials"; *Trans. Brit. Ceram. SOC.* 54, 151-187, 1955
- [3.18] P. Murray and J. White; "Kinetics of the thermal decomposition of clay 4, Interpretation of the differential thermal analysis of clays", *Trans. Brit. Ceram. Soc.* 54, 204-237, 1955
- [3.19] E. C. Sewel; "The consequences for differential thermal analysis of assuming a reaction to be first order"; *Clay Minerals Bul.* 2, 233-241, 1955
- [3.20] H. E. Kissinger; "Reaction Kinetics in Differential Thermal Analysis"; *Anal. Chem.* 29(11) 1702-1706, 1957
- [3.21] F. G. Boswell ; "On the calculation of activation energies using a modified Kissinger method"; *J. Therm. Anal.* 18(2) 353-358, 1980
- [3.22] B. D. Cullity; "Elements of X-Ray diffraction"; Reading, M.A. Addisonwesley, 1978

- [3.23] G. Herzer; "Grain size dependence of coercivity and permeability of Nanocrystalline ferromagnets"; IEEE Trans. Magn., **MAG-26** 1397, 1990
- [3.24] R. Alben, J. J. Becker, M. C. Chi.; "Random Anisotropy in Amorphous Ferromagnets"; J. Appl. Phy. **49** 1653-1658, 1978
- [3.25] G. Bertotti, E. Ferrara, F. Fiorillo, P. Tiberto; Mat. Sci. Eng. **A**, **226-228** 603, 1997
- [3.26] JMD Coey; "Rare-earth iron Permanent magnets"; Oxford; Oxford Science Publications, Clearendon Press, 1996
- [3.27] G. Herzer; "Nanocrystalline Soft Magnetic Materials"; J. Magn. Magn. Mater. **157/158** 133, 1996
- [3.28] A. Hernando, M. Vazquez, T. Kulik and C. Prados; "Analysis of the dependence of Spin-Spin correlations on the thermal treatment of the Nanocrystalline materials"; Phys. Rev. B **51** 3581, 1995
- [3.29] R. Grossinger, D. Holzer, C. Ksshach, H. Sassik, R. StaoTurtelli; J. P. Sinnecker, E. Witting ; J. Magn. Magn. Mater. in press
- [3.30] A. Hernando, T. Kulik; "Exchange interaction through amorphous paramagnetic layers in ferromagnetic nanocrystals"; Phys. Rev. B **49** 7064, 1994
- [3.31] J. S. Kouvel; "Magnetism and Metallurgy"; eds. A. Berkowitz and E. Kneller Academic press, New York, **Vol. 2A**, P 523,1969
- [3.32] M. E. Mc Henry, M. A. Willard and D. E. Laughlin; "Amorphous and nanocrystalline materials for application as soft magnets"; Prog. Mat. Sci. **44**, 291-433, 1999
- [3.33] K. Yamaguchi and T. Mizaguchi; J. Phys. SOC. Japan, **39**, 541, 1075
- [3.34] R. Bozorth; "Ferromagnetism", D. Van Nostrand, Princeton N. J. **76**, 1951
- [3.35] K. Handrich; "Conditions for the Existence of Amorphous Ferromagnets" Phys. Stat. Sol. (b) **53**, K17, 1972

Chapter IV

- [4.1] H. Le Chatelier; Bull SOC. France Mineral, **10**, 204, 1987
- [4.2] W. B. Pearson; "A Hand book of Lattice spacing and Structures of Metals and Alloys" (Oxford Pergamon), 1958

- [4.3] M. A. Mazid and M. A. Chowdhury; "Design and Construction of Forner type Vibrating Sample Magnetometer"; AECD/MMD/1 (Bangladesh). June, 1986
- [4.4] Simon Foner; "Versatile and Sensitive Vibrating Sample Magnetometer"; Rev. Sci. Instr. 30, 160, 1959
- [4.5] D. K. Stevens and J. H. Crawford, Jr., Phys. Rev. 92, 1065, 1953

Chapter VI

- [5.1] M. E. Mc Henry, M. A. Willard and D. E. Laughlin; "Amorphous and nanocrystalline materials for applications as soft magnets." Prog. Mat. Sci. 44, 29-433, 1999
- [5.2] S. Manjura Hoque, M. A. Hakim, N. Chau; "Ultra soft magnetic properties devitrified $\text{Fe}_{75.5}\text{Nb}_{2.4}\text{Cu}_{0.6}\text{Si}_{13}\text{B}_{8.5}$ alloy" Mat. Chem. Phys. 101, 112-117, 2007
- [5.3] D. K. Saha and M. A. Hakim; Journal of Bangladesh Academy of Sciences; Vol. 30, No. 2, 177-187, 2006
- [5.4] W. G. Clements and B. Cantor; in Rapidly quenched metal, Section-1, (eds. N. J. Graut and B. C. Giessen) (MIT Press Cambridge, Mass) P-267, 1976
- [5.5] F. E. Luborsky; Materials Sci. Engg. - 28, P-139, 1977
- [5.6] F. E. Marzo, A. R. Pierna and A. A. Altube; "Analysis of nanocrystallization of FINEMET type alloy by temperature modulated differential scanning calorimetry"; Journal of Non-crystalline solids, 287, 349-354, 2001
- [5.7] C. L. Chen and R. S. Hasegawa; "Mössbauer study of glassy alloy $(\text{Fe-Mo})_{80}\text{B}_{20}$ "; J. Appl. Phys. 49(3) 1721, 1978
- [5.8] S. Noor., "Effects of two-step annealing on complex permeability of Fe-Nb-Cu-Si-B nanocrystalline soft magnetic materials" M. Phil Thesis, , KUET, P 70-72, March 2005
- [5.9] N. Chau, N. X. Chein, N. Q. Hoa, P. Q. Niew, N. H. Luong, N. D. Tho, V. V. Hiep; JMM 282, 174-179, 2004

- [5.10] T. Liu, N. Chen., Z. X. Xu, R. Z. Ma; "The amorphous to nanocrystalline transformation in $\text{Fe}_{73.5}\text{Cu}_1\text{Nb}_3\text{Si}_{13.5}\text{B}_9$ studied by thermogravimetry analysis"; J. Magn. Magn. Mater. 152, 359-364, 1996
- [5.11] E. F. Kneller and F. E. Luborsky; "Partical size dependence of coercivity and remanence of single domain partical"; J. Appl. Phys. 34, 656, 1963
- [5.12] Y. Yoshizawa, S. Oguma, K. Yamachi; "New Fe-based soft magnetic amorphous alloys composed of ultrafine grain structure"; J. Appl. Phys. 64(10), 6044-6046, 1988
- [5.13] B. D. Cullity; "Elements of X-ray Diffraction"; Adison-Wisley Publishing Company Inc., London, England, P. 262, 1959
- [5.14] Bozorth; "Ferromagnetism"; D. Van Norstrand Company, Inc., Princeton, NJ, P. 64, 1964
- [5.15] W. B. Pearson; "A Hand book of Lattice spacing and Structures of Metals and Alloys" (Oxford Pergamon), 1958
- [5.16] M. A. Hakim and S. Manjura Hoque; "Effect of Structural parameters on Soft Magnetic properties of two phase nanocrystalline alloy of $\text{Fe}_{73.5}\text{Cu}_1\text{Ta}_3\text{Si}_{13.5}\text{B}_9$ "; J. Magn. Magn. Mater, 284, P. 395-402, 2004
- [5.17] M. A. Mazid and M. A. Chowdhury; "Design and Construction of Forner type Vibrating Sample Magnetometer"; AECD/MMD/1(Bangladesh), June, 1986
- [5.18] A. Lovas, L. F. Kiss, L. Balong; J. Magn. Magn. Mat., 215-216, 463-465, 2000
- [5.19] D. Holzer, I. Perez de Albeniz, R. Grossinger, H. Sassik; J. Magn. Magn. Mater., 203, 82-84, 1999
- [5.20] M. A. Hakim; Nuclear Science and Application, 13, 36-43, 2004
- [5.21] K. Knobel, J. P. Sinnecker, R. Sato Turteli, N. R. Rechenberg, R. Grossinger; J. Appl. Phys., 73, 6603-6605, 1993
- [5.22] A. E. Berkowitz, J. L. Walter, K. F. Wall; Phys. Rev. Lett. 46, 1484-1487, 1981

- [5.23] A. Inoue, T. Masumoto; *Mater. Sci. Eng.* 173A:1, 1993
- [5.24] C. Appino and F. Florillo; *J. Magn. Magn. Mater.*; 133, 107, 1994
- [5.25] H. Knonmuller, N. Moser and T. Reininger; *Anales de Fisica B* 86(1), 1990
- [5.26] G. R. Aranda, J. Gonzalez, K. Kulakowski; *J. Appl. Phys.*; 83: 6341, 1998
- [5.27] A. E. Berkowitz, J. L. Walter and K. F. Wall; "Magnetic properties by spark
Forsion"; *Phys. Rev. Lett.* 46, 1484, 1981
- [5.28] A. Zorkovaska, J. Kovac, P. Sovak, P. Petrovic, M. Konc; *J. Magn. Magn.
Mater.*, 215-216, 492-494, 2000